REVIEW

Check for updates

Atomically dispersed metal catalysts for the oxygen reduction reaction: synthesis, characterization, reaction mechanisms and electrochemical energy applications

Minmin Liu,[*a] Linlin Wang,[a] Kangning Zhao, [a] Shanshan Shi,[a] Qinsi Shao,[a] Lei Zhang,[ab] Xueliang Sun, [ac] Yufeng Zhao[*a] and Jiujun Zhang [*a]

In recent years, atomically dispersed metal catalysts (ADMCs) with well-defined structures have attracted great interest from researchers for electrocatalytic applications due to their maximum atom utilization efficiency (100%), distinct active sites and high catalytic activity, stability and selectivity. Based on this, this review will comprehensively discuss the recent developments in advanced single-atom and dual-atom ADMCs for the oxygen reduction reaction (ORR), including synthesis and characterization, reaction mechanisms and energy applications such as in fuel cells and metal–air batteries. In addition, challenges will be summarized and analyzed, including the rational design and fabrication of ADMCs and a deeper understanding of their geometric configuration, electronic structure and reaction dynamics towards the ORR. Furthermore, to facilitate further development, future research directions are proposed to overcome associated challenges, such as (1) the exploration of new/advanced materials including metal precursors and supporting substrates for the fabrication of ADMCs; (2) the optimization of rational design and synthesis techniques for single- and dual-atom catalysts to significantly enhance catalytic ORR activity and stability based on modern characterization techniques; (3) a deeper understanding of ADMC structures, reactive active sites, interactions between metal atoms and support surfaces and corresponding electrocatalytic ORR mechanisms at the atomic level using a combination of density functional theory (DFT) calculations and advanced experimental techniques; (4) the optimization of ADMC-based catalyst layers and membrane electrode assemblies to achieve high performance fuel cells and metal–air batteries using advanced electrochemical testing strategies.

Broader context

In this review, the most recent developments in advanced atomically dispersed metal catalysts (ADMCs) with single-metal and dual-metal active sites on support materials in the application field of the oxygen reduction reaction (ORR) are comprehensively discussed, including their synthesis/characterization, reaction mechanisms and application in electrochemical energy conversion and storage devices such as fuel cells and metal–air batteries. To facilitate the future development of high-performance ADMCs, several technical challenges are summarized and analyzed and possible research directions are proposed to overcome these challenges. The challenges mainly include the rational and scale-up design and fabrication of ADMCs and a deeper understanding of their geometric configuration, electronic structure and reaction dynamics towards the ORR. In addition, mechanisms of the ORR catalyzed by ADMCs and structure–activity relationships can be further investigated by combining advanced physicochemical characterization techniques and theoretical calculations. And applications of ADMCs as the catalyst layer of fuel cells and metal–air batteries as well as corresponding electrochemical performances are thoroughly reviewed and discussed. This review also focuses on further design and optimization of ADMC catalyst layers and membrane electrode assemblies for fuel cells and metal–air batteries.

[a] *Institute for Sustainable Energy/College of Sciences, Shanghai University, Shanghai, 200444, China. E-mail: liumm@shu.edu.cn, yufengzhao@shu.edu.cn, jiujun.zhang@shu.edu.cn*

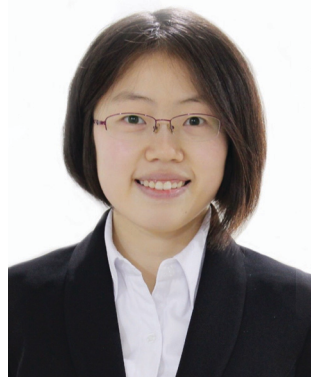[b] *Energy, Mining & Environment, National Research Council of Canada, Vancouver, V6T 1W5, Canada*

[c] *School of Materials and Mechanic Engineering, University of Western Ontario, London, Canada*

1. Introduction

Global concerns over the increase in fossil fuel usage and associated pollution have made the search for sustainable and renewable environmentally-friendly energy sources such as solar, wind, and so on one of the top priorities in the coming decades.[1,2] However, converted electricity from these weather-dependent

2890 | *Energy Environ. Sci.,* 2019, **12**, 2890–2923

This journal is © The Royal Society of Chemistry 2019

and unstable energy sources must be stored for smooth output to grid usage. Therefore, nanotechnology has become an important bridge to solve these problems. For example, electrochemical technologies[3–5] such as various batteries,[6,7] fuel cells,[8] supercapacitors[9] and H_2O and CO_2 electrolysis systems[10–14] have been recognized as the most practical options to meet this demand for energy storage and conversion. And among the various electrochemical technologies, fuel cells and metal–air batteries are two important types of devices that require air (oxygen) as the oxidant in one (positive electrode) of their two necessary electrode reactions. This reaction is called the Oxygen Reduction Reaction (ORR).[15] For example, low-temperature hydrogen–air (oxygen) fuel cells using proton exchange membranes (PEM) as the electrolyte are highly efficient and environmentally-friendly (zero emission) energy conversion devices that can be particularly applied in electric vehicles, as shown in Scheme 1(a). And because of their theoretically high energy/power densities and energy efficiencies, fuel cell technologies are potentially an eternal substitute for internal combustion engines in the fields of transportation and decentralized power.[16,17] And unlike batteries such as lithium-ion batteries, lead–acid batteries, nickel–metal hydride batteries, metal–air batteries, redox flow batteries and alkaline dry batteries, *etc.*, fuel cells are not energy storage devices, but rather, are power generation devices that can directly convert chemical energy (such as H_2) into electrical energy[18,19] with an external chemical fuel source. Furthermore, reactant fuel (H_2) and oxidants (O_2) can be continuously supplied into fuel cells to anodic and cathodic electrodes respectively to produce clean products (H_2O) and continuously output electrical energy and heat energy.[20] Regarding metal–air batteries (Scheme 1b) such as lithium–air and zinc–air, they are considered to be next generation batteries due to their extremely high energy densities.[21–24] In particular, rechargeable metal–air batteries possess great potential due to long-term stabilities and environmental benignity[25,26] and can possibly be used as alternatives to current energy density-limited lithium-ion batteries.

Minmin Liu

Dr Minmin Liu received her PhD in Analytic Chemistry from Changchun Institute of Applied Chemistry (CIAC), Chinese Academy of Sciences (CAS), under the direction of Professor Wei Chen in 2016. She was selected for the Shanghai Sailing Program in 2018. She is a lecturer at the Institute for Sustainable Energy/College of Sciences, Shanghai University. Her research interests focus on the design and application of carbon based nanomaterial electrocatalysts for electrochemical energy storage and conversion devices, such as fuel cells and metal–air batteries.

Linlin Wang

Dr Linlin Wang received her PhD in Inorganic Chemistry from the University of Science and Technology of China (USTC) under the direction of Prof. Kai-bin Tang and Prof. Yi-tai Qian in 2013. She was selected for the Shanghai Sailing Program in 2014. She is currently a full associate professor at Shanghai University. Her current research is focused on advanced materials for electrochemical energy storage and conversion, including electrodes in Li/Na/K-based batteries, Li/Na/K ion batteries, and electrocatalysis in fuel cells.
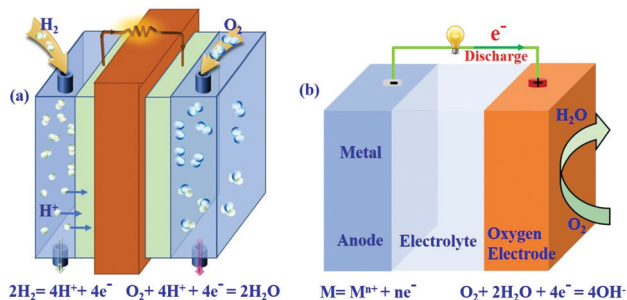
Kangning Zhao

Dr Kangning Zhao received his PhD in Materials Science and Engineering from Wuhan University of Technology under the direction of Prof. Liang Zhou and Prof. Liqiang Mai in 2019. He is currently a research associate at the Institute for Sustainable Energy/College of Sciences, Shanghai University. His current research interest is focused on the defect engineering and electrode/electrolyte interface modulation of electrocatalysis for fuel cells.

Lei Zhang

Lei Zhang is a Senior Research Officer at the National Research Council Canada (NRC) and a Fellow of the Royal Society of Chemistry (FRSC). Lei received her first Master's degree in Materials Chemistry (1993) from Wuhan University (China) and her second Master's degree in Physical Chemistry (2000) from Simon Fraser University (Canada). Lei's main research interests include advanced materials and electrochemical energy technologies in the areas of PEM fuel cell electrocatalysis, supercapacitors, metal–air batteries and Li-ion batteries. She has co-authored more than 200 publications (~16 500 citations).
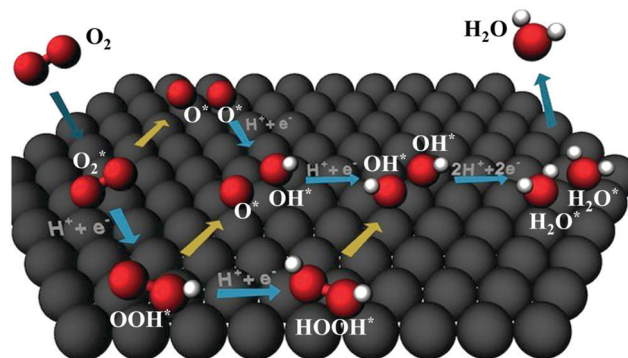
Scheme 1 Scheme of (a) proton-exchange membrane fuel cells (PEMFCs) and (b) metal–air batteries.

Scheme 2 Schematic depiction of possible principal ORR mechanisms. Reproduced with permission.[47] Copyright 2018, Wiley-VCH.

1.1 Importance of the oxygen reduction reaction in electrochemical energy devices

Although there are many advantages to proton-exchange membrane fuel cells (PEMFCs) and metal–air batteries, large-scale implementation and commercialization still face several challenges with major challenges involving the oxygen reduction reaction (ORR) at the cathode electrode. This is because the ORR greatly impacts the performance of PEMFCs due to sluggish kinetics, and although many electrocatalysts have been developed, current ORR activities are still unacceptable.[27,28] The ORR is currently one of the most extensively studied electrocatalytic reactions in energy conversion and storage devices and particularly in PEMFCs and metal–air batteries.[23,29–33] For PEMFCs, ORR catalysts are used in acidic media.[34–36] Unfortunately, due to the corrosive environment and sluggish kinetics,[37–39] ORR catalysts face greater challenges in the acidic and oxidizing environment of a PEMFC.[40] Pt-based catalysts are still the current benchmark catalysts for the ORR.[41–43] There is still a lot of room for improving the activity of non-Pt catalysts in acidic media.

For fuel cells, the ORR occurs on the cathode and proceeds through (i) a direct four-electron pathway by electro-reducing dioxygen to water as the end product ($O_2 + 4H^+ + 4e^- \rightarrow 2H_2O$

$U^{\Theta} = 1.229$ V, or $O_2 + 2H_2O + 4e^- \rightarrow 4OH^- \; U^{\Theta} = 0.401$ V),[44] or (ii) a less efficient two-step, two-electron electroreduction pathway, involving the formation of hydrogen peroxide ions as an intermediate ($O_2 + 2H^+ + 2e^- \rightarrow HOOH \; U^{\Theta} = 0.670$ V, $HOOH + 2H^+ + 2e^- \rightarrow 2H_2O \; U^{\Theta} = 1.77$ V, or $O_2 + H_2O + 2e^- \rightarrow HOO^- + OH^- \; U^{\Theta} = -0.065$ V, $HOO^- + H_2O + 2e^- \rightarrow 3OH^- \; U^{\Theta} = 0.867$ V).[20,44,45] In general, electrocatalytic ORR mainly includes species adsorption, electron transfer, proton transfer, bond breaking and formation and species desorption, and an oxygen molecule first reaches and absorbs on the catalyst surface of the electrode to form an O_2^*, followed by a decomposition process. The possible principal ORR mechanism is represented in Scheme 2. There are three pathways to reduce the O_2^*, distinguished by when the O–O bond cleavage can happen. (A) Dissociation pathway: O_2^* molecule can first dissociate into two O^* (eqn (1.1)), then the O^* continuously reacts with a hydrogen and an electron to form OH^* (eqn (1.2)) and further to a water molecule (eqn (1.3)). This pathway is relatively simple. (B) Associative pathway: the O_2^* reacts with a hydrogen and an electron to form OOH^* (eqn (2.1)) which will dissociate into O^* and OH^* (eqn (2.2)). Then, O^* will react with hydrogen and an electron

Xueliang Sun

Dr Xueliang Sun is a Canada Research Chair in Development of Nanomaterials for Clean Energy, Fellow of the Royal Society of Canada and Canadian Academy of Engineering and Full Professor at the University of Western Ontario, Canada. Dr Sun received his PhD in Materials chemistry in 1999 from the University of Manchester, UK, which he followed up by working as a postdoctoral fellow at the University of British Columbia, Canada.
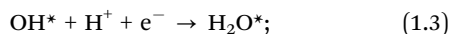

Jiujun Zhang

Dr Jiujun Zhang is a Professor at Shanghai University, Adjunct Professor at the University of British Columbia and the University of Waterloo, and former Principal Research Officer at the National Research Council of Canada Energy (NRC). Dr Zhang received his BS and MSc from Peking University in 1982 and 1985, respectively, and PhD in electrochemistry from Wuhan University in 1988. He then carried out three terms of postdoctoral research at the California Institute of Technology, York University, and the University of British Columbia. Dr Zhang has over 35 years of scientific research experience, particularly in electrochemical energy storage and conversion.

to form OH*. Finally, OH* can further react with hydrogen and an electron once again to form H_2O^*. (C) 2nd associative (peroxo) pathway (eqn (2.1′)–(2.3′)): OOH* and HOOH* are successively formed from O_2^* and then they are reduced to OH* (the cleavage of O–O bond) and further to water.[46,47]

(A) Dissociation pathway:

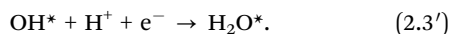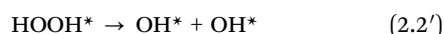$$O_2^* \rightarrow O^* + O^*, \qquad (1.1)$$

$$O^* + H^+ + e^- \rightarrow OH^*, \qquad (1.2)$$

$$OH^* + H^+ + e^- \rightarrow H_2O^*; \qquad (1.3)$$

(B) Associative pathway:

$$O_2^* + H^+ + e^- \rightarrow OOH^*, \qquad (2.1)$$

$$OOH^* \rightarrow O^* + OH^*, \qquad (2.2)$$

$$O^* + H^+ + e^- \rightarrow OH^* \qquad (2.3)$$

$$OH^* + H^+ + e^- \rightarrow H_2O^*; \qquad (2.4)$$

Or

(C) 2nd associative (peroxo) pathway:

$$O_2^* \rightarrow HOOH^*, \qquad (2.1')$$

$$HOOH^* \rightarrow OH^* + OH^* \qquad (2.2')$$

$$OH^* + H^+ + e^- \rightarrow H_2O^*. \qquad (2.3')$$
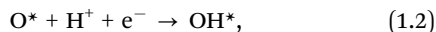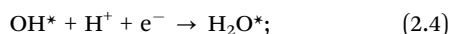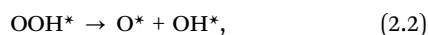
Subsequently, a multi-electron reduction reaction occurs involving a number of elementary steps and different reaction intermediates.[48] Currently, the most practical electrocatalysts are platinum (Pt)-based and can catalyze $4e^-$ ORR to produce water.[49,50]
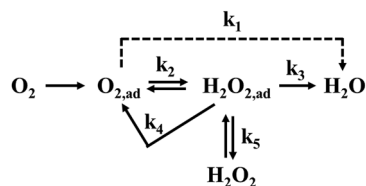
In the process of ORR, oxygen molecules can be electrochemically reduced to either H_2O or H_2O_2. Through a direct $4e^-$ pathway with a rate constant of k_1, O_2 is directly reduced to water (or OH^-) without the formation of adsorbed H_2O_2 (or HO_2^-) intermediates. Alternatively, O_2 can also be reduced through an indirect $2e^-$ pathway in which adsorbed oxygen molecules are first reduced to adsorbed H_2O_2 (or HO_2^-) with a rate constant of k_2, followed by the electrochemical reduction of the adsorbed intermediates to H_2O (or OH^-) with a rate constant of k_3, along with catalytical decomposition (k_4) or desorption (k_5).[49,51,52]

As for rechargeable metal–air batteries, the ORR occurs during the discharge process whereas the oxygen evolution reaction (OER) occurs during the charge process.[53] As the reverse reaction of the ORR, the OER is more studied under basic conditions because of the harsh conditions and large energy barrier in acidic solutions during the charge–discharge reaction processes: $4OH^- \rightleftharpoons O_2 + 2H_2O + 4e^-$. As for the testing and investigation

of ORR catalysts and reaction kinetics, the cyclic voltammetry and linear scanning voltammetry techniques, thin-film rotating disk electrode (RDE) and rotating ring-disk electrode (RRDE) techniques are normally used by researchers to obtain catalyst ORR activities and quantify electrode kinetics/mass transfer rates.[54–60]

1.2 Importance of electrocatalysts for the oxygen reduction reaction

Electrocatalysts are one of the most important cathode components in PEMFCs and metal–air batteries and play a critical role in obtaining the high performance of both devices.[61,62] Normally, the ORR on cathodes requires high overpotentials (>0.3 V, dependent on the electrode material) in the absence of electrocatalysts as a result of the sluggish reaction kinetics and hysteresis of ORR rates.[63] Therefore, to overcome this major electrochemical voltage loss, ORR electrocatalysts are generally required to speed up the process. Currently, the most effective catalysts for PEMFCs and metal–air batteries are platinum (Pt)-based materials with a typical loading of 0.1–0.5 mg cm^{-2},[59] and numerous advanced nanomaterials with unique structures have been explored with excellent ORR performances,[64,65] such as Pt_5M (M = lanthanide or alkaline earth metal) electrocatalysts,[66] Pt_3Ni nanoframes,[67] 'structurally ordered' and 'structurally disordered' PtNi catalysts,[68] ultrafine jagged platinum nanowires (J-PtNW),[69] and hollow Pt_3Ni nanoframes.[70] Among noble metal-based materials, Pt, Pd, Ru, Rh, Ir etc. have been extensively used as state-of-the-art ORR catalysts. However, the scarcity and high-cost of these noble metal materials are significant barriers in the large-scale commercialization of PEMFCs.[15,19,20,71–73] Therefore, there is an urgent need to develop inexpensive and non-noble metal catalysts that can demonstrate similar efficiencies and durability to Pt-based catalysts.[74–76] The researchers have reported that non-precious and earth-abundant transition metal (Fe, Co, Ni, etc.)-based catalysts are a class of effective ORR catalysts with proven activities and stabilities similar to commercial Pt/C catalysts,[37,77–79] and that among them, Fe–N_x–C materials are the most promising substitutes for precious metal catalysts in terms of electrocatalytic ORR activity.[80] Based on this, Fe–N_x–C catalysts have been intensively investigated in the past few decades and great progress has been made.[19,81,82] However, these non-precious transition metal catalysts are unstable, especially in acidic environments, which originates from severe leaching and larger over-potentials (40–400 mV) than commercial Pt/C catalysts.[83] Therefore, the development of non-precious metal electrocatalysts with both high ORR stability and activity comparable to commercial Pt/C catalysts is still a hot research area.

The fundamental understanding of intrinsic ORR mechanisms is another aspect in the development of high-performance electrocatalysts, particularly the elucidation of catalyst active sites for O_2 activation and catalyst–support interactions. The design of effective ORR catalysts requires oxygen-favorable reactive sites for O–O bond cleavage, optimized spatial structures for oxygen diffusion and water management and stable active sites for long term performance retention.[83] In addition, electrocatalytic reactions occur at the three-boundary zone of solid–liquid electrolyte–gas at the catalyst layer for cathodic ORR and the mechanisms of this process are complex and primarily dependent on the surface properties of the catalyst.[5,84]

This journal is © The Royal Society of Chemistry 2019

Energy Environ. Sci., 2019, 12, 2890–2923 | 2893

Therefore, theoretical studies of electrocatalytic ORR reactions and validation through experiments are the most important aspects in the development of ORR electrocatalysts. And nowadays, researchers can investigate electrocatalysts at the molecule/atom/electron level due to extraordinary developments in the accessibility of powerful computing and advanced modern characterization techniques.[5,84–86] For example, researchers can use density functional theory (DFT) calculations to study ORR kinetic processes, including electro-catalytic mechanisms, transition states and activation energies for each elementary step, rate determining steps and catalytic activities of different catalysts. Besides the work by Norskov and coworkers, some other researchers have also worked in the field of computational ORR electrocatalysis, including Timo Jacob et al.,[87] Rossmeisl et al.,[88–90] Greeley et al.,[91] Koper et al.,[92,93] and Calle-Vallejo and Sautet et al.[67,94]

The performance of catalysts is strongly associated with active site exposure and larger exposed surface areas can provide more active sites. Therefore, the fabrication of electrocatalysts with well-developed nanostructures and large surface areas is important[5] in which both theoretical and experimental studies have confirmed that the downsizing of particles or clusters to uniformly distributed single atoms is an effective method to obtain more active sites and better catalytic activities.[74,95–99]

1.3 Atomically dispersed catalysts (ADC)

1.3.1 Atomically dispersed metal catalysts (ADMCs). To increase the utilization of metal catalysts and boost ORR activity, catalyst particle sizes must be significantly reduced. This is because the downsizing of catalyst particles to the atomic scale can allow for atomic dispersion, resulting in single metal atoms anchored onto supports to maximize metal catalyst utilization and metal atom utilization efficiency (100%).[100] With decreasing metal size from bulk to nanoparticles, and then to the mono-atomic level, the specific activity per metal atom usually increases, accompanied by an increase of surface free energy,[101,102] as shown in Scheme 3. In the past decade, after a proposed concept of "single-atom catalyst" of Pt_1/FeO_x was reported in 2011,[103] atom-ically dispersed metal catalysts (ADMCs) have attracted extensive attention and have become a new frontier in the catalysis field. Up to now, most ADMCs for heterogeneous catalysis have been decorated on metal oxides (e.g., TiO_2, CeO_2, FeO_x, CoO, Al_2O_3, etc.) to avoid atom aggregation;[100,103–108] however, these catalysts are unsuitable in electrocatalytic applications due to low elec-trical conductivity and/or poor stability in strong acid or base liquid electrolytes.[109,110] Based on this, this review will summar-ize the recent advances in the preparation, characterization and catalytical ORR performance of ADMCs, along with a theoretical understanding of the corresponding structures and catalytic ORR mechanisms. In addition, challenges faced by ADMCs as well as possible research directions are provided to guide future research.

1.3.2 Dual atom catalysts. Due to the small contact areas and relatively weak interactions between single atoms and supporting materials, metal loading densities of ADMCs are usually below 1%.[105,111,112] To increase the number of single-atom active sites, dual atom catalysts and even multi-site atom catalysts can be designed. And as successfully demonstrated
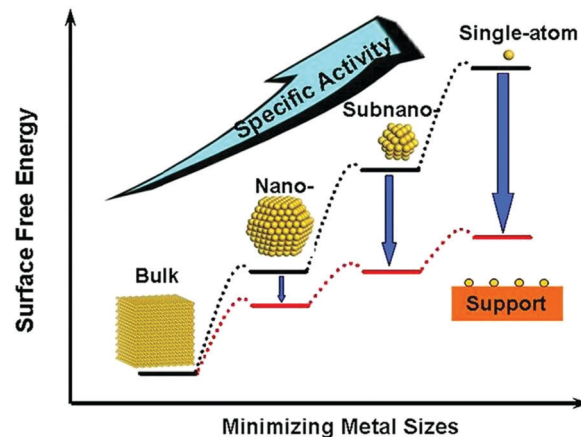
Scheme 3 Scheme of atomically dispersed metal catalysts or single-atom catalysts, and the relationship between surface free energy and metal size. Reproduced with permission.[101] Copyright 2013, American Chemical Society.

using model catalysts, metal clusters containing only a few atoms possess discrete band structures in which the alteration of one atom in the ultrafine cluster can significantly change the electronic structure of the whole cluster along with its catalytic performance.[112] Furthermore, studies have shown that dual-metal M_1, $M_2–N_x–C$ sites in macrocycle compounds are more active than single center sites[113,114] and theoretical and experimental studies have revealed that synergistic effects between M_1 and M_2 in bimetallic catalysts can significantly improve ORR performance,[115] suggesting that novel dual-atom catalysts can enhance the activation of oxygen through the effective cleavage of $O=O$ bonds, which is vital for the $4e^-$ pathway ORR process.[55,83,116–119] As an example, Zn–Co dual atomic pairs coordinated with doped nitrogen in a carbon support (Zn/CoN–C) was recently reported to be capable of enhancing binding abilities for O_2, significantly elongating the O–O length from 1.23 Å to 1.42 Å and thus facilitating the cleavage of O–O bonds.[118]

1.4 Importance of atomically dispersed catalysts

Different from conventional catalysts (supported metal nano-particles), ADMCs consist of isolated metal single atoms uni-formly dispersed on supporting materials with distinct active sites and unique chemical properties.[120–123] As a result, ADMCs are a good platform to understand structure–reactivity relation-ships at the atomic scale due to high dispersions and fully exposed active sites.[124,125] Furthermore, ADMCs possess uni-form single-atom dispersions and well-defined configurations and can provide a great platform to optimize high selectivity and activity. Currently, an important aspect of ADMCs is to ration-ally design and synthesize materials at the atomic level, allowing for increased metal loading and active sites along with improved intrinsic activity for each active site toward the ORR.[54,126] Here, the precise synthesis of ADMCs can be challenging due to the lack of a conclusive correlation between structure and electro-catalytic performance. In addition, it is also difficult to balance metal loading and the dispersal state of ADMCs because

2894 | Energy Environ. Sci., 2019, **12**, 2890–2923

This journal is © The Royal Society of Chemistry 2019

decreased particle sizes can lead to increased surface free energies and increased chemical interactions between adsorbates and metal sites on supports,[101] leading to ADMC agglomerations due to the high free energy of metal atoms during material sintering and increasing metal loading processes.[127–130] Furthermore, more accessible metal active sites during catalytic processes can lead to the easier formation of larger clusters or nanoparticles from isolated single metal atom species.[131]

Finally, a deeper understanding of the ORR catalytic mechanism of ADMCs is needed, including the identification of active sites at the atomic level and the interactions between ADMCs and support materials,[132–134] as well as the optimization of ADMC catalytic activities through the tuning of single metal atom coordination environments.[54] Theoretical calculations can be used to help in the understanding of the nature of active centers, metal atom–support interactions, and evaluations of catalytic activity. This in turn will guide the rational design of efficient ADMCs with ideal nanostructures and high ORR activities.

2. Synthesis strategies

Controlled synthesis strategies play a fundamental role in the preparation of uniformly dispersed single metal atoms on appropriate supports and can facilitate synergistic interactions between catalyst atoms and supports, leading to high-performance ORR catalysts. And based on the integration mode of components, ADMC fabrication approaches can be categorized into bottom-up and top-down strategies, in which currently, the majority of ADMCs are produced through the bottom-up strategy, including atomic layer deposition, high-energy bottom-up ball milling, photochemical strategies, mass-selected soft-landing methods, *etc.* In general, bottom-up precursors are adsorbed/anchored, reduced and confined by defects on oxides or carbon supports with plenty of N or O defects or vacancies.[61,101,135] Alternatively, top-down approaches involve the disbanding of well-organized nanostructures into smaller pieces with desired properties mainly through high-temperature pyrolysis and high-temperature gas-phase migration.[135,136]

In practice however, the fabrication of ADMCs is challenging due to their mobility and their tendency to aggregate resulting from high surface energies.[137] Therefore, inhibition strategies for agglomeration or surface uncapped sites play a significant role in the stabilization of single metal atom catalysts. Here, an effective method to increase the stability of ADMCs is to strongly anchor metal single atoms onto substrates with high surface areas, such as carbon, oxide, nitrides, sulfide, *etc.*, to lower free energies and form highly stable and reactive catalytic active centers for desired catalytic reactions.[120,138] Commonly used strategies for the preparation of ADMCs are summarized in Table 1, and more detailed discussions concerning Table 1 are as follows.

2.1 Wet-chemistry approach

With advantages such as ease of operation and possible large scale production, wet-chemistry approaches can be routinely carried out in any wet chemistry lab without specialized equipment.

In addition, wet-chemical approaches are currently the most promising and successful methods to synthesize ADMCs.[61,135] The common procedure of the wet-chemistry approach for preparing desired ADMCs includes precursor adsorption onto substrates with (or within) N sources (urea, NH_3, melamine, cyanamide, *etc.*), followed by drying, calcination and reduction or activation processes. Here, N sources such as melamine and NH_3 can be introduced during the post-treatment step and in the initial step, metal complexes or precursors (*e.g.*, Fe, Co, Ni, Cu, or Pt) are anchored onto carbon supports (*e.g.*, graphene, glucose, chitosan, or MN_4C_4 moiety) through coordination effects arising from co-precipitation,[127,186] impregnation/ion-exchange[135,140,187] and/or deposition precipitation methods.[131] For example, Wei *et al.*[188] used the co-precipitation method to prepare a series of Pt/FeO_x catalysts at 50 °C with chloroplatinic acid ($H_2PtCl_6\cdot6H_2O$) and ferric nitrate ($Fe(NO_3)_3\cdot9H_2O$) as metal precursors and sodium carbonate (Na_2CO_3) as the precipitating agent. The as-prepared catalysts were used for chemo-selective hydrogenation of 3-nitrostyrene with a yield of ~1500 h^{-1}, which is 20-fold higher than the optimal results reported in the literature at that time.

Although wet chemistry approaches are operationally easy and applicable to large-scale production without special equipment, disadvantages include the possible burial of metals either in the interfacial region or within the support bulk during co-precipitation. In addition, co-precipitation results in the easy formation of ADMCs on metal oxide supports and these metal oxide supports are not appropriate for electrochemical testing because of their low conductivity and weak stability under acidic conditions.[65] Furthermore, strong affinity between support surfaces and metal complexes or single metal atoms allows for the easy formation of nanoparticles or clusters in solutions or on supports, especially with increased metal loading.[131,135]

2.2 High-temperature pyrolysis method

High-temperature pyrolysis is a top-down approach to synthesize ADMCs through the thermal decomposition of select precursors at appropriate pyrolysis temperatures (*e.g.*, 600–1000 °C) in which the selection of temperature is vital to obtain high-performance ORR ADMCs.[135] As for the preparation process, specific precursors containing metal (M = Co, Fe, Ni, *etc.*), N (and/or S) and C elements are treated under a protective atmosphere (*e.g.*, N_2, Ar, H_2, or NH_3) and the precursors can be summarized as follows:

(1) **Metal-containing complexes or mixtures of specific precursors.** As alternatives to precious Pt, transition metal-containing complexes such as iron or cobalt organic macrocycles and covalent triazine frameworks (CTFs) have been widely used as precursors to prepare ORR catalysts[189–191] and in recent years, numerous transition metal $M–N_x–C$ (M = Fe, Co, Ni, Zn, Mn, Cu, *etc.*) species have been reported as promising ORR electrocatalysts with unexpected reactivity and outstanding durability.[38,39,74] In addition, electrochemical results have shown that they can also provide high selectivity towards the ORR and methanol tolerance in direct methanol fuel cells (DMFCs).[64] And of these $M–N_x–C$ nanostructures, $Fe–N_x$ species possess superior ORR electrocatalytic activity due to strong interactions between Fe

This journal is © The Royal Society of Chemistry 2019

Energy Environ. Sci., 2019, **12**, 2890–2923 | **2895**

Table 1 Strategies for the preparation of ADMCs along with the corresponding materials, catalyst loadings, and comparisons of the advantages and disadvantages of each method

Synthesis method	Materials	Application	Loading	Ref.	Notes
Wet chemistry strategy	FeCo-ISAs/CN	ORR	Fe 0.964 wt%, Co 0.218 wt%	139	Advantage: no need for specialized equipment, easy operation and possible large-scale production.
	Pt/TiN	ORR	0.35 wt%	140	Disadvantage: metals might become buried and the easy formation of nanoparticles or clusters.
	Pt1/TiC; Pt1/TiN	ORR H_2O_2 reduction	0.2 wt%; 0.2 wt%	141	
	Au_1/C_3N_4	NRR	0.15%	142	
	Rh_1/VO_2	AB hydrolysis	0.5 wt%	123	
	A-Co/r-GO	ORR	3.6 wt%	143	
	Pt_1@Fe–N–C	ORR/HER/OER	2.1 wt% Pt	144	
	Pt–CN	Photocatalytic H_2 evolution	0.075 wt%, 0.11 wt%, 0.16 wt%	145	
	Zn–N–C	ORR	9.33 wt% (2.06 atom%)	146	
	Pt_1/hNCNC	HER	0.75 to 1.48, 2.92, and 5.68 wt%	147	
High-temperature pyrolysis of MOFs	Fe-ISA/NC	ORR	0.947 wt%	148	Advantage: precise control over the size of MOF-derived carbon supports and interconnected 3D molecular-scale cages offering abundant mass transfer channels and active nitrogen sites.
	Fe-ISAs/CN	ORR	2.16 wt%	149	Disadvantage: low carbonization ratios, tedious procedures and extreme difficulty in the modification of the molecular structure and surface properties of resulting ADMCs at such high temperatures.
	S,N–Fe/N/C-CNT	OER/ORR	—	23	
	Co-SAs/N–C-900	ORR	4 wt%	99	
	Co-SAs/N–C-800	ORR			
	Fe50-N–C-900	ORR	0.1 mg cm^{-2} 0.3 mg cm^{-2}	31	
	NC-Co SA	ORR	1.84 wt%	150	
	Co_2N_xC	ORR	—	55	
	Fe,Co/N–C	ORR	—	83	
	Ni SAs/N–C	CO_2RR	1.53%	151	
	CoN_4/GN	DSSCs	—	152	
	CoPc/CNT	CO_2RR	6%	153	
	Ni–N	CO_2RR	4 wt%	14	
	Ni–S		2.5 wt%		
	Pd_1/TiO_2	Hydrogenation of C=C bonds	1.5%	105	
	Pt/FeO$_x$ SAC	DSSC	0.08–2.40%	154	
	Co-NG	HER	0.57 at%	98	
	Ru SAs/N–C	Hydrogenation of quinoline	0.30 wt%	155	
	Fe$_{SA}$–N–C	ORR	1.76 wt%	156	
	Fe SAs–N/C-20	ORR	0.20 wt%	157	
	A-PtCo-NC	ORR	Co: 1.72 wt%; Pt: 0.16 wt%	158	
	Co-SAs@NC	ORR	1.70 wt%	159	
	20Co-NC-1100	ORR 0.80 V, 0.5 M H_2SO_4	0.34 at%	160	
High-temperature pyrolysis of metal-containing complexes or mixtures of specific precursors	(CM + PANI)–Fe–C	ORR	0.2 at%	161	Advantages: top-down approach to synthesize ADMCs through the thermal decomposition of select precursors at appropriate pyrolysis temperatures.
	SA–Fe/CN	Benzene conversion	0.9 wt%	162	Disadvantage: low carbonization ratios, tedious procedures, and extreme difficulty in the modification of the molecular structure and surface properties of the resulting ADMCs at such high temperatures.
	CoNC700	ORR	0.73 at%	163	
	CoSAs@CNTs	ORR	0.14 at%	164	
	ZnN$_x$/BP	ORR	0.3 wt%	165	
	Zn/CoN-C	ORR	Zn 0.33 wt%; Co 0.14 wt%	118	
	(Zn,Co)/NSC	ORR	—	119	
	FeSAs/PTF-600	ORR	8.3 wt%	166	
	Fe-NGM	ORR	0.21 at%	167	
	Fe-NGM/C–Fe		0.53 at%		
	SA–Fe/NHPC	ORR	2.3 wt%	168	
	Co-ISAS/p-CN nanospheres	ORR	0.42 wt%	169	
	NGM-Co	ORR	0.18 at%	170	

Table 1 (continued)

Synthesis method	Materials	Application	Loading	Ref.	Notes
Template-assisted pyrolysis approach	Fe–N-SCCFs	ORR	0.8 at% BET 1180 m^2 g^{-1}	125	Advantage: structural integrity in large-scale production with controlled morphology.
	Single-atom Ni-doped graphene	HER	4–8 at%	171	Disadvantage: tedious operation processes, structure destroyed during the hard template removal process along with the introduction of impurities, strong acid/base or organic solvents used in the removal of templates are not environmentally-friendly.
	FeN_2/NOMC-3	ORR FeN_2	0.35 at%	172	
	Fe–NCCs	ORR	0.26 at%	173	
	Fe–N-CNTAs-5-900	ORR	0.09 at%	174	
Surfactant-assisted pyrolysis process	SA–Fe/NG	ORR	2.0 mg cm^{-2}	175	Advantage: effective and facile method that can be easily extended to the synthesis of other ADMCs, relatively easy to remove the soft template.
	CoN_4/NG	ORR	11.4 mF cm^{-2}	176	Disadvantage: worse stability of the soft template due to weak intermolecular or intramolecular interactions.
	Pd/meso-Al_2O_3	Selective aerobic oxidation of allylic alcohols	0.03 wt%	108	
Atomic layer deposition (ALD) method	Nb-in-C complex	ORR	60 µg cm^{-2}	177	Advantage: bottom-up precise synthesis of ADMCs with accurate control of atom layers with extremely uniform thicknesses, excellent uniformity and shape retention.
	Pd_1/graphene	Selective hydrogenation of 1,3-butadiene	0.25 wt%	158	Disadvantage: expensive, slow deposition rates and low yields limit large-scale production.
	ALD25Pt/NGNs	HER	0.19 wt%	122	
	ALD TiO_2 stabilized Pd1 catalysts	Methanol decomposition	0.5 wt%	178	
	ALDPt/GNS	MOR	—	179	
	Pt_1/graphene Pt_2/graphene	AB hydrolysis	—	112	
Nanoparticle transforming method	Cu-SAs/N–C	ORR	0.54 wt%	180	Advantage: great potential for large-scale production and readily scalable at industrial levels.
	Cu-SAs/N–G		1.26 wt%		Disadvantage: presence of agglomeration and atomization competition in the dynamic transformation process of NP-to-SA.
	Pt/La-Al_2O_3	CO oxidation	1 wt%	104	
	Pd-SAs	Acetylene conversion	—	181	
	SE-Ni SAs@PNC	CO_2RR	—	182	
	Pt SAs/DG	HER	2.1 wt%	183	
High-energy ball milling synthesis	Fe©SiO_2	Conversion of methane	0.5 wt%	184	Advantage: high efficiency in the breaking and reconstructing of material chemical bonds, favorable for large-scale preparation.
	CoN_4/GN	DDSC	—	152	Disadvantage: low powder yields, raw material wastage and long-time consumption.
	FeN_4/GN	Oxidation of benzene	1.5%	185	

NRR: nitrogen reduction reaction. DDSC: dye-sensitized solar cells. CO_2RR: carbon dioxide reduction reaction. AB hydrolysis: ammonia–borane hydrolysis.

and N species in carbon matrixes[23] whereas Co–N_x–C catalysts are more stable.[55]

(2) **Metal organic frameworks (MOFs).** As prospective precursors in the design of novel porous nanocarbon-based electrocatalysts, metal organic frameworks (MOFs) and MOF-derived materials have attracted intense attention in recent years. This is because MOFs possess a 3D ordered crystal framework structure and can be modularly constructed using bridging metal ions/clusters as nodes and functionalized organic ligands as struts[192,193] in which the ORR primarily occurs at the triple-phase boundary with the active material electrode (solid) being in intimate contact with oxygen molecules (gas) and the ion-conducting electrolyte (liquid).[194,195] The coupling of ADMCs with porous nanostructured electrodes can simultaneously increase the number of active sites and improve their reactivity.[54] Furthermore, MOF-derived electrocatalysts possess a highly ordered porous structure with uniform pore diameter distribution ratios, plentiful permanent open channels and nanoscale cavities, offering congenial situations for small molecules to access.[196] In particular, MOFs possess high surface areas, well-defined porosities, large pore volumes, diverse structures and adjustable functionalities as well as flexible tunability in compositions and a readily self-sacrificial nature.[192,197–199] In addition, MOF-based catalysts with high surface areas and uniformly distributed active sites can be formed without the addition of carbon supports or pore forming agents and the large surface area is conducive

This journal is © The Royal Society of Chemistry 2019

Energy Environ. Sci., 2019, **12**, 2890–2923 | **2897**

to the dispersion of active components and sites for electrocatalytic ORR.

Among the various MOF materials, zeolitic imidazolate frameworks (ZIFs) and derivatives such as ZIF-8 and ZIF-67 are the most common precursors used due to their easy preparation and high ORR performances. And during the pyrolysis of these MOF materials, doped metal precursors can transform into single atoms with Zn species being removed under Ar flow due to their low boiling point at $\sim 907°$, resulting in isolated metal ions that are closely confined in the MOF-derived support through N-coordination, thus avoiding aggregation during high-temperature pyrolysis.[23,200,201] For example, Zhang et al.[202] synthesized well-dispersed atomic Fe sites anchored onto porous carbon by directly bonding Fe ions onto imidazolate ligands within a 3D framework in which no aggregation was observed. The researchers explained the active site formation process by associating the measured ORR activity with the chemical bond change during the thermal activation procedure and found the formation of new Fe species with a reduced oxidation state (from Fe^{3+} to Fe^{2+}) as active sites at a critical temperature of 800 °C.

Thus, a series of MOF-derived single atom catalysts through high-temperature pyrolysis have been reported in the literature.[83,99,148,149,181,203] For example, Wang et al.[83] recently reported a high-performance single atom ORR catalyst on N-doped porous carbon with Fe–Co dual sites ((Fe,Co)/N–C) in which a Zn/Co bimetallic MOF (BMOF) with Co^{2+} and Zn^{2+} nodes in the metal–organic framework (ZIF-8 structure) acted as the host and adsorbed Fe ions acted as the guest (Fig. 1). The researchers reported several associated conversions occurring during the pyrolysis process and that Zn species can be removed under Ar flow due to a low boiling point at ~ 1173 K. Furthermore, the researchers reported that Fe^{3+} moieties can be reduced by as-generated carbon and in turn modulate the geometric structure of the carbon support to form N-doped graphene and that these Fe species can not only accelerate the decomposition of metal–imidazolate–metal links and drive the generation of voids inside the MOFs, but also bond with neighboring Co atoms to form Fe, Co-dual atomic sites. In addition, successive decomposition and graphitization in the process reportedly led to inner cavities and size enlargements through the Kirkendall effect.

In another example, Chen et al.[149] prepared isolated Fe atoms anchored onto N-doped porous carbon (Fe-ISAs/CN) by encapsulating $Fe(acac)_3$ precursors into molecular cages with a zeolitic imidazolate framework (ZIF-8) structure. In this case, the ZIF-8 structure (cavity diameter (d_c): 11.6 Å, pore diameter (d_p): 3.4 Å) can act as molecular-scale cages to encapsulate and separate $Fe(acac)_3$ precursors (molecular diameter, ca. 9.7 Å) in which one $Fe(acac)_3$ molecule can be trapped in one molecular-scale cage originating from the assembly of Zn^{2+} and 2-methylimidazole (denoted as $Fe(acac)_3$@ZIF-8). And upon subsequent pyrolysis at 900 °C for 3 hours under flowing argon, ZIF-8 frameworks can be transformed into N-doped porous carbon (CN) whereas $Fe(acac)_3$ trapped in the cage can be reduced by carbonized organic linkers to form isolated single Fe atoms anchored onto N-doped porous carbon (Fe-ISAs/CN). And by using this method, the researchers reported that the Fe loading of the isolated Fe-ISAs/CN can reach 2.16 wt% and provide superior ORR performances as compared with Pt/C catalysts in alkaline solution. Furthermore, Xiao et al.[55] synthesized novel atomic-scale binuclear Co_2N_5 sites through the pyrolysis of a bimetal–organic framework (ZnCo-ZIF) and reported that the metal atoms can be effectively spatially confined in the MOF precursors to suppress their agglomeration during pyrolysis. The researchers further conducted theoretical analysis of the obtained material and reported that the Co–Co distance was 2.21 Å, which was assigned to the Co_2N_5 structure. The intrinsic activity of Co_2N_5 can reach 3734 mA mg_{Co}^{-1}, which is ~ 12 times higher than that of single atomic CoN_4 sites. The binuclear site (Co_2N_5) structure with a Co–Co distance of 2.21 Å showed much higher ORR activities, which was attributed to significantly reduced thermodynamic barriers due to the formation of the binuclear site structure. Here, the term "thermodynamic barrier" is related to the largest of the endothermic steps. A low thermodynamic barrier corresponds to a situation in which only a low overpotential is necessary for the onset of the reaction.
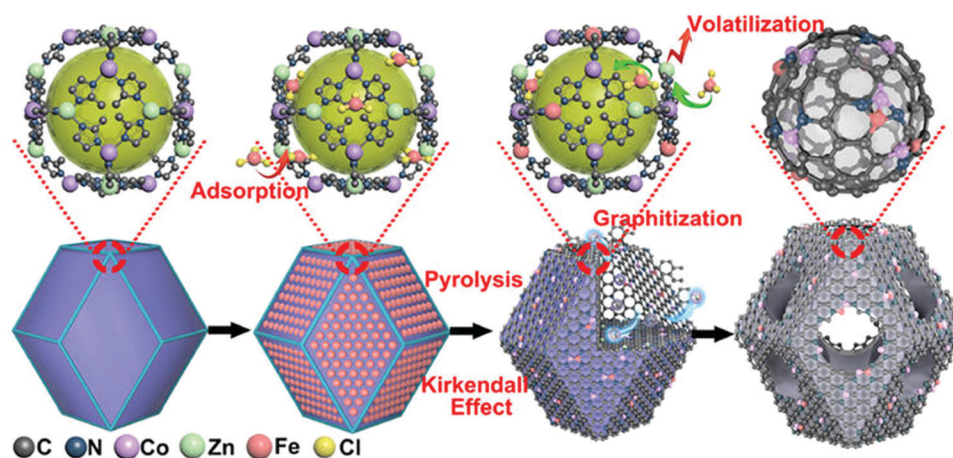
Fig. 1 Synthetic procedure of (Fe,Co)/N−C. Co nodes in the metal−organic framework acted as the host and adsorbed Fe ions as the guest. Continuous decomposition and graphitization can result in interior cavities and size enlargements through the Kirkendall effect. Reproduced with permission.[83] Copyright 2017, American Chemical Society.

2898 | Energy Environ. Sci., 2019, **12**, 2890–2923

This journal is © The Royal Society of Chemistry 2019

In another study, Yang et al.[175] synthesized a single-atom iron catalyst supported on g-C_3N_4 substrates (SA–Fe/NG) through a surfactant-assisted pyrolysis process. As reported, Fe precursors were first doped into surfactant F127 sheets and subsequently tightly anchored onto g-C_3N_4 substrates. During the pyrolysis process, Fe can easily coordinate with nitrogen and form Fe@ pyrrolic N(C) active sites for the ORR.

Based on systematic investigations of the relationship between precursor structures and catalyst activity, metal–ligand compositions can be rationally designed with a wide selection of metal–linker combinations.[204] In addition, surface areas and pore sizes of MOF-derived carbon catalysts can be tuned by controlling organic linker lengths which are converted to carbon during the thermal activation process. However, high-temperature pyrolysis also often generates complex species such as M(0), MO_x, M–N_x and corresponding mixtures that are tens of nanometers in size.[121,124] In addition, direct pyrolysis strategies require improvements due to the agglomeration of metal ions/atoms into nanoparticles during the drastically reactive process at high temperatures.

(3) Template-assisted pyrolysis approach. The creation of carbon-based nanomaterials with 3D porous structures is another strategy to enhance ORR performance. This is because 3D porous structures can provide high surface areas with abundant exposed active sites, faster mass transport/diffusion and more effective electron-transfer pathways.[174,205,206] Furthermore, the template-sacrificial method is an efficient approach to create 3D porous carbon-based M–N–C nanocatalysts with high ORR performance in which the high-temperature pyrolysis of MOFs can be classified into hard and soft template approaches.

Hard template. The hard template approach employs metal hydroxides or oxides (e.g., silica nanoparticles, SBA, α-FeOOH nanorods, Mg(OH)$_2$, zeolite, Te nanowires) as sacrificial templates and small organic molecules, metal complexes or polymers (e.g., CCl_4, glucosamine, dopamine, metalloporphyrins) as carbon precursors.[54,111,162,172,174,203,207,208] For example, Zhu et al.[54] recently developed a bimodal template-based synthesis strategy to produce hierarchically porous M–N–C (M = Fe or Co) single atom electrocatalysts with robust MN_2 active sites in which a mixture of silica sol suspension, metal precursor ($FeCl_3$ or $CoCl_2$), $ZnCl_2$ and glucosamine was subjected to freeze drying (Fig. 2a) followed by pyrolysis at 900 °C for 2 hours under flowing nitrogen and template removal using hydrofluoric acid to obtain hierarchically porous Fe or Co–N–C single-atom electrocatalysts. The researchers reported that cobalt/iron salts and small glucosamine molecules acted as precursors and silica nanoparticles and zinc chloride acted as porosity-inducing templates, and that the addition of zinc chloride was essential to create more porous nanostructures. In another example, Shen et al.[172] designed a new template casting procedure to prepare atomically dispersed FeN_2 moieties on N-doped ordered mesoporous carbon (FeN_2/NOMC) through a hard template
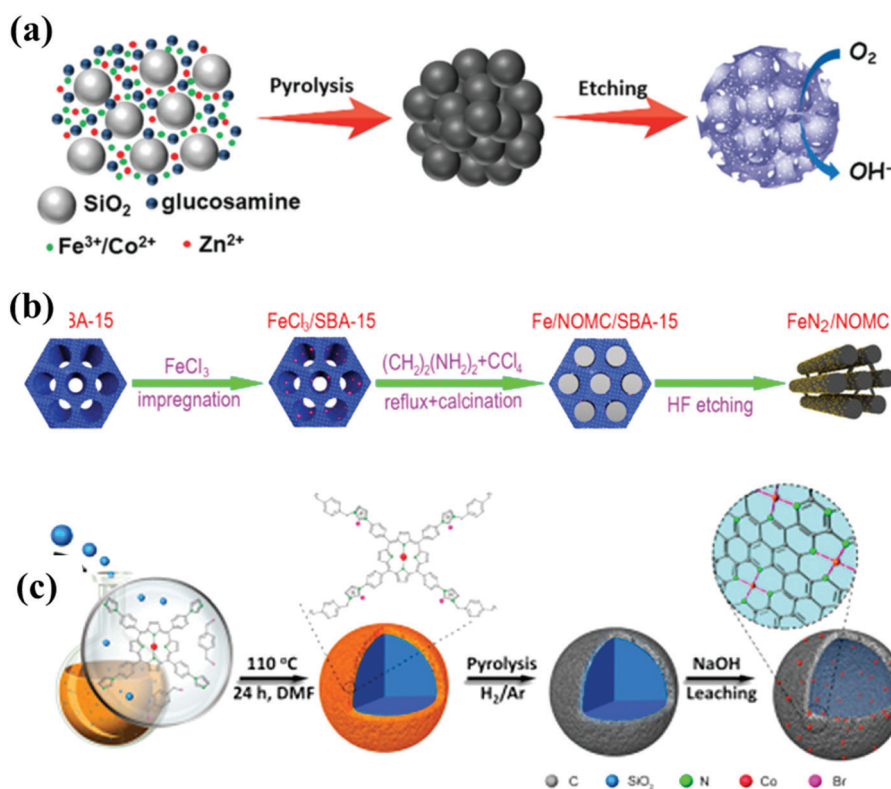
Fig. 2 Schematics of the synthetic procedures for single-atom electrocatalysts using the hard template process: (a) hierarchically porous M–N–C (M = Co and Fe) ADMCs; reproduced with permission.[54] Copyright 2018, Wiley-VCH. (b) FeN_2/NOMC; reproduced with permission.[172] Copyright 2017, Elsevier Ltd. (c) ISAS-Co/HNCS. Reproduced with permission.[209] Copyright 2017, American Chemical Society.

This journal is © The Royal Society of Chemistry 2019

Energy Environ. Sci., 2019, **12**, 2890–2923 | **2899**

approach (Fig. 2b) involving iron ion deposition onto the surface of SBA-15 through impregnation to ensure the uniform dispersion and availability of Fe on the surface of the support, polymerization by refluxing the mixture of iron ethylenediamine (EDA) and CCl_4 at 90 °C for 6 hours to obtain a dark-brown solid mixture and subsequent carbonization at 900 °C for 3 hours and HF etching to obtain the final product composed of atomic Fe elements anchored along the surface/edges of the carbon support. The researchers reported that this anchoring effect of iron on the template can prevent diffusion in the carbon skeleton during the carbonation process. Furthermore, Han et al.[209] reported a series of isolated single metal atom electrocatalysts supported on N-doped carbon spheres through a hard template-assisted pyrolysis approach in which isolated Co, Fe, or Cu-ADMCs dispersed on hollow N-doped carbon spheres (ISAS-M/HNCS) were prepared by using SiO_2 as the template and metalloporphyrins (M-TIPP, M = Co, Fe, Cu, etc.) as the monomers (Fig. 2c). SiO_2 nanoparticles were first prepared and dispersed into a M-TIPP/TIPP solution to obtain a SiO_2@M-TIPP/TIPP polymer followed by thermal treatment at 800 °C for 3 hours under flowing H_2/Ar. The SiO_2 template is subsequently removed with etching agents (sodium hydroxide) to yield the final ISAS-M/HNCS. And, the researchers reported that the ISAS-Co/HNCS demonstrated high ORR catalytic activity. This was attributed to the single Co sites which can significantly improve the transfer of protons and charges onto adsorbed *OH species. Using a similar hard template approach, Chen et al. also prepared a Mo ADMC with sodium molybdate and chitosan as precursors and reported that in the catalyst, Mo atoms were confirmed to be anchored to one nitrogen atom and two carbon atoms ($Mo_1N_1C_2$).[203] Furthermore, Zhang et al.[162] also developed a series of different metal single atoms dispersed on hollow nitrogen-doped carbon (CN) supports (SA-M/CN, M = Fe, Co, Ni, Mn, etc.). For example, a SA–Fe/CN catalyst was obtained using α-FeOOH nanorods as the template and metal precursor and polydopamine as the precursor for the CN shell. α-FeOOH nanorods were first prepared through a hydrothermal method followed by polydopamine (PDA) coating through a self-polymerization process to form FeOOH/PDA. This material was subsequently subjected to a thermal carbonization procedure to convert the PDA layer of the FeOOH/PDA into the support and reduce the α-FeOOH to iron atoms, enabling strong interactions between Fe atoms and CN. Finally, acid leaching was carried out to etch and remove unstable species, resulting in iron single atoms on the inner wall of CN shells. The researchers reported that by changing the metal precursors (Fe, Co, Ni, etc.) or polymer monomers (dopamine, aniline, pyrrole, etc.), SA-M/CN with dual sites of FeNi, FeCo can be successfully synthesized, suggesting the universality of this synthetic method. Through a similar template-sacrificial approach using $Mg(OH)_2$ or nano-MgO support as the hard template, Liu et al.[207,210] in their studies synthesized a series of self-supporting catalysts of single-atom dispersed Co, or Fe–N–C in which $Co(phen)_2(OAc)_2$ or $Fe(phen)_x$ complexes were supported on $Mg(OH)_2$ or nano-MgO supports and subjected to pyrolysis followed by acid leaching to remove the MgO support. As a result, the researchers reported that the introduction

of $Mg(OH)_2$ can effectively prevent cobalt or iron atom aggregation.[174,206,207,209,210]

Zeolite-templated carbon (ZTC) with a unique carbon structure of highly curved 3D graphene nanoribbon networks is another potential support for ADMCs with a relatively high metal loading. For example, Choi et al.[111] synthesized a single Pt atom catalyst with relatively high loading (5 wt%) on a high sulfur-doped ZTC support (Pt/HSC) and reported that the unique carbon structure with the highly doped sulfur enabled the high loading of atomically dispersed Pt and characterization results confirmed that single Pt atoms existed in the form of Pt^{2+} species which was linked to approximately four S-moieties.

Soft template. Surfactant-assisted pyrolysis is an effective and facile synthetic strategy to prepare ADMCs. For example, Yang et al.[175,176] developed a series of Fe- and Co-based ADMCs using water-soluble surfactant F127 (polyoxyethylene–polyoxypropylene– polyoxyethylene (PEO–PPO–PEO)) through surfactant-assisted pyrolysis. In their experiment, the precursors of g-C_3N_4, metal salt and F127 complex were uniformly mixed using sonication in which metal-adsorbed surfactant F127 moieties can penetrate g-C_3N_4 substrate interlayers. Following this, the homogeneous system was carbonized at 550 °C for 2 hours and pyrolyzed at 800 °C for another 2 hours in a N_2 atmosphere. The researchers reported that the negatively charged F127 surfactant can play a critical role in the strong attraction of positive metal ions (Fe^{3+}, Co^{2+}) and was vital for the uniform dispersion of single metal atoms in g-C_3N_4 layers. In another study, Zhang et al.[107] employed a self-assembly method with modified sol–gel solvent vaporization to synthesize thermally stable single atom Pt/m-Al_2O_3. In this synthesis process, after ethanol evaporation at 60 °C, an ethanolic mixture of triblock copolymer P123, aluminum isopropoxide ($C_9H_{21}AlO_3$) and H_2PtCl_6 self-assembled into a highly-ordered hexagonally-arranged mesoporous gel structure with the encapsulation of Pt precursors. This as-obtained gel matrix was subsequently calcined in air to decompose the P123 template and allowed for the transformation of the aluminum isopropoxide into a rigid and well-aligned mesoporous Al_2O_3 framework. Finally, a reducing step in 5% H_2/N_2 at 400 °C was carried out to obtain isolated Pt SAs stabilized by unsaturated pentahedral Al^{3+} centers.

In general, hard templates possess high stability and well-defined structures in which the structural integrity of the template is retained, even in large-scale preparation. However, disadvantages include tedious operation processes, structural deformation during synthesis and the introduction of impurities. In addition, the removal of used templates under harsh conditions using strong acids/bases or organic solvents is not environmentally-friendly.[211,212] As for the soft template method, used templates are relatively easier to remove; however, soft templates often possess worse stability due to weak intermolecular or intramolecular interactions.

2.3 Atomic layer deposition (ALD)

Atomic layer deposition (ALD) is a sequential film growth process based on the self-terminating surface reaction between gas phase metallic precursors and solid substrates. Through the

2900 | Energy Environ. Sci., 2019, 12, 2890–2923

This journal is © The Royal Society of Chemistry 2019

alternative sequential exposure of solid surfaces (growing films) to pulsing vapors of metallic precursor molecules, sequential deposition of sub-monolayers or monolayer(s) can be obtained.[213,214] Deposition is based on chemisorption which only occurs on reactive surface sites and can lead to self-limited coordination and area-selective ALD.[215] Therefore, as a method for synthesizing precise-controlled nanoparticles and clusters, ALD is a promising and powerful technique to synthesize ADMCs with precise-controlled stability. In addition, ALD is also useful in the exploration of structure–performance relationships in ADMCs.[122,158,178] For example, Sun et al.[179] anchored isolated Pt atoms onto graphene nanosheets using an ALD technique with oxygen and (methylcyclo-pentadienyl)-trimethyl platinum ($MeCpPtMe_3$) as precursors. The researchers reported that through the use of ALD the Pt content of the catalyst can be varied from isolated single atoms to sub-nanometer sized clusters up to nanoscale particles and that the as-synthesized ADMCs exhibited better electrocatalytic activity than the commercial Pt/C catalysts. In another example, Zhang et al.[177] incorporated single niobium atoms into graphitic layers (Nb-in-C) as ORR catalysts using ALD and reported, through a combination of experimental testing and theoretical simulation, that the Nb-in-C complex could undergo a rearrangement of d-band electrons, which was thought to be favorable for the adsorption and dissociation of oxygen molecules. The researchers in this study also reported that the strategy of incorporating single niobium atoms can enhance the overall conductivity and accelerate the exchange of ions and electrons, as well as suppress the chemical/thermal coarsening of active particles. Furthermore, Yan et al.[112] fabricated a Pt_2 dimer through a bottom-up strategy by depositing Pt onto a graphene support using ALD in which the resulting material was obtained through a surface self-limiting reaction between $MeCpPtMe_3$ and graphene nanosheets. The isolated nucleation sites (anchor sites) of phenols or phenol–carbonyl pairs were controllably generated through both acid oxidation and high-temperature thermal reduction and the first cycle of Pt ALD on the nucleation sites was carried out through alternating exposure to $MeCpPtMe_3$ and molecular O_2 at 250 °C, with the second cycle

involving the selective deposition of secondary Pt atoms onto Pt_1/graphene at 150 °C (Fig. 3). The researchers claimed that Pt precursors, temperature and post-treatment atmospheres all played crucial roles in this diatomic catalyst preparation process.

In general, ALD with sequential surface saturated reactions and self-limited surface chemical reactions can guarantee accurate control of atom layers and step coverage, affording promising prospects for the homogeneous deposition of ADMCs onto large-scale 3D porous structures with high aspect ratios.[213,215] Therefore, ALD nanocavities can form the basis for the large-scale construction of highly efficient and stable single-atom catalysts at the atomic scale through the accurate control of the structure and composition of related supports.[178] However, disadvantages such as high costs and slow deposition rates need to be addressed.

2.4 Gas migration strategies (nanoparticle transforming method: NP-to-SA)

Presently, although researchers have developed numerous pre-paration methods for ADMCs, most of these methods involve complex processes and large-scale approaches are still not available. However, researchers reported, in 2016, thermally stable single platinum atoms supported on ceria[104] and demon-strated that metal nanoparticle transformation is an effective approach to prepare thermally stable single atoms (NP-to-SA). In that study, Jones et al.[104] found that Pt nanoparticles supported on alumina can be transferred onto ceria supports in air at 800 °C and that high temperatures can guarantee that only the most stable binding sites are occupied, yielding thermally stable and sinter-resistant single atoms. In addition, these researchers also found that polyhedral- and nanorod-ceria were more effective at anchoring Pt than cube-ceria. In a subsequent study, Wei et al.[181] directly observed the dynamic transformation process of noble metal (Pd, Pt, and Au) nanoparticles to thermally stable single atoms using in situ environmental transmission electron microscopy (ETEM). In addition, the researchers reported that they also clearly observed and recorded the competing process between sintering and atomization during NP-to-SA conversion.
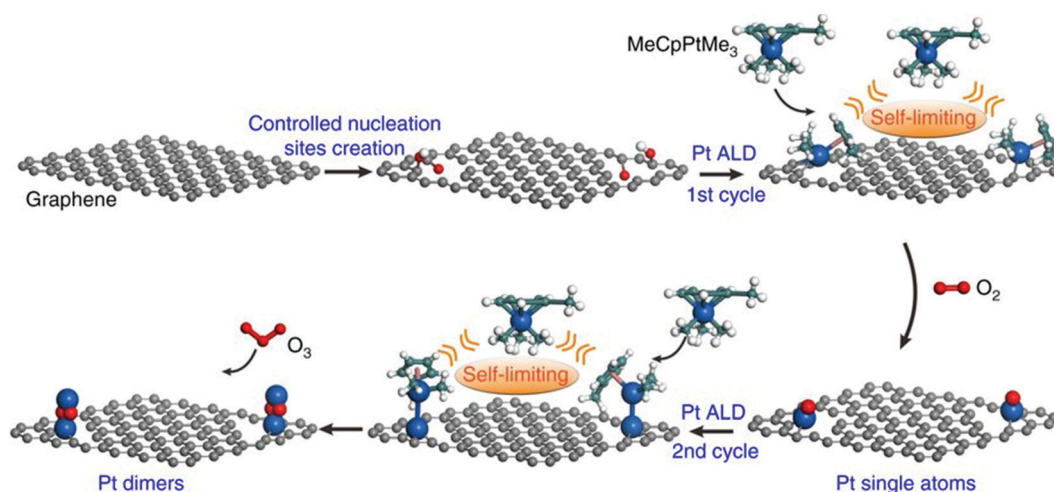

Fig. 3 Schematic for the preparation of dimeric Pt_2/graphene catalysts through a bottom-up ALD approach. Reproduced with permission.[112] Copyright 2017, Nature Publishing Group (NPG).

This journal is © The Royal Society of Chemistry 2019

Energy Environ. Sci., 2019, **12**, 2890–2923 | **2901**

DFT calculations were carried out which further confirmed that NP-to-SA conversions at high temperatures were motivated by the formation of more thermodynamically stable M–N$_4$ structures (M = Pd, Pt, Au, *etc.*) as mobile M atoms were trapped in the defects of the carbon support. Furthermore, Yang *et al.*[182] prepared thermally stable Ni single atoms transformed from Ni metal nanoparticles supported on N-doped carbon with abundant defects. A mechanistic study showed that when exposed to N-doped carbon, Ni nanoparticles can break surface C–C bonds and drill into the carbon skeleton and that Ni atoms can be separated from Ni NPs due to the strong coordination and stabilization in the carbon substrate.

Recently, Qu *et al.*[180] reported a simple gas migration strategy to directly convert bulk metals into single atomic catalysts (Fig. 4) which resulted in outstanding ORR performance. In their preparation process, copper foam and ZIF-8 were separately placed into two porcelain boats before treatment in which ZIF-8 was first pyrolyzed under an argon atmosphere at 1173 K to form N-doped carbon supports (N–C) with empty zinc nodes and numerous defect sites. Following this, copper foam was exposed to an ammonia atmosphere to form volatile Cu(NH$_3$)$_x$ species through strong Lewis acid–base interactions between ammonia molecules and surface copper atoms and were hauled out of the copper foam. Subsequently, these Cu(NH$_3$)$_x$ species were captured by the defects in the N-rich carbon support to produce isolated Cu-SAs/N–C catalysts with the actual loading of Cu calculated to be 0.54% using inductively coupled plasma atomic emission spectroscopy (ICP-AES). Furthermore, the researchers also found that isolated copper single atoms can be homogeneously dispersed onto graphene sheets (Cu-SAs/N–G) by using graphene oxide as the defect-rich support in which ICP-AES analysis showed that the Cu

loading of Cu-SAs/N–G can reach 1.26 wt%. Moreover, the researchers claimed that this gas-migration method can be used to access a series of M-SAs/N–C (M = Co or Ni) catalysts, indicating its generality in the preparation of various functional ADMCs.[180] Electrochemical testing was also conducted in this study and suggested that Cu-SAs/N–C takes a near-4e$^-$ ORR pathway with a large kinetic current density (j_k) at 0.9 V and a low Tafel slope of 63 mV dec^{-1}, further demonstrating its outstanding ORR performance. And more importantly, no clear current density degeneration at $E_{1/2}$ was observed after 5000 continuous potential cycles, demonstrating the robust stability of this Cu-SAs/N–C catalyst.

In general, the atomization conversion from bulk metal materials such as nanoparticles, nanocrystals and metal foam is a convenient top-down means to prepare single-atom catalysts and provides a novel universal method for the development of precious metal single atomic catalysts with high thermal stability. This method may even be applicable for the reactivation and reuse of sintered industrial metal nanocatalysts (especially noble nanocrystals), providing valuable insights into the large-scale preparation of high-performance thermally stable electrocatalysts.[180]

2.5 Other potential synthesis methods

2.5.1 Photochemical method. The photochemical reduction method involving photon absorption and electronically excited states has been widely applied to synthesize metal nanocrystals. For example, Liu *et al.*[105] successfully fabricated a stable atomically dispersed palladium catalyst stabilized on ultrathin titanium oxide nanosheets (Pd$_1$/TiO$_2$) through a one-step photochemical route at room-temperature. In this study, two-atom-thick ultrathin TiO$_2$ nanosheets were first prepared by reacting TiCl$_4$ with ethylene
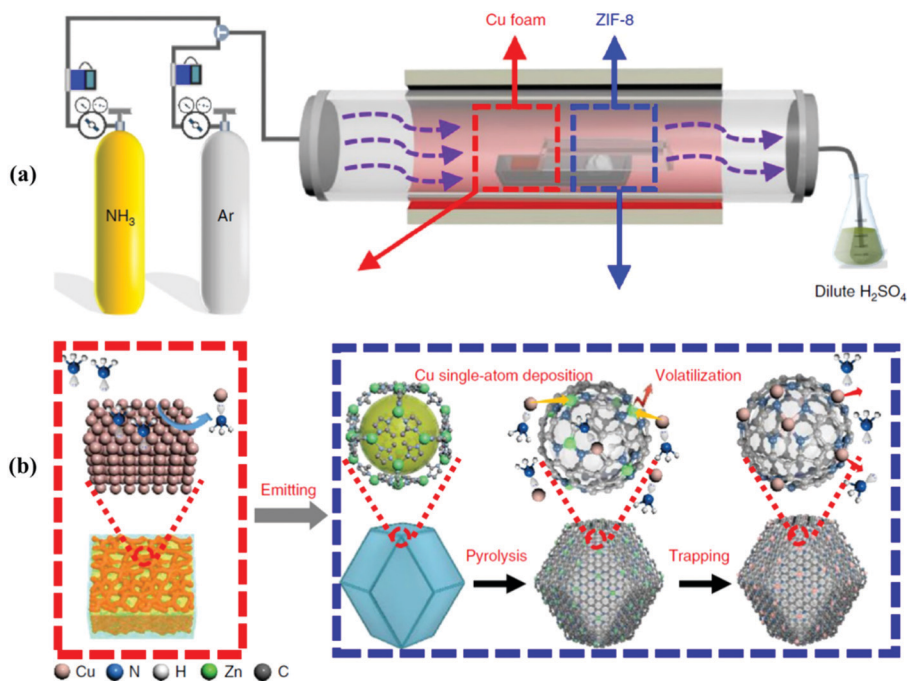

Fig. 4 (a) Schematic of the preparation of copper single atoms supported on nitrogen-doped carbon (Cu-SAs/N–C) and (b) its proposed reaction mechanism. Reproduced with permission,[180] Copyright 2018, Nature publishing group (NPG).

glycolate (EG) followed by a solvothermal process at 150 °C for 4 hours. Subsequently, the mixture of TiO$_2$ and H$_2$PdCl$_4$ was subjected to ultraviolet (UV) light at 365 nm to obtain Pd$_1$/TiO$_2$ in one step. The researchers reported that the UV-induced formation of EG radicals on the TiO$_2$ nanosheets was quite stable and was also critical in the preparation of Pd$_1$/TiO$_2$ due to the promotion of Cl$^-$ removal. In addition, the researchers also reported that after UV irradiation, Pd loading can be increased up to 1.5% and that the obtained Pd$_1$/TiO$_2$ demonstrated superior catalytic performances with no activity decay after 20 cycles. Similarly, Wei et al.[216] employed UV irradiation on frozen chloroplatinic acid (H$_2$PtCl$_6$) aqueous solutions to successfully synthesize atomically dispersed Pt catalysts on various substrates, including graphene, carbon nanotubes, mesoporous carbon, zinc oxide nanowires and titanium dioxide nanoparticles. The researchers in this study suggested that the photochemical reduction reaction occurring in the frozen precursor solution can balance the nucleation and growth of nanocatalysts, in which because ice lattices can naturally confine dispersed reagents and restrict photochemical reduction products, nucleation can be prevented. As a result, the aggregation of atoms can be effectively prevented and single atoms can be further successfully stabilized, demonstrating that this photochemical reduction strategy can be extended to the synthesis of other metal (Au, Ag, etc.) single atom catalysts.

2.5.2 High-energy ball milling method. High-energy ball milling has been verified to be a powerful bottom-up method due to its high efficiency at breaking and reconstructing chemical bonds of materials and is recognized as a potential pathway for synthesizing ADMCs.[135,185] For example, Cui et al.[152] and Deng et al.[185] both used high-energy ball milling to prepare and study a series of coordinatively unsaturated single iron catalysts confined in different matrixes such as silica and graphene. In these studies, lattice-confined single iron sites embedded in a silica matrix were obtained through the ball milling of a mixture of commercial SiO$_2$ and Fe$_2$SiO$_4$ under argon and fusing in air, and DFT calculations revealed that the most stable structure of the single iron atom was the one in which the single iron atom was bonded to one Si and two C atoms within the silica matrix.[184] Furthermore, a series of different metal single catalysts (Fe, Co, Mn, Ni, and Cu) embedded in graphene matrixes were also synthesized in large quantities using ball milling[152,185] in which embedded Fe loading in graphene could reach 4.0 wt%.[185] In addition, these confined and unsaturated single Fe sites demonstrated high catalytic performances in the direct non-oxidative conversion of methane[184] and in the catalytic oxidation of benzene.[185] Moreover, the researchers reported that the prepared CoN$_4$/GN possessed superior electrochemical properties for the interconversion of the redox couple I$^-$/I$_3^-$, which was attributed to the good balance between the adsorption and desorption processes originating from the appropriate adsorption energy of iodine on confined Co sites.[152] In another study, Zhang et al.[217] successfully synthesized uniformly distributed isolated metal catalysts supported on ordered mesoporous carbon using a solid-state ball milling method and reported that the coordination polymerization between metal ions and polyphenols was completed

during the solvent-free ball milling process. Meanwhile, the metal-salt linkers became stable metal nanoparticles in situ within the pores of the ordered mesoporous carbons (OMCs). And as a result, the formed catalysts supported on activated carbon and post-impregnated OMC were composed of either micropores or mesopores blocked by large metal nanoparticles, demonstrating that this ball milling method can largely reduce assembly times in solid-state routes as compared with the solution route and lead to large-scale fabrication of isolated metal atomic catalysts.

2.5.3 Mass-selected soft-landing method. The mass-selected soft-landing method is a powerful technique for the synthesis of metal clusters and is a potential technique for the synthesis of atomic catalysts. Furthermore, this technique is particularly effective in the preparation of small nanoclusters 0.5–2 nm (<200 atoms) in size. And as a physical deposition method, it can be applied to obtain any metal clusters consisting of precisely controlled numbers of atoms that "soft-land" onto the surface of flat supports[131] in which the number of atoms can be accurately controlled by using high-energy atom beams through vacuum surface procedures.[218–221] In addition, this precise control over cluster size is strongly dependent on the rapid evolution of atomic and electronic structures and generally, both gas-phase ion sources (cations/anions) and a mass-select spectrometer are required for downstream deposition onto substrates.[222] And as a result, this mass-selected soft-landing technique has great potential to prepare ADMCs. However, practical applications of this method are limited due to high costs, low-yields and difficulty in finding suitable precursors that are stable in solutions and can be electro-sprayed.[137] Furthermore, this mass-selected soft-landing method is also not suitable for high surface-area supports or mesoporous support materials, and hence is not favorable for practical industrial applications.[131]

2.5.4 Electrodeposition. As reported by Zhou et al.,[223] the electrochemical control of catalyst particle size can be achieved through electrodeposition methods in which the use of bismuth ultramicroelectrodes (UME) can allow for the electrodeposition of isolated Pt atoms or small clusters of up to 9 atoms. In this study, the researchers used femtomolar concentrations of PtCl$_6^{2-}$ ions to control the mass transfer of precursors to Bi-UME substrate surfaces and limit the number of Pt atoms coated on the electrode. A bismuth UME was immersed in a PtCl$_6^{2-}$ solution with a desired molar concentration and an electrochemical plating pulse of suitable duration was applied. The researchers reported that the pulse duration can determine the number of platinum atoms electrodeposited on the UME through the reduction of PtCl$_6^{2-}$ to Pt^0. And in order to obtain Pt clusters, UME could be further moved into a solution with a higher proton concentration. Lastly, the researchers reported that the deposited single Pt atoms or clusters were detected through the electrocatalytic voltammetry of HER.

2.5.5 Microwave-assisted rapid synthesis. Microwave heating is an effective method to synthesize nanomaterials because it can greatly reduce reaction times and suppress side reactions, dramatically improving efficiency. For example, Fei et al.[224] developed a convenient and rapid microwave-assisted synthesis method for G-SAMs involving the 2 second heating of a mixture of metal
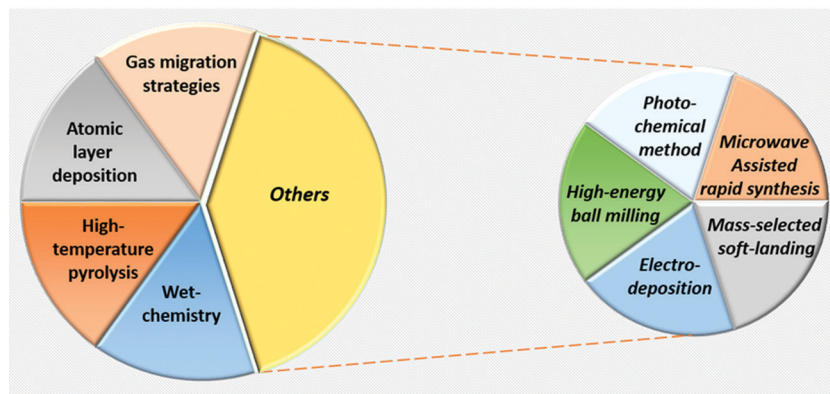
Scheme 4 The integrated figure of advanced synthesis methods for ADMCs.

salts and amine-functionalized graphene oxide using a microwave. This method also possesses universality for the exploration of N-doped graphene supported monodispersed atomic transition metals (*e.g.*, Co, Ni, and Cu).

In summary, to fully express the synthesis methods, Scheme 4 summarizes the entire synthesis methods discussed in the whole Section 2. In general, ADMC synthesis can be achieved through several synthesis methods. Here, the adsorption method with subsequent calcination can achieve atomic metal enriched surfaces, which might decrease catalytic mass transfer obstacles.[139] In addition, single Pt atom catalysts with relatively high loading (5 wt%) can be obtained through combining several synthesis methods. For example, zeolite-templated carbon (ZTC) supports can be first obtained through chemical vapor deposition (CVD) and atomically dispersed Pt can be selectively synthesized by a simple wet-impregnation method on the ZTC support.[111] Furthermore, well-dispersed Fe atoms supported on 3D simple-cubic carbon frameworks (Fe–N-SCCFs) with high stability can be derived from Fe_3O_4 nanocubes through a template method. In this case, Fe_3O_4 nanocubes can be first self-assembled into Fe_3O_4 superlattices, followed by *in situ* ligand carbonization, acid etching and NH_3 activation. Next, surface-coating oleic acid ligands on the surface of the Fe_3O_4 superlattices can be carbonized without affecting the ordering of the nanocubes through a high-temperature pyrolysis process, and finally, the target sample can be obtained through acid washing to remove the Fe_3O_4 nanocube template.[125] Overall, through the combination of synthesis methods, a variety of preparation procedures can be used to develop different types of ADMCs.

3. Characterization of atomically dispersed metal catalysts

3.1 Structural characterization

The development of atomic resolution characterization techniques for atomic level resolution studies of catalyst materials has led to the comprehensive understanding of the structural and fundamental mechanisms of ADMCs in catalysis processes. And recently, rapid developments in advanced characterization

technologies have allowed for the confirmation of ADMC systems. Along with advanced theoretical modeling and simulation techniques in computational chemistry,[225] ADMC structures and catalytic properties can be thoroughly investigated and predicted at the molecular level.[74,133,226,227] The technologies used for characterizing ADMCs mainly include *in situ/ex situ* X-ray diffraction (XRD), energy dispersive X-ray spectroscopy (EDX), X-ray photoelectron spectroscopy (XPS), *in situ/ex situ* scanning tunneling microscopy (STM and ETEM), aberration-corrected scanning transmission electron microscopy (ac-STEM) (accompanied by electron energy loss spectroscopy (EELS) and high-angle annular dark field (HAADF)) and X-ray absorption spectroscopy (XAS) (includes X-ray absorption near edge structure (XANES) and complementary extended X-ray absorption fine structure (EXAFS) spectroscopy). In addition, useful characterization techniques such as *in situ/ex situ* Fourier transform infrared spectroscopy (FTIR), *in situ/ex situ* Raman spectroscopy and nuclear magnetic resonance (NMR) can provide complementary data on the local structural information of ADMCs, which is in favor of understanding the mutual interactions between isolated metals and supports.[215] And although many existing techniques can be used to characterize materials structures, morphologies and composition, the tiny amounts and extremely small atomic size of ADMCs on substrates require instrument resolution capabilities to be extremely high and at atomic levels to provide useful information on structure, morphology and composition as well as electron interactions between atoms and between atoms and substrates. Therefore, the following subsection will only review several highly sensitive techniques.

3.1.1 Aberration-corrected scanning transmission electron microscopy (ac-STEM). Scanning transmission electron microscopy (STEM) is a straightforward morphology characterization technique to characterize material structures on the micro- and nanoscale. However, the resolution of STEM is limited by parasitic lens aberration. And therefore, major advancements in STEM involving the use of correctors for parasitic lens aberrations have been made to further increase resolutions to Å levels. The correctors used can produce electron beams with spot sizes of well below 1 Å and can adequately characterize atomic scale catalysts,[228,229] with the resulting STEM technique

2904 | *Energy Environ. Sci.*, 2019, **12**, 2890–2923

This journal is © The Royal Society of Chemistry 2019

referred to as aberration-corrected scanning transmission electron microscopy (ac-STEM). And as a result, this technique has become a standard tool in the characterization of atomic-scale catalysts and can provide precise and direct observations of the location of individual single metal atoms on supporting materials.[101,230] And in addition to spatial distribution, ac-STEM can also be used to evaluate crystallographic relationship in regard to the surface structure of supports. Furthermore, a combination of ac-STEM and HAADF can result in a technique called ac-HAADF-STEM which is useful for the characterization and understanding of the structure/morphology and fundamental mechanisms of single-atom catalysts as well as for further optimization of catalyst synthesis procedures. For example, Qu et al.[180] used TEM with corresponding EELS along with ac-HAADF-STEM on Cu single atoms decorated on N-doped porous carbon (Cu-SAs/CN) to obtain elemental mapping images of Cu-SAs/N–C, which revealed uniformly distributed Cu, C, and N elements over the entire architecture (Fig. 5a and b). In addition, the researchers reported that the number of bright spots tagged by red circles in the obtained ac-HAADF-STEM images represented single Cu atoms in which the contrast of the Cu single atoms depended on the location and stability (under electron beam irradiation) of the Cu atoms (Fig. 5c). Furthermore, the researchers reported that the coordination environment can be confirmed using ac-HADDF-STEM coupled with electron energy loss spectroscopy (EELS).

In another study by Wang et al.[160] a number of evenly scattered bright spots ascribed to Co atom sites were clearly observed in the carbon particles carbonized from ZIF nanocrystals based on the obtained ac-HADDF-STEM image (Fig. 5d), and was further confirmed in the obtained EELS point spectra (Fig. 5e and f). Here, the researchers reported that during ac-HADDF-STEM, if the electron beam was placed on the dark neighboring carbon support (green circle in Fig. 5d), no N or Co signals were observed in the accompanying EELS spectrum (Fig. 5e) whereas if the electron beam was moved over the bright dots (red circle), both Co and N were observed, suggesting coexistence in the form of CoN_x (Fig. 5f) and verifying that Co atoms in their 20Co-NC-1100 catalyst were coordinated with N from ZIF precursors.

Other powerful techniques such as scanning tunneling microscopy (STM) and in situ environmental transmission electron microscopy (ETEM) can also be used to identify the exact structure of ADMCs. And as a technique with true atomic resolution, STM is an ideal tool to study ADMCs for which Parkinson[231] has discussed the prospect of STM experiments under realistic reaction conditions. Furthermore, ETEM can be used to directly observe the dynamic transformation process of noble metal nanoparticles into thermally stable single atoms,[181] which might be beneficial to the in situ observation of the growing process of atomically dispersed metal catalysts for the ORR.
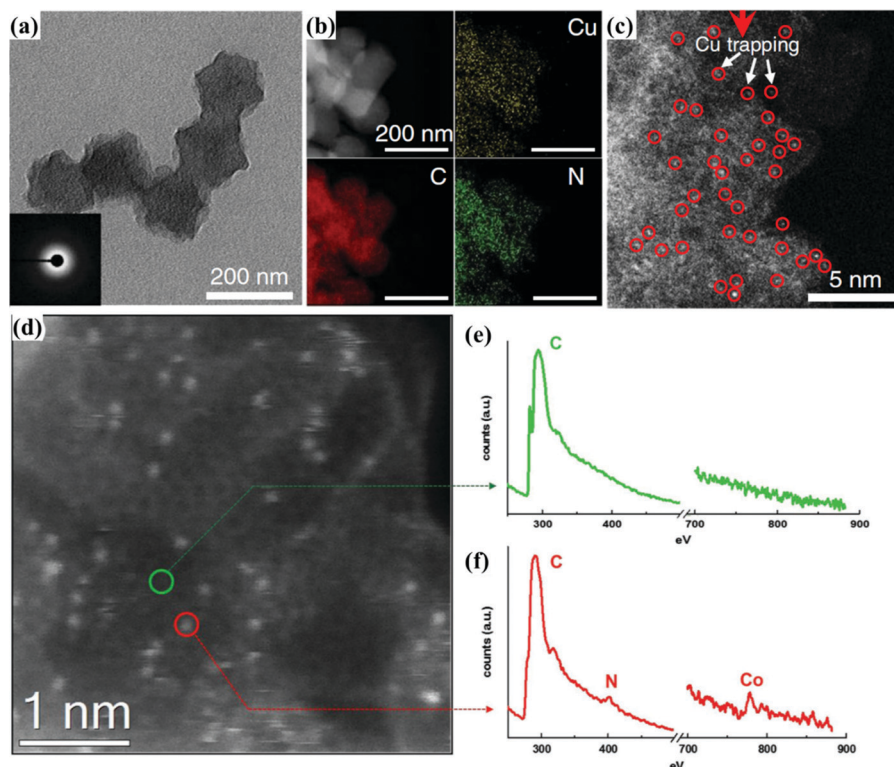
Fig. 5   (a) TEM image of ammonia-pyrolyzed ZIF-8 with the inset showing the ring-like selected-area electron diffraction (SAED) pattern. (b) Corresponding EELS mapping images of copper, carbon and nitrogen. (c) ac-HADDF-STEM image of Cu-SAs/N–C. Reproduced with permission[180] Copyright 2018, Nature publishing group (NPG). (d) ac-HADDF-STEM image with (e and f) accompanying EEL point spectra of the 20Co-NC-1100 catalyst. The point spectra in (e) and (f) were taken at the dark neighboring support and bright atoms in (d) respectively. Compared with point spectrum (e), point spectrum (f) showed both Co and N, indicating that Co is coordinated with N at an atomic scale. Reproduced with permission[160] Copyright 2018, Wiley-VCH.

This journal is © The Royal Society of Chemistry 2019

Energy Environ. Sci., 2019, 12, 2890–2923 | 2905

3.1.2 X-ray absorption near edge structure (XANES) spectroscopy. Synchrotron radiation-based X-ray absorption spectroscopy (XAS) is a powerful tool to characterize the geometric structure of the active moiety of ADMCs[65,232,233] and can be roughly divided into X-ray absorption near edge structure (XANES) spectroscopy and the complementary extended X-ray absorption fine structure (EXAFS) spectroscopy. XANES is highly sensitive to the oxidation states and coordination chemistries (e.g., tetrahedral or octahedral coordination) of metal species.[61,131,133,215,234] As reported, the white-line intensity in the normalized XANES reflects the oxidation state of determined metal elements.[235] For example, Liu et al. obtained XANES spectra of Pt_1/BP and $Pt_1–N/BP$ catalysts to study their near-edge absorption energy between those of Pt foil and bulk PtO_2 reference (Fig. 6a). The research revealed that the white-line intensities of Pt_1/BP and $Pt_1–N/BP$ were both between those of Pt foil and bulk PtO_2 reference, representing the oxidation of some Pt atoms in Pt_1/BP and $Pt_1–N/BP$. However, the L_3-edge of $Pt_1–N/BP$ showed a lower white-line intensity than that of Pt_1/BP, demonstrating the lower content of Pt oxide in $Pt_1–N/BP$ than that in Pt_1/BP.[235] As reported in another research, as annealing temperatures increased from 600 to 800 °C and subsequently to 1100 °C, the corresponding XANES edge can shift to lower energies, suggesting the reduction of Co oxidation states (Fig. 6b) in which the derivative of XANES showed that the characteristic peaks of the catalyst shifted from $Co^{(3+\delta)+}(\delta > 0)$ (600 °C) to predominantly Co^{2+} (1100 °C) (Fig. 6c). In addition, XANES revealed that the pre-edge peak (≈ 7710 eV) of Co-NC-1100 °C assigned to the forbidden 1s-to-3d transition was much lower than those of the precursor and catalysts from Co-NC-600 °C to Co-NC-800 °C, suggesting higher cation symmetry.[160]

3.1.3 Extended X-ray absorption fine structure (EXAFS) spectroscopy. Extended X-ray absorption fine structure (EXAFS) spectroscopy can be used to evaluate the fabrication of ADMCs and the local coordination environments of central metal atoms (e.g., coordination numbers, distances and adjacent atomic species).[133,234] In general, EXAFS raw data are background-subtracted and normalized, followed by Fourier transformation

and wavelet transformation.[98] Fourier transform (FT) is a fundamental step in the data reduction and clarification of EXAFS through the separation of backscattering atoms using their radial distance from absorbed atoms (namely shells) and wavelet transform (WT) is a routine complement to FT to provide radial distance resolution in k-space.[236,237] Furthermore, the ability to determine metal–metal coordination numbers has resulted in the effective use of EXAFS to evaluate the successful fabrication of ADMCs.[131,238] For example, Yang et al.[140] used FT-EXAFS to characterize single Pt atoms supported on titanium nitride (Pt/TiN, 0.35 wt%) and reported that the obtained FT-EXAFS curves showed only one strong peak at 2 Å and smaller wiggles at 2–3 Å. The only strong peak at 2 Å mainly originated from the Pt–Cl interaction and the smaller wiggles were because of the small Pt–Ti and Pt–Pt interactions (Fig. 7a). In another example, the researchers carried out WT-EXAFS to more clearly indicate the atomic dispersion of metal throughout the whole catalyst, which was owing to the powerful resolutions in both k and R space WT-EXAFS. In detail, the WT contour plot of Fe ISAs/CN displayed only one intensity maximum at 5 Å^{-1}, which could be attributed to the Fe–N (or Fe–O) coordination. However, the WT contour plots of Fe bulk (Fe foil) and Fe_2O_3 standards displayed the intensity maxima at 8 and 5 Å^{-1}, respectively, which were associated with the Fe–Fe and Fe–N(O) contributions (Fig. 7b). Impressively, compared to Fe foil and Fe_2O_3 standards, no WT signals assigned to Fe–Fe coordination were detected in the WT-EXAFS, suggesting only the presence of single Fe atoms anchored onto the carbon supports.[149] Moreover, WT-EXAFS is in particular useful for the identification of dual-metal atomic catalysts. For example, Xiao et al.[55] used WT-EXAFS to study a Co_2N_5 dimer metal site system and reported that the WT-EXAFS of the as-synthesized Co–N–C-10 sample (B in Fig. 7d) showed the coexistence of a Co–N path in the bottom contour map (A in Fig. 7d) and a Co–Co path in the top contour map (C in Fig. 7d) from Co nanoparticles. In addition, the WT-EXAFS obtained in this study revealed that k_B (6.88 Å^{-1}) was smaller than k_C (7.09 Å^{-1}), demonstrating the formation of a shortened Co–Co
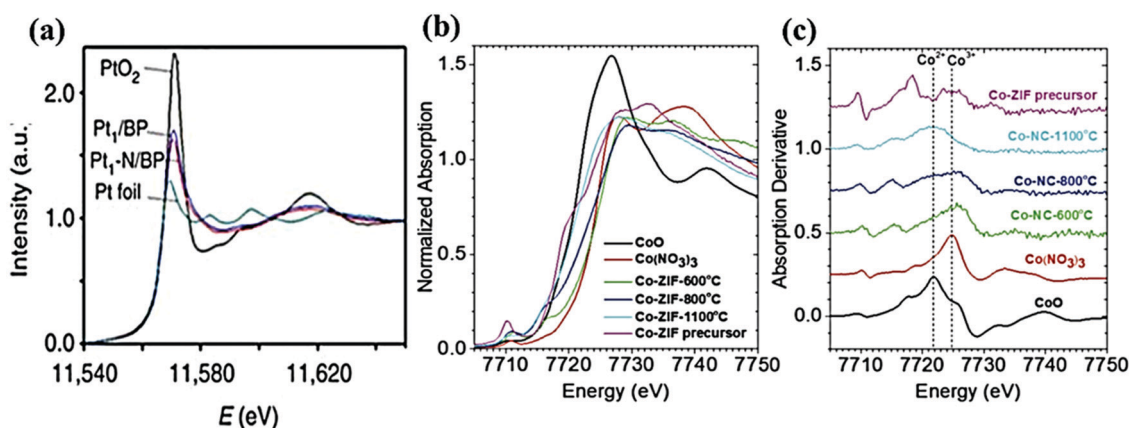
Fig. 6 (a) Pt L_3-edge XANES for Pt_1/BP, $Pt_1–N/BP$, Pt foil and bulk Pt oxide. Reproduced with permission,[235] Copyright 2017, Nature Publishing Group (NPG). (b and c) XANES spectra of Co–N–C catalysts annealed at different temperatures with (b) Co K-edge XANES and (c) the responding derivative of XANES. Reproduced with permission,[160] Copyright 2018, Wiley-VCH.

2906 | *Energy Environ. Sci.*, 2019, **12**, 2890–2923

This journal is © The Royal Society of Chemistry 2019
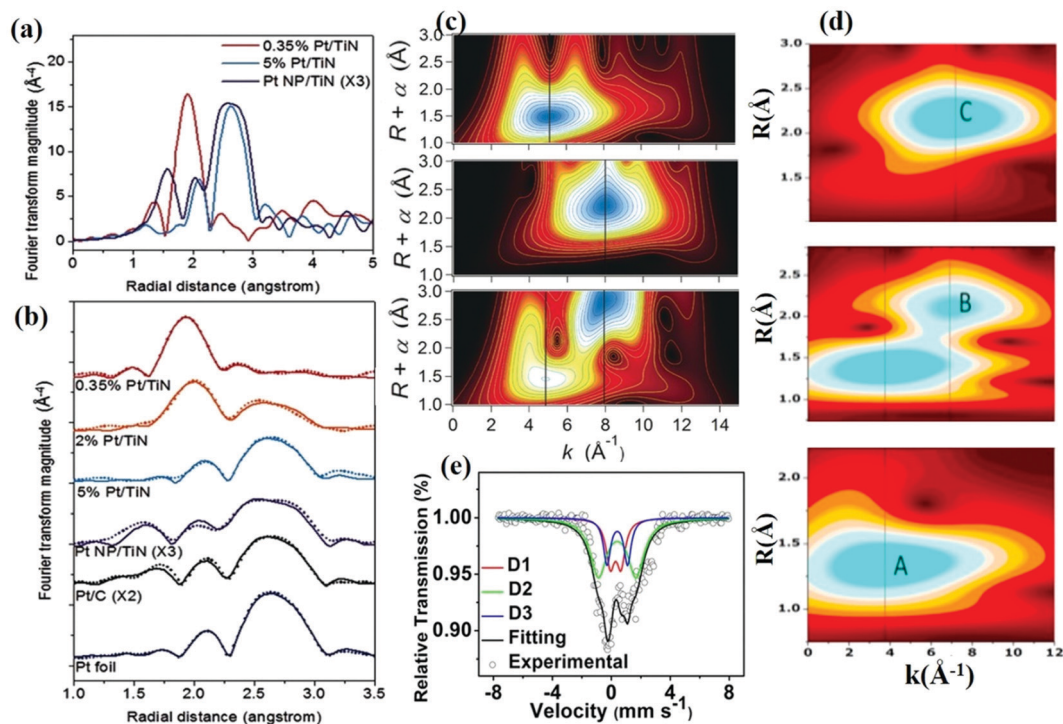
Fig. 7 (a) Pt L$_3$ edge k^3-weighted FT-EXAFS curves of the samples: 0.35 wt% and 5 wt% Pt/TiN, and 5 wt% Pt NP/TiN (tripled). (b) The corresponding FT-EXAFS fitting curves of 0.35 wt%, 2 wt% and 5 wt% Pt/TiN, 5 wt% Pt NP/TiN (tripled), 20 wt% JM Pt/C (doubled) and Pt foil with the fitting range from 1.0 to 3.5 Å; 20 wt% JM Pt/C Pt foil. Dots show the experimental data, and the lines are the fitted results. Reproduced with permission.[140] Copyright 2016, Wiley-VCH. (c) WT-EXAFS of Fe ISAs/CN (top), Fe foil (middle) and Fe$_2$O$_3$ standards (bottom). Reproduced with permission.[149] Copyright 2017, Wiley-VCH. (d) WT-EXAFS of a Co$_2$N$_5$ dimer metal site system with k^2-weighted $\chi(k)$ Co K-edge signals. Reproduced with permission.[55] Copyright 2018, Elsevier Ltd. (e) Mössbauer spectroscopy of ^{57}Fe in SA-Fe/NG. Reproduced with permission,[175] Copyright 2018, National Academy of Sciences.

distance in the as-synthesized Co–N–C-10 sample. Therefore, through the FT- and WT-EXAFS analysis, the dispersed states of metal atomic catalysts can be determined.

3.1.4 Fourier-transform infrared spectroscopy (FTIR). Fourier-transform infrared spectroscopy (FTIR) is an important technique for the characterization of the nature of supporting materials that adsorb probing molecules in which through the direct monitoring of the changes in the probe molecules based on vibrational frequency and intensity, the properties of the local structure, homogeneity and active centers can be deduced.[131,239] For example, FTIR has been applied to identify the presence of isolated single metals (Rh, Pt, *etc.*) on support materials[240,241] in which CO, NH$_3$, pyridine, *etc.* are often used as probing molecules. In addition, the percentage of isolated single metal atoms in supports can also be quantified using FTIR and time- and temperature-resolved FTIR spectroscopy can be applied to detect intermediate species during catalytic reaction processes.[131]

3.1.5 Nuclear magnetic resonance (NMR) spectroscopy. Nuclear magnetic resonance (NMR) spectroscopy is another tool that can be used to detect the existence of single atom catalysts and can provide information on the nature of metal species and the coordination between isolated active centers and supports. For example, under *in situ* conditions, NMR can be used to detect binding ligands during catalytic reactions and is useful for the understanding of the catalytic performance and formation mechanisms of ADMCs.[131,215,242]

3.1.6 Mössbauer spectrum. Mössbauer spectrum is a sensitive and powerful technique to characterize ORR catalysts, especially for iron-containing compounds, such as Fe–N$_4$ centers.[243–245] Recently, combined with EXAFS and HAADF-STEM measurements, Mössbauer spectrum has been used to gain insight into the Fe coordination type of ADMCs.[172,246–248] In general, Mössbauer spectrum of FeN$_4$-sites can be fitted with three doublets which can result in a ferrous low-spin and two ferrous mid-spin sites.[246] For example, Yang *et al.*[175] analyzed the coordination environment (Fe–N or Fe–O) of SA-Fe/NG by performing Mössbauer spectroscopy based on the recoil-free absorption of γ-rays by ^{57}Fe nuclei at 295 K. Being consistent with the EXAFS and HAADF-STEM observation, the Mössbauer curve did not show any sextets and singlet, indicating the absence of iron carbide phases and zero-valence iron crystals in SA-Fe/NG. As shown in Fig. 7e, Mössbauer curves of SA-Fe/NG are mainly fitted with three doublets (D1, D2, and D3) which are all assigned to Fe–N$_x$ moieties. Here, D1 is assigned to ferrous low-spin Fe–N sites, while D3 and D2 are assigned to ferrous mid-spin sites. The main difference between D2 and D3 probably originates from their local environment. Among them, the D2 proportion is the largest, signifying that the most possible coordination types of Fe–N species in SA-Fe/NG are the analog of the iron phthalocyanine structure. Furthermore, the Mössbauer spectrum can also be used to help understand the coordination environment of a Fe-base dual site catalyst, such as (Fe,Co)/N–C *etc.* In their

This journal is © The Royal Society of Chemistry 2019

Energy Environ. Sci., 2019, **12**, 2890–2923 | **2907**

research, (Fe,Co)/N–C also shows a three-doublet Mössbauer spectrum (D1, D2, and D3), and consists of square-planar Fe(II)N$_4$ coordination and is similar to the as-synthesized single metal catalyst (Fe SAs/N–C).[83,248]

4. ADMCs for the oxygen reduction reaction (ORR) in electrochemical energy devices

ADMCs can display high electrocatalytic ORR performance in both acidic and basic media; for instance, FeCo-ISAs/CN, as an ADMC, can provide a half-wave potential of 0.920 V (vs. RHE) in 0.1 M KOH.[139] However, the ORR activity of ADMCs in acidic electrolytes needs to be further improved, particularly in membrane electrode assemblies (MEA) for PEMFCs. The electrocatalytic performance of ADMCs towards the ORR is statistically shown in Table 2, including the half-wave potential ($E_{1/2}$), proposed active sites and mass active areas. As for the application of ADMCs in electrochemical energy devices such as fuel cells and metal–air batteries, ADMC-based catalyst layers can provide superior ORR performance in half-cell apparatus, but need to be further developed in real cells or batteries. But overall, ADMCs for the ORR have shown promising performances in PEMFCs,[144,175,249] regenerative fuel cells[83,144] and metal–air batteries.[117,250]

4.1 ADMC-catalyzed fuel cells

From Table 2, we can see that the maximum metal loading of ADMCs can achieve up to 9.33 wt% (2.6 at%).[146] Generally, ADMCs show better ORR catalytic activity in alkali than in acid. For example, the half-wave potential ($E_{1/2}$) of Fe50-N–C-900 and FeCo-ISAs/CN can reach 0.92 V[31,139] in 0.1 M KOH, and Pt-based ADMCs (A-PtCo-NC) can give an $E_{1/2}$ of 0.96 V vs. RHE. However, under acidic conditions, a relatively positive $E_{1/2}$ of 0.863 V can be obtained with a current density of 2.842 mA cm^{-2} at 0.9 V.[83] To date, ADMCs have been widely investigated in fuel cell applications, as shown in Table 3. For fuel cell applications, ADMCs can be used to construct cathodic catalyst layers in membrane electrode assemblies (MEA) to test PEM fuel cells under real operational conditions[144,175,190,249] such as at a constant cell voltage of 0.5 V with H$_2$ and O$_2$ feeds. Here, conditions such as the effects of catalyst/catalyst layer/MEA structures (particularly ORR active centers and support materials) and electrolytes should also be considered during the electrocatalytic process.[62] Generally, H$_2$/O$_2$ fuel cells can give better performance than hydrogen–air fuel cells. Currently, the maximum current density is reported to be 1100 mA cm^{-2} at 0.6 V,[253] while the max power density can reach ~0.87 W cm^{-2} (P_{O_2} = 1.0 bar) and even 0.94 W cm^{-2} (P_{O_2} = 2.0 bar).[161] In one example, Wang et al.[83] used a (Fe,Co)/N–C hollow carbon-derived catalyst with N-coordinated Fe, Co-dual metal sites as a cathode electrocatalyst and reported higher ORR performance with an onset potential (E_{onset}) of 1.06 V$_{RHE}$ and half-wave potential ($E_{1/2}$) of 0.863 V$_{RHE}$ as compared with commercial Pt/C catalysts (1.03 and 0.858 V respectively). In addition, the researchers verified full cell ORR activities in which (Fe,Co)/N–C dual atoms were used as a

catalyst in single fuel cell tests and delivered activities that outperformed most reported Pt-free catalysts under both H$_2$/O$_2$ and H$_2$/air conditions. The maximum power density of the (Fe,Co)/N–C catalyzed single H$_2$/O$_2$ fuel cell reached ~0.85 and 0.98 W cm^{-2} at 0.1 and 0.2 MPa partial pressures respectively. Furthermore, the researchers reported that this ADMC with dual metal sites demonstrated excellent durability in long-term operations with 50 000 cycles in an electrode cyclic voltammetry test and 100 hours for H$_2$/air single cell operations. This study also reported that by using pure O$_2$ as the oxidant for a H$_2$/O$_2$ single cell with ~0.77 mg cm^{-2} (Fe,Co)/N–C at the cathode and 0.1 mg$_{Pt}$ cm^{-2} Pt/C at the anode, O$_2$ mass transport issues can be alleviated and that a cell voltage of 0.6 V at a current density higher than 550 mA cm^{-2} and a peak power density higher than 505 mW cm^{-2} at 0.42 V can be achieved. However, despite these performances being better than most reported Pt-free catalysts, they are only ~76% of the power density of commercial Pt/C catalyst-based fuel cells.

In another example, Zeng et al.[144] tested atomically dispersed Pt$_1$@Fe–N–C catalysts in a real acidic PEM fuel cell and reported that with a cathode catalyst loading of 3 mg cm^{-2}, the Pt$_1$@Fe–N–C provided a high current density of 280 mA cm^{-2} at 0.8 V, which was higher than those of Fe–N–C (211 mA cm^{-2}) and 20% Pt/C (193 mA cm^{-2}), and that the power density curves of the MEAs showed that the Pt$_1$@Fe–N–C was 0.86 and 0.79 W cm^{-2} at 0.49 and 0.6 V respectively. More importantly, stability tests revealed that compared with Fe–N–C-based single cells, the Pt$_1$@Fe–N–C single cell at a constant voltage of 0.5 V for 50 hours with H$_2$ and O$_2$ feeds demonstrated remarkably alleviated performance decay in which the Pt$_1$@Fe–N–C normalized current remained at ~50% after 20 hour testing whereas Fe–N–C remained at 22%. In addition, the current density of the Pt$_1$@Fe–N–C (2.1 wt%) remained at almost twice that of Fe–N–C in the initial test stage.

4.2 ADMC-catalyzed metal–air batteries

ADMCs as cathode catalysts in Zn–air batteries have shown promising performances, demonstrating potential in practical applications.[117,118,250] Table 4 summarizes the performance of ADMC-catalyzed metal–air batteries, including the open circuit voltage, current density, power density, specific capacity and energy density, etc. For example, the current density and the max power density of Fe–N-SCCF-based zinc–air batteries can reach ~205 mA cm^{-2} (at 1.0 V) and 300 mW cm^{-2}, respectively. Wang et al.[117] reported that Fe–Co dual site ADMC embedded in carbon nanotube ((Fe,Co)/CNT)-based batteries exhibited a superior open-circuit voltage (1.63 V) as compared with commercial Pt/C-based batteries (1.56 V), validating the excellent ORR performance of (Fe,Co)/CNT (Fig. 8A). Here, an ADMC of (Fe,Co)/CNT dispersed on carbon paper (CP) with a loading of 1 mg$_{total}$ cm^{-2} was used as the air cathode in a Zn–air battery with 6 M KOH as the electrolyte and Zn foil as the anode and produced a high voltage of 1.31 V at a discharge current density of 20 mA cm^{-2}, with the power density and specific energy density of the full battery reaching 260 mW cm^{-2} and 870 W h kg$_{Zn}^{-1}$, respectively. Furthermore, discharge polarization

2908 | Energy Environ. Sci., 2019, 12, 2890–2923

This journal is © The Royal Society of Chemistry 2019

Table 2 Summary of the ORR catalytic properties of various ADMCs

Materials	Active center	Properties ($E_{1/2}$ (vs. RHE) or active area)	Loading	Ref.
Pt/TiN	Isolated single atomic Pt sites	78 A g_{Pt}^{-1} at an overpotential of 0.05 V, 0.1 M HClO$_4$	0.35 wt%	140
Pt$_1$/TiC; Pt$_1$/TiN	Atomically dispersed active sites High selectivity toward H$_2$O$_2$	0.96 mA cm^{-2} (0.2 V), 0.1 M HClO$_4$; 0.34 mA cm^{-2} (0.2 V), 0.1 M HClO$_4$	0.2 wt%; 0.2 wt%	141
Pt$_1$@Fe–N–C	Pt$_1$–O$_2$–Fe$_1$–N$_4$	0.80 V, 280 mA cm^{-2} at 0.8 V, 0.5 M H$_2$SO$_4$	2.1 wt% Pt	144
Pt$_1$–N/BP	g-P–N1–Pt1	0.87 V, 0.1 M KOH; 0.76 V, 0.1 M HClO$_4$	0.4 wt%	235
S,N–Fe/N/C-CNT	Fe–N$_x$ species	0.85 V, 0.1 M KOH	—	23
Fe50-N–C-900	Fe–N–C active sites	0.92 V, 0.1 M KOH; 6.83 mA cm^{-2}, 1 M HClO$_4$	0.1 mg cm^{-2} 0.3 mg cm^{-2}	31
Fe-ISA/NC	FeN$_4$S$_2$	0.896 V, 100.7 mA cm^{-2} at 0.85 V 0.1 M KOH	0.947 wt%	148
Fe-ISAs/CN	Fe–N$_4$	0.900 V, 37.83 mV cm^{-2} at 0.85 V, 0.1 M KOH	2.16 wt%	149
(CM + PANI)–Fe–C	FeN$_4$	0.80 V, 0.39 W cm^{-2} at 1.0 bar partial pressure of H$_2$ and air, 0.5 M H$_2$SO$_4$	0.2 at%	161
FeSAs/PTF-600	Fe–N$_4$	0.87 V, 5.51 mA cm^{-2} (0.2 V vs. RHE), 0.1 M KOH; 5.42 mA cm^{-2} (0.2 V vs. RHE), 0.1 M HClO$_4$	8.3 wt%	166
Fe SAs–N/C-20	FeN4-6r-c1, FeN4-6r-c2	0.915 V, 0.1 M KOH	0.20 wt%	157
FeNC-MSUFC	Fe–N$_4$	~0.73 V	0.044–0.048 at%	251
Fe$_{SA}$–N–C	Fe–N$_4$	0.891 V, 23.27 mA cm^{-2} (0.85 V), 0.1 M KOH; 0.776 V, 9.60 mA cm^{-2} (0.75 V), 0.1 M HClO$_4$	1.76 wt%	156
SA-Fe/NHPC	ORR	0.87 V, 4.1 mA cm^{-2} at 0.88 V, 0.1 M KOH	2.3 wt%	168
Fe-N-CNTAs-5-900	Fe–N$_x$	0.88 V, 0.1 M KOH	0.09 at%	174
FeN$_x$-Embedded PNC	ORR/OER Fe–N$_x$	0.86 V, 0.1 M KOH	3.935 at%	252
Fe-N-SCCFs	Fe-Containing active sites	0.883 V, alkaline	0.8 at%	125
Fe-NCCs	Fe–N$_x$	0.82 V, 0.1 M KOH	0.26 at%	173
SA-Fe/NG	Fe–N$_4$ moieties	0.88 V, 52.4 mA cm^{-2}, 0.1 M KOH; 0.8 V, 15.6 mA cm^{-2} (0.75 V), 0.1 M HClO$_4$	2.0 mg cm^{-2}	175
C-FeZIF-1.44-950	Fe–N$_x$	0.864 V, 0.1 M KOH; 0.78 V, 0.1 M HClO$_4$		253
C-FeHZ8@g-C$_3$N$_4$-950		0.845 V, 0.1 M KOH; 0.78 V 0.1 M HClO$_4$	3.17 wt%	247
A-Co/r-GO	CoN$_3$C	0.842 V, 0.1 M KOH; 0.71 V, 0.5 M H$_2$SO$_4$	3.6 wt%	143
CoSAs@CNTs	M–N–C and single Co atom sites	0.86 V, 0.1 M KOH	0.14 at%	164
CoN$_4$/NG	Co–N$_4$	0.87 V (0.1 M KOH), 23.4 mA cm^{-2} at 0.85 V	11.4 mF cm^{-2}	176
NGM-Co	Co–N$_x$–C	≈50 mV more positive than NGM, 0.1 M KOH	0.18 at%	170
Co-SAs@NC	ORR	0.82 V, 0.1 M KOH	1.70 wt%	159
Co-ISAS/p-CN nanospheres	ORR	0.837 V, 5.2 mA cm^{-2} (0.83 V), 0.1 M KOH	0.42 wt%	169
Co-SAs/N–C-900	Co–N$_2$	0.881 V, 0.1 M KOH; 0.863 V$_{RHE}$	4 wt%	99
Co-SAs/N–C-800	Co–N$_4$			
NC-Co SA	Co–N$_x$	0.72 V	1.84 wt%	150
CoNC700	Co–N$_4$ square-planar structures	0.85 ± 0.01 V, 0.1 M KOH; 0.73 V, 0.1 M HClO$_4$	0.73 at%	163
20Co-NC-1100	Co–N$_4$	ORR 0.80 V, 0.5 M H$_2$SO$_4$	0.34 at%	160
Zn/CoN–C	ZnCoN$_6$	0.861 V, 0.1 M KOH; 0.796 V, 0.1 M HClO$_4$	Zn 0.33 wt%; Co 0.14 wt%	118
ZnN$_x$/BP	Zn–N$_4$	−175 mV vs. SCE, 0.1 M KOH	0.3 wt%	165
Zn–N–C	Zn–N$_4$	0.746 V, 0.1 M HClO$_4$; 0.873 V, 0.1 M KOH	9.33 wt% (2.06 atom%)	146
Co$_2$N$_x$C	Co$_2$N$_5$	0.79 V, 0.1 M HClO$_4$, 3734 mA mg$_{Co}^{-1}$, 7468 mA mg$_{Co_2}^{-1}$	—	55
(Fe,Co)/N–C	Fe–Co dual-sites	0.863 V, 2.842 mA cm^{-2} at 0.9 V, 0.1 M HClO$_4$	—	83
FeCo-ISAs/CN	Fe–N$_4$ and Co–N$_4$	0.920 V, 31.1 mA cm^{-2} at 0.88 V, 0.1 M KOH	Fe 0.964 wt%, Co 0.218 wt%	139
A-PtCo-NC	(Co–Pt)@N8 V4	0.96 V, mass activity of 45.47 A mg^{-1}, 0.1 M KOH	Co: 1.72 wt%; Pt: 0.16 wt%	254
Fe, Mn–N/C-900	Fe–N$_x$ and Mn–N$_x$	0.905 V, 33.33 mA cm^{-2} (0.85 V), 0.1 M KOH	Fe: 1.75 wt%; Mn: 0.07 wt%	250
(Zn,Co)/NSC	Zn,Co–N$_6$–C–S	0.893 V, 0.1 M KOH; 0.70 V, 0.5 M H$_2$SO$_4$	—	119
Nb-in-C complex	Niobium atoms incorporated in graphite layers	12.3 mA cm^{-2} (−0.5 V$_{Ag/AgCl}$), 0.1 M KOH	60 μg cm^{-2}	177
Cu-SAs/N–C Cu-SAs/N–G	Cu–N$_4$	0.895 V, 0.005 mA cm^{-2} (0.9 V), 0.1 M KOH; 0.74 V, 0.1 M KOH	0.54 wt%; 1.26 wt%	180

SCE: saturated calomel electrode; RHE: reversible hydrogen electrode.

curves revealed that this battery can perform at a high current density of 178 mA cm^{-2} at a cell voltage of 1.0 V (Fig. 8B) with both the power density and current density significantly better than that of commercial Pt/C (105 mW cm^{-2} and 18 mA cm^{-2} respectively) (Fig. 8C). Galvanostatic discharge measurements were also conducted and revealed that the performance of the (Fe,Co)/CNT-based battery was better than that of commercial Pt/C-based batteries, as the specific capacity of the (Fe,Co)/CNT–Zn battery reached 774 mA h g$_{Zn}^{-1}$ at 50 mA cm^{-2}, corresponding to a gravimetric energy density of 870 W h kg$_{Zn}^{-1}$ (Fig. 8D). And because these values are higher than those of commercial Pt/C-based batteries (748 mA h g$_{Zn}^{-1}$ vs. 640 W h kg$_{Zn}^{-1}$ at 50 mA cm^{-2}), (Fe,Co)/CNT is a highly promising substitute for commercial Pt/C with great application potential in Zn–air batteries.

Table 3 Summary of ADMC-catalyzed fuel cells

Materials	Open circuit	Current density	Power density	Ref.
(Fe,Co)/N–C	H_2/O_2 fuel cell	>550 mA cm^{-2}, 0.6 V and a peak power density >505 mW cm^{-2} at 0.42 V	Max power density: ∼0.85 W cm^{-2} at 0.1 MPa; 0.98 W cm^{-2} at 0.2 MPa	83
Pt$_1$@Fe–N–C	H_2/O_2 fuel cells	280 mA cm^{-2} at 0.8 V	Peak power density: 0.86 W cm^{-2} at 0.49 V; high power density: 0.79 W cm^{-2} at 0.6 V	144
(CM + PANI)–Fe–C	H_2–air fuel cell	—	0.39 W cm^{-2}	161
(CM + PANI)–Fe–C	H_2/O_2 fuel cell	—	∼0.87 W cm^{-2} (p_{O_2} = 1.0 bar) 0.94 W cm^{-2} (p_{O_2} = 2.0 bar)	161
SA-Fe/NG	PEMFC	0.85 A cm^{-2} at 0.6 V; 3.34 A cm^{-2} at 0.2 V	823 mW cm^{-2}	175
20Co-NC-1100	H_2/O_2 fuel cell	—	0.56 W cm^{-2}	160
Pt$_1$–N/BP	H_2/O_2 fuel cells	Surface area of 1102 m^2 g^{-1}	0.68 W cm^{-2} with 0.13 g$_{Pt}$ kW^{-1}	235
C-FeZIF-1.44-950	H_2/O_2 PEMFC	1100 mA cm^{-2} at 0.6 V; 637 mA cm^{-2} at 0.7 V	775 mW cm^{-2}	253
	H_2–air PEMFC	650 mA cm^{-2} at 0.6 V; 350 mA cm^{-2} at 0.7 V	463 mW cm^{-2}	
C-FeHZ8@g-C$_3$N$_4$-950	H_2/O_2 PEMFC	400 mA cm^{-2} at 0.7 V; 133 mA cm^{-2} at 0.8 V	628 mW cm^{-2}	247

Table 4 Summary of ADMC-catalyzed metal–air batteries

Materials	Application	Open circuit voltage (V)	Current density	Power density	Ref.
S,N–Fe/N/C-CNT	Zinc–air batteries	1.35	—	102.7 mW cm^{-2}	23
FeN$_x$-Embedded PNC	Zinc–air batteries	1.55	—	278 mW cm^{-2}	252
Fe–N-SCCFs	Zinc–air batteries		∼205 mA cm^{-2} (1.0 V)	300 mW cm^{-2}	125
Fe–NCCs	Zinc–air batteries	1.36	Specific capacity: 705 mA h g^{-1} at 5 mA cm^{-2}	Peak power density: 66 mW cm^{-2} at 0.55 V	173
pCNT@Fe@GL	Zn–air batteries	—	—	—	255
				No significant change on overpotential (0.58 V, Fe–N–C pCNT + NiFe LDH) and discharge potential (≈1.36 V, pCNT@Fe@GL towards ORR)	
CoN$_4$/NG	Flexible solid zinc–air batteries	1.51	50.0 mA cm^{-2}	115 mW cm^{-2} Specific capacity: 730 mA h g^{-1} Energy density: 671 W h kg^{-1}	176
	All-solid-state foldable Zn–air battery	—	—	28 mW cm^{-2}	
NGM-Co	Zinc–air batteries	1.439	—	152 mW cm^{-2} 840 W h kg$_{Zn}$$^{-1}$ at 20.0 mA cm^{-2}	170
NC-Co SA	Zn–air battery	1.411	31.0 mA cm^{-2}	20.9 mW cm^{-3}	150
Zn–N–C	Zn–O$_2$ battery		683.3 mA h g$_{Zn}$$^{-1}$ (100 mA cm^{-2})	179 mW cm^{-2}	146
(Fe,Co)/CNT	Zn–air batteries	1.63	178 mA cm^{-2} (1.0 V)	260 mW cm^{-2} with specific energy density of 870 W h kg$_{Zn}$$^{-1}$	117
Zn/CoN–C	Zn–air battery	1.4	—	230 mW cm^{-2}	118
(Zn,Co)/NSC	Zinc–air batteries	1.5	—	Peak power density: 150 mW cm^{-2}	119
	Solid-state zinc–air battery	1.56	—	15 mW cm^{-2}	

5. Theoretical electrochemical ORR mechanisms catalyzed by ADMCs

The rational design of ADMCs with highly active sites and the elucidation of their nature remain challenging. In addition to physicochemical characterization methods, various theoretical modeling and simulations are effective in the understanding of ADMC structural effects and their catalytic ORR mechanisms. And with the rapid development of computer technologies, data processing speeds are becoming faster, resulting in the simulation of electrocatalytic performances using computational chemistry becoming increasingly precise and accurate. The development of electrochemical reaction models and simulation methods have made computational chemistry an indispensable means of electrocatalytic research and evaluation of catalyst electrocatalytic properties at the atomic level.[256]

First-principles density functional theory (DFT) calculations are an important tool to investigate the fundamental ORR mechanisms of supported ADMCs, including the geometric configurations and electronic structures of ADMCs as well as reaction dynamics such as active centers, strong metal–support interactions (SMSI) and charge transfer processes.[131,137,257,258] Compared with DFT calculations for metal nanoparticles and cluster catalysts, the DFT calculations for ADMCs are much faster because only one metal atom is involved.[259,260] However, it should be noticed that a lot of calculations are still needed for finding the right spin states. DFT calculations can provide quantitative structural information on coordination numbers, bond lengths, bond angles, bonding energies, charge density distributions, and Bader charges,[122,257] and are vital in the investigation of reaction intermediates catalyzed by metal atoms. Furthermore, the state of metal catalysts (metallic or insulating)
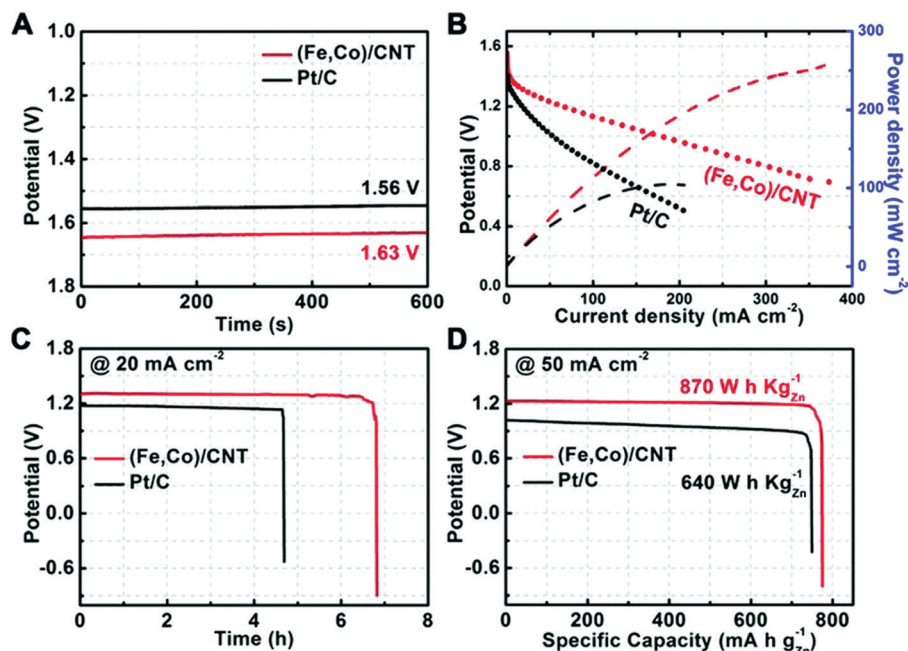
Fig. 8 (A) Open circuit voltage curves of (Fe,Co)/CNT-based and Pt/C-based Zn–air batteries using (Fe,Co)/CNT and Pt/C as cathode catalysts respectively. (B) Discharge polarization curves of Zn–air batteries with corresponding power densities. (C) Galvanostatic discharge curves of Zn–air batteries at 20 mA cm^{-2}. (D) Long-term galvanostatic discharge curves of Zn–air batteries before the complete consumption of the Zn anode at 50 mA cm^{-2}. Reproduced with permission.[117] Copyright 2018, Wiley-VCH.

can be obtained through the analysis of density of states (DOS) at the Fermi level, which is important in the determination of chemical reaction dynamics.[261,262] Aside from DFT calculations, *ab initio* molecular dynamics (MD) is also widely applied to characterize active site properties of electrocatalysts.[263] For example, Holby *et al.* used *ab initio* molecular dynamics to evaluate the stability of metal–nitrogen clusters through observations of the reconstruction of water molecules around the active sites. The simulated system was studied in the presence of solvent molecules (H_2O) at a thermal temperature of 300 K for a period of time and revealed that as O_2 molecules were introduced, constraints relaxed and spontaneous dissociation occurred in the presence of water in which this spontaneous reaction was likely to be unaffected by solvation, indicating that solvents appear to have no effect on the stability of edge defects.[263] Nevertheless, the effects of solvents on the adsorption energies of ORR intermediates are so appreciable that the solvation is also a key issue currently in computational electrocatalysis, because it can change adsorption energies and activity predictions.[264,265] Besides, the potential energy surface of ADMCs for ORR may be studied using *ab initio* molecular dynamics for geometry optimizations in solvent environments. Furthermore, DFT can also be used to approximate free energies of adsorption and provide a first-order estimation of ORR activities by means of the calculated overpotentials. Furthermore, the complementary stability modelling, such as Pourbaix diagrams (or potential-pH predominance diagrams) is also a useful tool to visualize electrochemical equilibrium conditions and analyze the free energy dependency of the electrochemical intermediates in changing potential and pH situations.[88,266] Based on all of this, Section 5 will review and
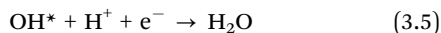
analyze the current state of theoretical research for single atom ORR catalysts from the aspects of active sites and catalyst–support interactions.

5.1 Catalytic ORR active centers of ADMCs

ADMCs with structural uniformity are ideal model systems to investigate structure and performance relationships[110] and the study of active site structures is beneficial to the design and optimization of catalyst structures to increase active site density, efficiency and durability for the ORR. Based on numerous theoretical studies, metal–ligand element moieties supported on carbon (M–L_x–C; M = Fe, Co, Zn, Pt, *etc.*, L = N, S, *etc.*) structures are promising candidates for electrocatalytic ORR in which atomic M–L_x–C structures with high electrical conductivity can display comparable ORR performances to commercial Pt/C catalysts, especially in alkaline environments. In addition, the presence of nitrogen in catalysts can also play an important role in developing M–N–C ADMCs with highly catalytic ORR activities. For example, carbon-hosted porphyrin-like FeN_4C_{12} (M = Fe, Co, Ni, *etc.*) moieties have been identified to be active for the ORR.[54,90,243,266,267] Based on DFT calculations, Calle-Vallejo *et al.*[88] pointed out that the transition metal atoms and 4 nitrogen atoms on graphitic materials are active towards the ORR and OER.[90] They also compared single-metal active sites of metal–N_4 sites in porphyrins and ADMCs in functionalized graphitic materials towards both ORR and OER.[266] It was found that the activity trend of the two materials was basically the same, and the active sites containing groups 7 to 9 transition metals (in the periodic table) might be good ORR and OER electrocatalysts. In both research studies, the authors also computationally determined

This journal is © The Royal Society of Chemistry 2019

Energy Environ. Sci., 2019, **12**, 2890–2923 | **2911**

the oxidation states of the active sites based on ligand-field theory and the spin states of the metal centers. The spin analysis results showed that the possible oxidation state of the transition metal atoms in these active sites had flexibility and was generally 2^+.[90,266]
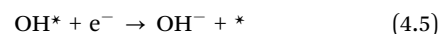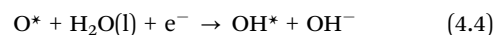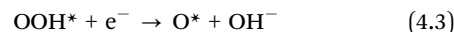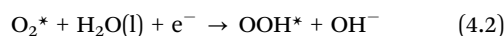
In ORR catalysis by ADMCs, three mechanisms have been proposed to describe the reduction of oxygen molecules to form water molecules, including oxygen dissociation, peroxyl dissociation and hydrogen peroxide dissociation in which peroxyl dissociation is one possible ORR mechanism with the smallest energy pathway (MEP) to describe the ORR.[55,268] The free energy of each elementary step can be calculated by uniting the enthalpy with the harmonic entropy. The reaction free energy (ΔG) within the purely thermodynamic model is given by Nørskov et al.[269] with the expression: $\Delta G = \Delta E + \Delta_{ZPE} - T\Delta S + \Delta E_{solvation}$, where ΔE is the reaction energy of an elementary chemical reaction and can be obtained from DFT calculations, Δ_{ZPE} is the difference in zero point energy, and ΔS is the change in entropy, and $\Delta E_{solvation}$ is related to solvation energy. Here, the zero-point energy comes from vibrational frequency analysis normally made using the harmonic oscillator approximation. In their work, they also introduced the concept of computational hydrogen electrode (CHE) which was the basis of most computational electrochemistry studies and allowed for the relatively accurate modelling of protons and electrons in solution.[270] In acidic media, the general ORR process could be described by five elementary steps, as follows:[209]

$$O_2(g) + * \rightarrow O_2* \tag{3.1}$$

$$O_2* + H^+ + e^- \rightarrow OOH* \tag{3.2}$$

$$OOH* + H^+ + e^- \rightarrow O* + H_2O \tag{3.3}$$

$$O* + H^+ + e^- \rightarrow OH* \tag{3.4}$$

$$OH* + H^+ + e^- \rightarrow H_2O \tag{3.5}$$

where * represents the adsorption site and the latter four steps (2 to 5) give the $4e^-$ transfer mechanism. For example, Liu et al.[235] reported that the pure carbon-supported Pt SAC (Pt1/BP) displayed a lower ORR performance (0.44 V_{RHE} of $E_{1/2}$) than N/BP (0.51 V_{RHE} of $E_{1/2}$), suggesting that single Pt atoms with oxidation state, supported on carbon materials, were almost inert to the ORR process.[140] However, by doping N, the catalytic activity of the modified Pt SAC (Pt1–N/BP) with a Pt loading of 0.4 wt% was significantly increased (0.76 V_{RHE} of $E_{1/2}$). This could provide a strategy for improving the catalytic activity of carbon-based atomically dispersed metal catalysts by utilizing the intrinsic catalytic activities of the complex active sites based on single metal atoms and doped heterogeneous elements. Notably, the authors also observed the above synergistic-effect-induced high ORR activity of Pt1–N/BP under alkaline conditions with a much higher $E_{1/2}$ of 0.87 V_{RHE} (Fig. 9b), which was at the same level as that of the traditional state-of-the-art Pt/C catalysts. The coordination number of the Pt atoms in Pt1–N/BP was revealed to be 5 with a distance of 2.0 Å. DFT calculations further revealed that the O–O bond of O_2 adsorbed on a single Pt atom of g-P–N1–Pt1 sites was longer than that on the traditional bulk Pt–NP-based active sites (Fig. 9c), which probably indicated the

easier breaking of the O–O bond. The formation of OOH* on the g-P–N1–Pt1 site further elongated the O–O bond length to 1.49 Å, suggesting an easier dissociation of the O–O bond in the succeeding steps. Besides, an important indicator of the catalytic properties of a catalyst was found to be ORR overpotential, which could be demonstrated in the calculated free energy diagrams.[88,89,271] The circle of Fig. 9c displayed the free energy diagrams on g-P–N1–Pt1 site. At $U = 0$ V, all the electron-transfer steps are exothermic and the free energy pathway is downhill. From this, it can be seen that the atomic structure model is an effective approach to verify catalytic active sites through the quantitative estimation of the free energy of elementary reaction steps by calculating the entropy, binding energy, solvation energy and zero-point energy of possible intermediates on catalysts in which the resulting energy diagrams can be used to identify the potential determining steps during catalytic ORR and the activity of different atomic sites.[257] In addition, the potential-limiting steps are more appropriate because they are thermodynamic steps, while the rate-limiting step is a kinetic one.[272]

For alkaline conditions, the catalytic cycle is described by steps (4.1)–(4.5) as follows:[149,269]

$$O_2(g) + * \rightarrow O_2* \tag{4.1}$$

$$O_2* + H_2O(l) + e^- \rightarrow OOH* + OH^- \tag{4.2}$$

$$OOH* + e^- \rightarrow O* + OH^- \tag{4.3}$$

$$O* + H_2O(l) + e^- \rightarrow OH* + OH^- \tag{4.4}$$

$$OH* + e^- \rightarrow OH^- + * \tag{4.5}$$

where steps (7)–(10) correspond to the $4e^-$ transfer processes. For example, Chen et al.[149] reported that at $U = 0$ V, the first three electron-transfer steps (steps (2), (3) and (4)) of Fe-ISAs/CN and Fe particles (Fe-NPs/CN) exhibited similar free-energy changes. Here, by comparing free energetics, the electron transfer in steps (2) and (5) of Fe-ISAs/CN was revealed to be endothermic, suggesting the need for external forces (i.e., applied voltage) at $U = 0$ V. In addition, the formation of OH* is energetically facile, suggesting that resident *OH adsorbed on the catalyst is difficult to remove.[55] Step (5) is the potential determining step with the highest endothermic energy in which an estimated overpotential of 0.65 V for Fe-ISAs/CN is required for step 5 to become exothermic. This is much lower than that of Fe-NPs/CN (1.76 V), making electron transfer in Fe-ISAs/CN much easier from Fe single atoms to adsorbed *OH species followed by charging of adsorbed *OH to form OH⁻, resulting in high ORR reactivity.

As for isolated Pt atom catalysts on sulfur-doped zeolite-templated carbon supports (Pt/HSC catalyst), Choi et al.[111] modeled Pt–S₄ catalytic centers and, through DFT calculations using the Perdew–Burke–Ernzerhof function and semi-empirical dispersion correction, obtained the best fitted ligation model with one Pt atom ligated by two thiophenes and two thiolates in which the Pt–S₄ species form a square-planar-type ligand arrangement with a typical d^8 electron configuration (Fig. 10a). The researchers reported that if solvated in water, Pt^{2+} centers can be activated by favorably interacting with two water molecules to

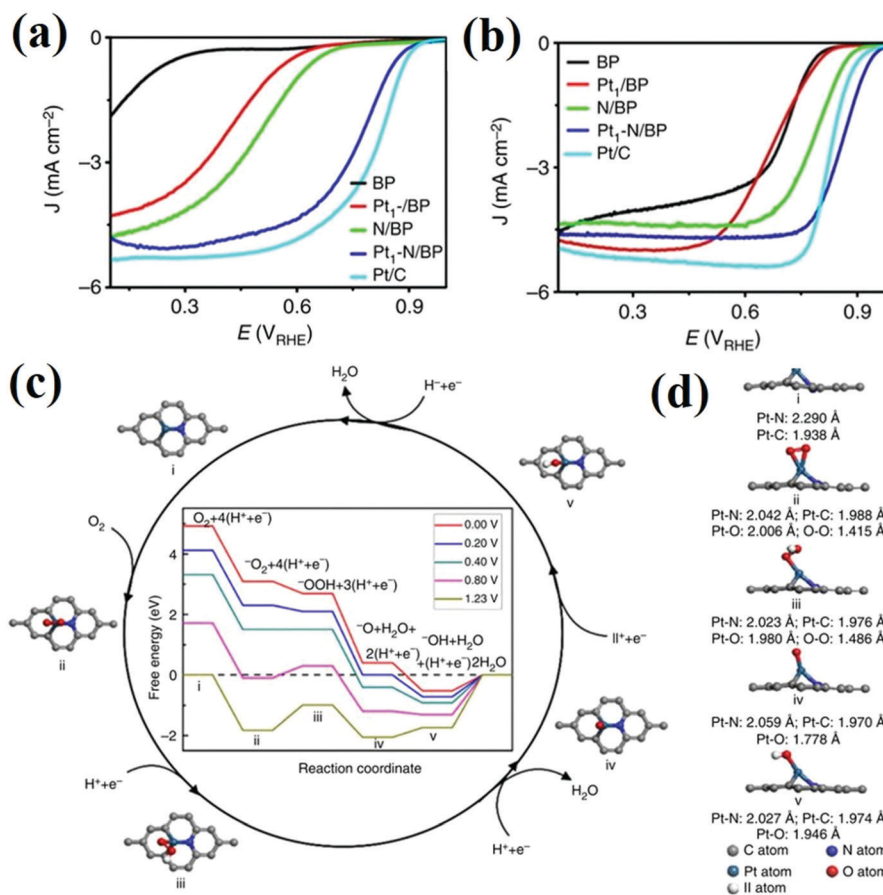2912 | Energy Environ. Sci., 2019, 12, 2890–2923

This journal is © The Royal Society of Chemistry 2019

Fig. 9 (a) RRDE polarization curves of different catalysts (BP, Pt_1/BP, N/BP, Pt_1–N/BP and commercial Pt/C) in O_2-saturated 0.1 M $HClO_4$ (a) and 0.1 M KOH (b) with a scan rate of 5 mV s^{-1} at a rotation speed of 1600 rpm. (c) The proposed reaction pathways and free energy diagram (the inset) for the ORR on the g-P–N_1–Pt_1 catalyst in acidic medium, (d) side view and bond lengths of the proposed catalytic sites. Reproduced with permission.[235]

substitute two S of the thiophene-like moiety (0.63 eV downhill; Fig. 10b) and the stronger Lewis basicity of the oxygen lone-pairs as compared with sulfur lone-pairs in thiophene results in a distorted Pt center positioned out of the original square planar geometry, allowing this ligand substitution to make Pt more suitable for catalytic actions. Furthermore, the researchers reported that by substituting a H_2O molecule, the Pt center can reduce oxygen molecules through a series of proton-coupled electron transfer (PCET) processes in which the first PCET is the potential-determining step in both the $2e^-$ and $4e^-$ pathways (Fig. 10c). Here, the calculated ORR limiting potential was reported to be 0.64 V_{RHE}, which matched well with the experimental onset potential of 0.71 V_{RHE}.

According to the different coordination configurations of active M–N_x centers, there are several possible active centers other than MN_4 sites such as MN_2 moieties.[74] Notably, recent theoretical and experimental results have indicated that abundant atomically dispersed MN_2 moieties show better ORR behaviors than MN_4 moieties and even better than commercial Pt/C catalysts.[99,172,244] The researchers attribute this performance to the weaker interactions between MN_2 moieties and $*O_2$ and $*OH$ intermediates in comparison with MN_4 moieties, which can promote the electron transport process.[172] In addition, researchers

have also reported that MN_2 moieties can exhibit stronger interactions with peroxide as compared with MN_4 according to DFT calculations[99] which is strongly associated with improved ORR performances. Furthermore, DFT calculations have also revealed that FeN_2 moieties are more active than CoN_2 moieties for the ORR due to the lower energy barriers of the intermediates and products involved.[54]

Dual atomic catalysts, which possess more atomic metal active sites, have been recently reported to exhibit higher intrinsic activities towards the ORR and theoretical and experimental studies have revealed that dual-atom catalysts can considerably reduce thermodynamic barriers.[55] For example, Holby et al.[263] investigated Fe atoms located between N-terminated zigzag edges and found that the FeN_3 cluster structure (which can form Fe_2N_5 sites) appeared to be capable of undergoing barrierless cleavage of O–O bonds through a dissociative ORR pathway thus avoiding the formation of H_2O_2. In addition, ab initio molecular dynamics in that study revealed that the solvation process does not appear to affect the spontaneous reaction and stability of these N-coordinated intra-edge defects in the carbon support.[263]

Pt-Free dual site ADMCs such as binuclear Co_2N_5 and Fe–Co dual sites have also been shown to possess outstanding ORR

This journal is © The Royal Society of Chemistry 2019

Energy Environ. Sci., 2019, **12**, 2890–2923 | **2913**
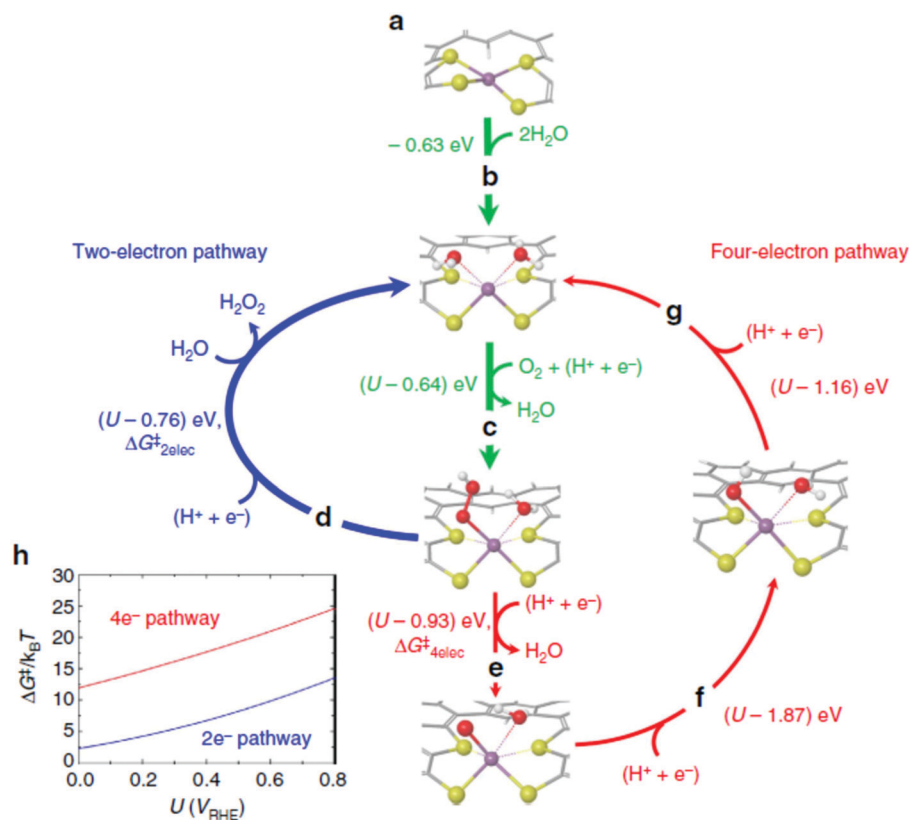
Fig. 10 Possible ORR mechanisms on the atomic Pt/HSC catalyst. (a) Atomically dispersed Pt complexed with two thiophene and two thiolate groups in one carbon framework. (b) Activation of Pt centers by substituting two S from the thiophene-like moiety with two O from water molecules. (c) The first proton-coupled electron transfer (PCET) process during the oxygen reduction process to form OOH. (d) $2e^-$ pathway: H_2O_2 formation through the second PCET followed by the substitution of an H_2O_2 molecule with an outer-sphere H_2O molecule, recuperating the initial state in which Pt is complexed with two thiolates and two water molecules. (e) $4e^-$ pathway: H_2O formation through the second PCET process involving the breaking of O–O bonds. (f) The formation of OH through the third PCET process and (g) an inner-sphere H_2O through the fourth PCET process (C: grey, H: white, S: yellow, O: red, Pt: purple). (h) Calculated kinetic barriers of the second PCET step for $2e^-$ (blue) and $4e^-$ (red) pathways using the Marcus kinetic theory. Ref. 111 Copyright 2016, NPG.

performance in acidic media[55,83] and such dual sites are reported to be able to activate and spontaneously cleave O–O bonds, which is crucial for the $4e^-$ transfer of the ORR.[83,273] For example, Xiao et al.[55] built several possible Co_2N_x configurations to identify potential active site structures, including Co_2N_5, CoN_4–CoN_3, CoN_2–CoN_2 and Co_2N_6 through DFT calculations. The results proved that the shortest Co–Co distance of 2.21 Å obtained from the binuclear site (Co_2N_5) structure was close to 2.12 Å attained in the EXAFS fitting process. In addition, the researchers reported that their novel binuclear Co_2N_5 sites demonstrated extreme activity towards the ORR that was 12 times higher than that of conventional CoN_4 sites. This might be attributed to the greatly reduced thermodynamic energy barrier originated from the binuclear site structure.

Another type of ADMC with dual sites consists of two different metal single atoms isolated on the support.[118,119,139] Here, the introduction of a second doping metal or ligand element complicates situations and there are controversies concerning the binding modes of the two metal elements in dual atomic catalysts; namely, the type of bonding, including M_1–M_1, M_2–M_2 or M_1–M_2 bonding and the presence of metal–metal bonding, especially in cases in which M–L bonding coordination is close. A typical example is FeCo-ISAs/CN with atomically dispersed Fe and Co

atoms. Zhang et al.[139] conducted FT-EXAFS and reported that the main peak at 1.5 Å in the FT-EXAFS for the Fe K-edge was assigned to the Fe–N coordination and the only main peak at 1.4 Å in the Co K-edge spectra was assigned to the Co–N coordination. Additionally, no other peaks, especially those of Fe–Fe bonds and Co–Co bonds at ~2.2 Å, were detected in the FT-EXAFS spectra, indicating the atomic dispersion of Fe and Co atoms. The researchers attributed the enhanced kinetics of the ORR active centers of FeCo-ISAs/CN not only to the increased metal sites, but also to the synergistic effects of the adjacent atomically dispersed Fe and Co active sites. In another example Lu et al.[118] investigated Zn/CoN–C with Zn and Co atoms forming Zn–Co dual atomic pairs with a distance of 0.22 ± 0.04 nm. Zn/CoN–C presented the best ORR performance with a $E_{1/2}$ of 0.861 V that was 35, 68 and 155 mV more positive than those of Pt/C (0.826 V), CoN–C (0.793 V) and ZnN–C (0.706 V) respectively. The researchers in this study also obtained the structural information of Zn/CoN–C and the ORR active sites using a combination of XAFS and DFT and reported that based on the fitting results of XAFS, the coordination number of both Co–N and Zn–N was 3.5 in the first shell, suggesting that the Co–N and Zn–N interactions were both in a mixed M–N_3 and M–N_4 (M = Co, Zn) environment. As for the second shell, the coordination

2914 | Energy Environ. Sci., 2019, 12, 2890–2923

This journal is © The Royal Society of Chemistry 2019

number of both Co–M and Zn–M was reported to be 0.5 ± 0.1, suggesting a weak Co–M and Zn–M interaction in the form of a $ZnCoN_6$ structure. Furthermore, DFT calculations revealed that the lowest energy could be obtained through Co bonding with Zn, suggesting the tendency to form Co–Zn diatomic pairs. Finally, *in situ* XANES spectra of Zn/CoN–C confirmed that Co acted as an active center during the ORR due to its more involved activity.

Although the dual-atom strategy can increase the catalyst loading of ADMCs, coordination situations become more complex because pure dual-atom ADMCs are difficult to prepare due to the coexistence of single and dual atoms simultaneously. And for the second introduced ligand (L′), the identification of active sites ($Fe–L_x$) requires the understanding of the coordination conditions of Fe, L and L′, which is more complex.[23] This structural information might be obtained through a combination of theoretical calculations and advanced characterization technologies, such as probe molecules, Mössbauer, nuclear resonance vibrational spectroscopy, etc.[274] For example, using a combination of DFT calculations with local scanning tunneling microscopy/spectroscopy (STM-STS) measurements, Kondo et al.[275] was able to obtain the density of states in the occupied region near the Fermi level of the carbon atoms adjacent to pyridinic N.

5.2 Strong metal–support interactions (SMSIs)

In general, the structure of ADMCs, their vicinal coordination environments and the close contact of catalyst atoms with supporting materials play a significant role in the enhancement of catalyst ORR activities.[276–279] For metal atoms, they carry charge (s), which can affect their binding strengths with reactant molecules or regulate their behavior.[277] And for supports of ADMCs, they not only act as anchoring sites to strongly interact with isolated atoms and further prevent migration and agglomeration, but also actively participate in surface reactions.[141] Based on this, numerous DFT calculations on different ADMC systems have focused on metal atom–support interactions and corresponding catalytic performances.[131] And to increase the aggregation barrier to prevent sintering, many factors including the support type and defects, particle size and morphology and metal–reactant interactions should be taken into consideration.[120,279] In general, the metal atom–support interactions originate from the chemical bonding effect and charge transfer between metal catalysts and supports and the associated interface.[101,280] Single metal atoms are chemically anchored onto the surface of supports through strong metal–support interactions (SMSIs), which usually involve interfacial bonding, including metal–metal bonds or coordination bonds with O, N and S atoms on supports.[281] SMSIs can ensure the tight anchoring of atomically dispersed metals onto support surfaces, preventing the migration and aggregation of single-atoms and maintaining their stability during the catalytic process.[131] Furthermore, SMSIs can lower the free energy and form highly stable and catalytically active centers for desired catalytic reactions.[120] Therefore, the selection of appropriate supports is necessary to strongly interact with isolated atoms and prevent the migration and agglomeration of isolated atoms, forming stable, finely dispersed active sites. And among promising catalysts, nanocarbon-based materials have attracted intense

attention due to their economic viability, tunable surface chemistry and fast electron transfer capacity. However, significant enhancements in the active sites of heteroatom-decorated carbon materials remain challenging.[23]

The rational design of ORR electrocatalysts and even bifunctional ORR and OER electrocatalysts with atomic modulation is greatly desired for fuel cells and rechargeable flexible metal–air batteries. Numerous studies have demonstrated that DFT is a powerful technique for understanding the nature of active centers, metal atom–support interactions and the evaluation of catalytic activity.[86] And based on the single metal atomic scale data obtained through ac-STEM imaging, theoretical calculations can be carried out to help understand the structure and ORR activity of single atom catalysts on support materials. For example, on the surface of selected supports, ac-STEM imaging data of ADMCs can be directly used to establish models for DFT calculations of catalytic processes,[103,228] allowing for the elucidation of stable conformations and providing new perspectives in the detection of structures and characteristics.[4,5,135,215] And ultimately, more robust ORR catalysts toward specific electrochemical processes can be precisely and rationally designed at the atomic level.

6. Summary, technical challenges and possible research directions

6.1 Summary

In this Review, the most recent developments of atomically dispersed metal catalysts (ADMCs) with single-atom and dual-atom active sites for the oxygen reduction reaction (ORR) have been summarized, including their synthesis/characterization, reaction mechanisms and application in electrochemical energy conversion and storage devices. Here, ADMCs with minimal size and maximum atomic utilization are of significance for the rational utilization of precious metal resources and the improvement of the economic feasibility of electrocatalytic systems. The realized ADMCs show excellent ORR performance and can be used as model systems for the fundamental understanding of ORR mechanisms in terms of active sites and interactions between ADMCs and supports. In ADMCs, the catalytic active sites can be verified through the quantitative estimation of the free energy of elementary reaction steps; however, to compare between different active sites, researchers usually assume that the reaction mechanism is identical on all sites, which is not necessarily true and may lead to erroneous conclusions.[282] For example, MN_2 moieties show higher ORR performance due to weaker interactions with $*O_2$ and $*OH$ intermediates than MN_4 species. As for dual atomic catalysts with increased number of active sites, these have recently been reported to show higher intrinsic activities towards the ORR due to the considerably low onset potential. The dual metal sites can activate and spontaneously cleave O–O bonds which is crucial for the $4e^-$ pathway, further promoting the electron transport process. In addition, strong metal–support interactions (SMSIs) allow ADMCs to be able to tightly anchor onto supports, improving the stability of single-atom catalysts. And overall, the understanding of the

This journal is © The Royal Society of Chemistry 2019

Energy Environ. Sci., 2019, **12**, 2890–2923 | **2915**

nature of ADMC structures can allow for the rational design of better electrocatalysts with precise active site structures and excellent ORR properties at the atomic level.

6.2 Technical challenges and their analysis

Although ADMCs possess many advantages over conventional catalysts, several challenges remain in terms of their development and practical application:

(1) **Insufficient catalytic ORR activity.** The improvement of ADMC catalytic performance towards the ORR is necessary yet challenging, especially under acidic conditions. In addition, an in-depth understanding of reaction mechanisms including active centers, strong metal–support interactions (SMSI) and charge transfer processes, especially in practical applications of fuel cells and metal–air batteries, is also challenging.

(2) **Insufficient catalytic ORR stability, particularly in PEM fuel cell and metal–air battery applications.** To achieve commercialization, the stability of ADMCs is critical. However, problems originating from agglomeration during material sintering and increased metal atom loading due to their high free energy as well as deactivation of isolated metal atoms during the catalytic reaction process of energy devices due to aggregation or leaching remain. Particularly in acidic media, due to the corrosiveness of the environment and sluggish kinetics, ADMCs face greater challenges. Here, because ADMCs are generally confined and stabilized on support materials, metal–support interactions play a key role in the homogeneous dispersion and enhanced stability of ADMCs. Therefore, the availability of homogeneous structures of anchor sites on supports becomes particularly important for the rational design of ADMCs with high stability.

(3) **Lack of fundamental understanding.** An understanding of the structure and electrochemical performance of ADMCs at the atomic level can be achieved by the development of advanced atomic resolution characterization and calculation techniques. However, deeper insights into the geometric configuration and electronic structure of ADMCs are still required, such as the local coordination environments of centrally active metal sites (*e.g.*, coordination numbers, distances and adjacent atomic species), especially for ADMCs with dual and even multiple sites, in which coordination conditions and active sites are more complex and difficult to identify.

(4) **Difficulty in the scale-up synthesis of ADMCs.** Simple and large-scale synthesis of ADMCs with perfectly balanced metal active center loading and dispersal is still challenging. Here, the difficulty in the accurate synthesis of atomic catalysts is caused by the lack of precise control over the atomic active site formation process. And presently, synthesis methods play a key role in the development and practical application of ADMCs; however, most of them are produced using bottom-up strategies with metal precursors adsorbed/anchored, reduced or confined by defects on oxides or carbon supports with ample N or O defects or vacancies, which are not suitable for large-scale production.

6.3 Possible research directions

To facilitate further development and overcome challenges, several research directions are proposed as follows:

(1) **Further development and optimization of synthesis strategies to obtain more active and stable ADMCs.** To achieve significantly enhanced catalytic ORR activities and stabilities in ADMCs, especially in practical applications, synthesis methods and optimizations are key and new material exploration and selection for catalysts and supports are crucial. One strategy to increase the catalytic activity is to dope carbon materials with heterogeneous elements (such as nitrogen, boron, sulfur, oxygen, phosphorus, *etc.*). Furthermore, the strengthening of the affinity and synergistic interactions between support surfaces and metal precursors, including interfacial chemical bonding and finely dispersed anchor sites, needs to be given larger emphasis and more effort.

(2) **Further investigations into structure–activity relationships and reaction catalytic mechanisms at the atomic level.** Theoretical calculations, advanced modern characterizations and experimental validations are all methods to achieve the fundamental understanding of catalyst performances and mechanisms for new catalyst design and performance optimization. Theoretical calculation is an important topic now to realistically include electrochemical barriers in computational models by using the computational hydrogen electrode (CHE) and it will be a major advance when it happens.[270] Besides, a better explanation of solvation is also a current requirement.[264,265] In addition, the activity model should be supplemented by the stability model (*e.g.*, Pourbaix diagram).[283] Finally, besides the associative pathways based on *OOH, *OH and *O proposed by Norskov *et al.*,[284] there are also several other pathways which should be considered when analyzing the activity trends. Through a combination of physicochemical characterization techniques (*e.g.*, ac-STEM, XAFS, FTIR, NMR) and theoretical calculations (*e.g.*, DFT), the structures and electrochemical reaction mechanisms of ADMCs can be investigated and understood, including binding energies, coordination environments and active centers. In this regard, the development of *in situ* characterization technologies such as *in situ* electron microscopy and *in situ* X-ray absorption fine structure is expected to aid the catalyst growth process and reaction mechanism research, especially in practical performance validation. Furthermore, the identification and detailed characterization of active site chemical structures towards the ORR are highly desirable and a deeper understanding of ADMC structures, including reactive active sites and interactions between metal atoms and support surfaces, will benefit the rational design and optimized synthesis of ADMCs at the atomic level. In addition, it is also highly desirable to achieve atomic modulation of ADMCs towards the ORR with accurately controlled coordination environments for metal atoms.

(3) **Development of large-scale rational design and synthesis strategies for ADMCs with elaborately controlled active sites and increased metal loading.** For rational design and optimized synthesis of ADMCs at the atomic level, several strategies can be elaborated. For the high-temperature pyrolysis strategies, ensuring the original ratio of metal and the strong affinity between support surfaces and metal complexes is the most basic requirement. Besides, high temperature pyrolysis is also affected by the heating rate and heating conditions, *etc.*, so it needs to be

2916 | *Energy Environ. Sci.*, 2019, **12**, 2890–2923

This journal is © The Royal Society of Chemistry 2019

precisely regulated to achieve micro-area pyrolysis. In addition, through the exploration of new/advanced materials and/or novel large-scale synthesis strategies, including atomic layer deposition, mass-selected soft-landing *etc.*, ADMCs can be rationally designed and fabricated with perfectly balanced metal loadings and dispersal states for practical application, in which ADMCs with dual- and even multi-site atomic catalysts can possess more metal loading and more active centers.

(4) Further design and optimization of ADMC catalyst layers and membrane electrode assemblies for fuel cells and metal–air batteries. The advanced structure and high ADMC loading of catalyst layers (CLs) as well as associated membrane electrode assemblies (MEAs) play a crucial role in device performance. Therefore, ADMC-based CLs and MEAs need to be innovatively designed and optimized to achieve high performances in fuel cells and metal–air batteries toward practical application.

Conflicts of interest

There are no conflicts of interest to declare.

Acknowledgements

References

1 S. Chu and A. Majumdar, *Nature*, 2012, **488**, 294.

2 M. Zhou, H.-L. Wang and S. Guo, *Chem. Soc. Rev.*, 2016, **45**, 1273–1307.

3 H. D. Yoo, E. Markevich, G. Salitra, D. Sharon and D. Aurbach, *Mater. Today*, 2014, **17**, 110–121.

4 H. Xu, D. Cheng, D. Cao and X. C. Zeng, *Nat. Catal.*, 2018, **1**, 339–348.

5 Y. Jiao, Y. Zheng, M. Jaroniec and S. Z. Qiao, *Chem. Soc. Rev.*, 2015, **44**, 2060–2086.

6 Y.-J. Wang, B. Fang, D. Zhang, A. Li, D. P. Wilkinson, A. Ignaszak, L. Zhang and J. Zhang, *Electrochem. Energy Rev.*, 2018, **1**, 1–34.

7 H. Zhang, H. Zhao, M. A. Khan, W. Zou, J. Xu, L. Zhang and J. Zhang, *J. Mater. Chem. A*, 2018, **6**, 20564–20620.

8 R. Wang, H. Wang, F. Luo and S. Liao, *Electrochem. Energy Rev.*, 2018, **1**, 324–387.

9 A. Yu, V. Chabot and J. Zhang, *Electrochemical Supercapacitors for Energy Storage and Delivery: Fundamentals and Applications*, CRC Press, Boca Raton, 2013.

10 C. Zhu, Q. Shi, S. Feng, D. Du and Y. Lin, *ACS Energy Lett.*, 2018, **3**, 1713–1721.

11 M. A. Khan, H. Zhao, W. Zou, Z. Chen, W. Cao, J. Fang, J. Xu, L. Zhang and J. Zhang, *Electrochem. Energy Rev.*, 2018, **1**, 483–530.

12 J. Qiao, Y. Liu, F. Hong and J. Zhang, *Chem. Soc. Rev.*, 2014, **43**, 631–675.

13 X. Wang, Z. Chen, X. Zhao, T. Yao, W. Chen, R. You, C. Zhao, G. Wu, J. Wang, W. Huang, J. Yang, X. Hong, S. Wei, Y. Wu and Y. Li, *Angew. Chem.*, 2018, **130**, 1962–1966.

14 H. B. Yang, S.-F. Hung, S. Liu, K. Yuan, S. Miao, L. Zhang, X. Huang, H.-Y. Wang, W. Cai, R. Chen, J. Gao, X. Yang, W. Chen, Y. Huang, H. M. Chen, C. M. Li, T. Zhang and B. Liu, *Nat. Energy*, 2018, **3**, 140–147.

15 W. Xing, G. Yin and J. Zhang, *Rotating Electrode Methods and Oxygen Reduction Electrocatalysts*, Elsevier Press, 2014.

16 K. Strickland, E. Miner, Q. Jia, U. Tylus, N. Ramaswamy, W. Liang, M.-T. Sougrati, F. Jaouen and S. Mukerjee, *Nat. Commun.*, 2015, **6**, 7343.

17 S. Wang and S. P. Jiang, *Natl. Sci. Rev.*, 2017, **4**, 163–166.

18 R. Borup, J. Meyers, B. Pivovar, Y. S. Kim, R. Mukundan, N. Garland, D. Myers, M. Wilson, F. Garzon, D. Wood, P. Zelenay, K. More, K. Stroh, T. Zawodzinski, J. Boncella, J. E. McGrath, M. Inaba, K. Miyatake, M. Hori, K. Ota, Z. Ogumi, S. Miyata, A. Nishikata, Z. Siroma, Y. Uchimoto, K. Yasuda, K.-I. Kimijima and N. Iwashita, *Chem. Rev.*, 2007, **107**, 3904–3951.

19 X. Fu, P. Zamani, J.-Y. Choi, F. M. Hassan, G. Jiang, D. C. Higgins, Y. Zhang, M. A. Hoque and Z. Chen, *Adv. Mater.*, 2017, **29**, 1604456.

20 M. Liu, R. Zhang and W. Chen, *Chem. Rev.*, 2014, **114**, 5117–5160.

21 M. A. Rahman, X. Wang and C. Wen, *J. Electrochem. Soc.*, 2013, **160**, A1759–A1771.

22 J. Park, M. Park, G. Nam, J.-S. Lee and J. Cho, *Adv. Mater.*, 2015, **27**, 1396–1401.

23 P. Chen, T. Zhou, L. Xing, K. Xu, Y. Tong, H. Xie, L. Zhang, W. Yan, W. Chu, C. Wu and Y. Xie, *Angew. Chem., Int. Ed.*, 2017, **56**, 610–614.

24 J.-S. Lee, S. Tai Kim, R. Cao, N.-S. Choi, M. Liu, K. T. Lee and J. Cho, *Adv. Energy Mater.*, 2011, **1**, 34–50.

25 C. Xia, J. Guo, Y. Lei, H. Liang, C. Zhao and H. N. Alshareef, *Adv. Mater.*, 2018, **30**, 1705580.

26 Z. Cui, G. Fu, Y. Li and J. B. Goodenough, *Angew. Chem.*, 2017, **129**, 10033–10037.

27 J. Zhang, L. Qu, G. Shi, J. Liu, J. Chen and L. Dai, *Angew. Chem., Int. Ed.*, 2016, **55**, 2230–2234.

28 H. Shui, T. Jin, J. Hu and H. Liu, *ChemElectroChem*, 2018, **5**, 1401–1406.

29 C. Hu and L. Dai, *Angew. Chem., Int. Ed.*, 2016, **55**, 11736–11758.

30 G. Zhang, B. Y. Xia, C. Xiao, L. Yu, X. Wang, Y. Xie and X. W. Lou, *Angew. Chem., Int. Ed.*, 2013, **52**, 8643–8647.

31 S. Fu, C. Zhu, D. Su, J. Song, S. Yao, S. Feng, M. H. Engelhard, D. Du and Y. Lin, *Small*, 2018, **14**, 1703118.

32 Y. Zhao, S. Huang, M. Xia, S. Rehman, S. Mu, Z. Kou, Z. Zhang, Z. Chen, F. Gao and Y. Hou, *Nano Energy*, 2016, **28**, 346–355.

33 J. Zhang, C. Zhang, Y. Zhao, I. S. Amiinu, H. Zhou, X. Liu, Y. Tang and S. Mu, *Appl. Catal., B*, 2017, **211**, 148–156.

34 M. K. Debe, *Nature*, 2012, **486**, 43–51.

35 H. Zhang and P. K. Shen, *Chem. Rev.*, 2012, **112**, 2780–2832.

This journal is © The Royal Society of Chemistry 2019

Energy Environ. Sci., 2019, **12**, 2890–2923 | **2917**

36 L. Tao, Y. Zhao, Y. Zhao, S. Huang, Y. Yang, Q. Tong and F. Gao, *J. Phys. Chem. Solids*, 2018, **113**, 61–66.

37 G. Wu and P. Zelenay, *Acc. Chem. Res.*, 2013, **46**, 1878–1889.

38 M. Lefèvre, E. Proietti, F. Jaouen and J.-P. Dodelet, *Science*, 2009, **324**, 71–74.

39 G. Wu, K. L. More, C. M. Johnston and P. Zelenay, *Science*, 2011, **332**, 443–447.

40 I. E. L. Stephens, A. S. Bondarenko, U. Grønbjerg, J. Rossmeisl and I. Chorkendorff, *Energy Environ. Sci.*, 2012, **5**, 6744–6762.

41 L. Bu, S. Guo, X. Zhang, X. Shen, D. Su, G. Lu, X. Zhu, J. Yao, J. Guo and X. Huang, *Nat. Commun.*, 2016, **7**, 11850.

42 L. Bu, N. Zhang, S. Guo, X. Zhang, J. Li, J. Yao, T. Wu, G. Lu, J.-Y. Ma, D. Su and X. Huang, *Science*, 2016, **354**, 1410–1414.

43 D. He, L. Zhang, D. He, G. Zhou, Y. Lin, Z. Deng, X. Hong, Y. Wu, C. Chen and Y. Li, *Nat. Commun.*, 2016, **7**, 12362.

44 L. Carrette, K. A. Friedrich and U. Stimming, *ChemPhysChem*, 2000, **1**, 162–193.

45 E. Yeager, *Electrochim. Acta*, 1984, **29**, 1527–1537.

46 Y. Lin, P. Liu, E. Velasco, G. Yao, Z. Tian, L. Zhang and L. Chen, *Adv. Mater.*, 2019, 1808193.

47 X. Han, X. Ling, Y. Wang, T. Ma, C. Zhong, W. Hu and Y. Deng, *Angew. Chem., Int. Ed.*, 2019, **58**, 5359–5364.

48 K. Kinoshita, *Electrochemical oxygen technology*, John Wiley & Sons, 1992.

49 H. S. Wroblowa, P. Yen Chi and G. Razumney, *J. Electroanal. Chem. Interfacial Electrochem.*, 1976, **69**, 195–201.

50 L. Zhang, H. Li and J. Zhang, *J. Power Sources*, 2014, **255**, 242–250.

51 N. M. Marković, T. J. Schmidt, V. Stamenković and P. N. Ross, *Fuel Cells*, 2001, **1**, 105–116.

52 N. M. Marković and P. N. Ross, *Surf. Sci. Rep.*, 2002, **45**, 117–229.

53 J. Yi, P. Liang, X. Liu, K. Wu, Y. Liu, Y. Wang, Y. Xia and J. Zhang, *Energy Environ. Sci.*, 2018, **11**, 3075–3095.

54 C. Zhu, Q. Shi, B. Z. Xu, S. Fu, G. Wan, C. Yang, S. Yao, J. Song, H. Zhou, D. Du, S. P. Beckman, D. Su and Y. Lin, *Adv. Energy Mater.*, 2018, **8**, 1801956.

55 M. Xiao, H. Zhang, Y. Chen, J. Zhu, L. Gao, Z. Jin, J. Ge, Z. Jiang, S. Chen, C. Liu and W. Xing, *Nano Energy*, 2018, **46**, 396–403.

56 M. Liu, Y. Lu and W. Chen, *Adv. Funct. Mater.*, 2013, **23**, 1289–1296.

57 T. J. Schmidt, H. A. Gasteiger, G. D. Stäb, P. M. Urban, D. M. Kolb and R. J. Behm, *J. Electrochem. Soc.*, 1998, **145**, 2354–2358.

58 U. A. Paulus, T. J. Schmidt, H. A. Gasteiger and R. J. Behm, *J. Electroanal. Chem.*, 2001, **495**, 134–145.

59 A. Rabis, P. Rodriguez and T. J. Schmidt, *ACS Catal.*, 2012, **2**, 864–890.

60 Z. Lu, J. Wang, S. Huang, Y. Hou, Y. Li, Y. Zhao, S. Mu, J. Zhang and Y. Zhao, *Nano Energy*, 2017, **42**, 334–340.

61 C. Zhu, S. Fu, Q. Shi, D. Du and Y. Lin, *Angew. Chem., Int. Ed.*, 2017, **56**, 13944–13960.

62 A. P. O'Mullane, *Nanoscale*, 2014, **6**, 4012–4026.

63 Z. Wang, H. Jin, T. Meng, K. Liao, W. Meng, J. Yang, D. He, Y. Xiong and S. Mu, *Adv. Funct. Mater.*, 2018, **28**, 1802596.

64 A. S. Aricò, P. Bruce, B. Scrosati, J.-M. Tarascon and W. V. Schalkwijk, *Materials for Sustainable Energy: a collection of peer-reviewed research and review articles from Nature Publishing Group*, 2011, pp. 148–159.

65 L. Zhang, K. Doyle-Davis and X. Sun, *Energy Environ. Sci.*, 2019, **12**, 492–517.

66 M. Escudero-Escribano, P. Malacrida, M. H. Hansen, U. G. Vej-Hansen, A. Velázquez-Palenzuela, V. Tripkovic, J. Schiøtz, J. Rossmeisl, I. E. L. Stephens and I. Chorkendorff, *Science*, 2016, **352**, 73–76.

67 F. Calle-Vallejo, J. Tymoczko, V. Colic, Q. H. Vu, M. D. Pohl, K. Morgenstern, D. Loffreda, P. Sautet, W. Schuhmann and A. S. Bandarenka, *Science*, 2015, **350**, 185–189.

68 R. Chattot, O. Le Bacq, V. Beermann, S. Kühl, J. Herranz, S. Henning, L. Kühn, T. Asset, L. Guétaz, G. Renou, J. Drnec, P. Bordet, A. Pasturel, A. Eychmüller, T. J. Schmidt, P. Strasser, L. Dubau and F. Maillard, *Nat. Mater.*, 2018, **17**, 827–833.

69 M. Li, Z. Zhao, T. Cheng, A. Fortunelli, C.-Y. Chen, R. Yu, Q. Zhang, L. Gu, B. V. Merinov, Z. Lin, E. Zhu, T. Yu, Q. Jia, J. Guo, L. Zhang, W. A. Goddard, Y. Huang and X. Duan, *Science*, 2016, **354**, 1414–1419.

70 C. Chen, Y. Kang, Z. Huo, Z. Zhu, W. Huang, H. L. Xin, J. D. Snyder, D. Li, J. A. Herron, M. Mavrikakis, M. Chi, K. L. More, Y. Li, N. M. Markovic, G. A. Somorjai, P. Yang and V. R. Stamenkovic, *Science*, 2014, **343**, 1339–1343.

71 N. Cheng, M. N. Banis, J. Liu, A. Riese, X. Li, R. Li, S. Ye, S. Knights and X. Sun, *Adv. Mater.*, 2015, **27**, 277–281.

72 B. Y. Xia, H. B. Wu, N. Li, Y. Yan, X. W. Lou and X. Wang, *Angew. Chem., Int. Ed.*, 2015, **54**, 3797–3801.

73 X. Zhou, J. Qiao, L. Yang and J. Zhang, *Adv. Energy Mater.*, 2014, **4**, 1301523.

74 L. Liu and A. Corma, *Chem. Rev.*, 2018, **118**, 4981–5079.

75 B. Y. Xia, Y. Yan, N. Li, H. B. Wu, X. W. Lou and X. Wang, *Nat. Energy*, 2016, **1**, 15006.

76 Z. Chen, D. Higgins, A. Yu, L. Zhang and J. Zhang, *Energy Environ. Sci.*, 2011, **4**, 3167–3192.

77 J. Masa, W. Xia, M. Muhler and W. Schuhmann, *Angew. Chem., Int. Ed.*, 2015, **54**, 10102–10120.

78 K. Artyushkova, I. Matanovic, B. Halevi and P. Atanassov, *J. Phys. Chem. C*, 2017, **121**, 2836–2843.

79 C. W. B. Bezerra, L. Zhang, K. Lee, H. Liu, A. L. B. Marques, E. P. Marques, H. Wang and J. Zhang, *Electrochim. Acta*, 2008, **53**, 4937–4951.

80 Y.-C. Wang, Y.-J. Lai, L. Song, Z.-Y. Zhou, J.-G. Liu, Q. Wang, X.-D. Yang, C. Chen, W. Shi, Y.-P. Zheng, M. Rauf and S.-G. Sun, *Angew. Chem.*, 2015, **127**, 10045–10048.

81 E. Proietti, F. Jaouen, M. Lefèvre, N. Larouche, J. Tian, J. Herranz and J.-P. Dodelet, *Nat. Commun.*, 2011, **2**, 416.

82 X. Wan, W. Chen, J. Yang, M. Liu, X. Liu and J. Shui, *ChemElectroChem*, 2019, **6**, 304.

83 J. Wang, Z. Huang, W. Liu, C. Chang, H. Tang, Z. Li, W. Chen, C. Jia, T. Yao, S. Wei, Y. Wu and Y. Li, *J. Am. Chem. Soc.*, 2017, **139**, 17281–17284.

84 J. K. Nørskov, F. Abild-Pedersen, F. Studt and T. Bligaard, *Proc. Natl. Acad. Sci. U. S. A.*, 2011, **108**, 937–943.

85 J. K. Nørskov, T. Bligaard, J. Rossmeisl and C. H. Christensen, *Nat. Chem.*, 2009, **1**, 37–46.

2918 | *Energy Environ. Sci.*, 2019, **12**, 2890–2923

This journal is © The Royal Society of Chemistry 2019

86 Z. W. Seh, J. Kibsgaard, C. F. Dickens, I. Chorkendorff, J. K. Nørskov and T. F. Jaramillo, *Science*, 2017, **355**, eaad4998.

87 J. A. Keith and T. Jacob, *Angew. Chem., Int. Ed.*, 2010, **49**, 9521–9525.

88 H. A. Hansen, J. Rossmeisl and J. K. Nørskov, *Phys. Chem. Chem. Phys.*, 2008, **10**, 3722–3730.

89 H.-Y. Su, Y. Gorlin, I. C. Man, F. Calle-Vallejo, J. K. Nørskov, T. F. Jaramillo and J. Rossmeisl, *Phys. Chem. Chem. Phys.*, 2012, **14**, 14010–14022.

90 F. Calle-Vallejo, J. I. Martínez and J. Rossmeisl, *Phys. Chem. Chem. Phys.*, 2011, **13**, 15639–15643.

91 D. Raciti, J. Kubal, C. Ma, M. Barclay, M. Gonzalez, M. Chi, J. Greeley, K. L. More and C. Wang, *Nano Energy*, 2016, **20**, 202–211.

92 J. H. Zagal and M. T. M. Koper, *Angew. Chem., Int. Ed.*, 2016, **55**, 14510–14521.

93 M. J. Kolb, J. Wermink, F. Calle-Vallejo, L. B. F. Juurlink and M. T. M. Koper, *Phys. Chem. Chem. Phys.*, 2016, **18**, 3416–3422.

94 F. Calle-Vallejo, M. D. Pohl, D. Reinisch, D. Loffreda, P. Sautet and A. S. Bandarenka, *Chem. Sci.*, 2017, **8**, 2283–2289.

95 A. A. Herzing, C. J. Kiely, A. F. Carley, P. Landon and G. J. Hutchings, *Science*, 2008, **321**, 1331–1335.

96 U. Heiz, A. Sanchez, S. Abbet and W.-D. Schneider, *J. Am. Chem. Soc.*, 1999, **121**, 3214–3217.

97 M. Turner, V. B. Golovko, O. P. Vaughan, P. Abdulkin, A. Berenguer-Murcia, M. S. Tikhov, B. F. Johnson and R. M. Lambert, *Nature*, 2008, **454**, 981.

98 H. Fei, J. Dong, M. J. Arellano-Jiménez, G. Ye, N. Dong Kim, E. L. G. Samuel, Z. Peng, Z. Zhu, F. Qin, J. Bao, M. J. Yacaman, P. M. Ajayan, D. Chen and J. M. Tour, *Nat. Commun.*, 2015, **6**, 8668.

99 P. Yin, T. Yao, Y. Wu, L. Zheng, Y. Lin, W. Liu, H. Ju, J. Zhu, X. Hong, Z. Deng, G. Zhou, S. Wei and Y. Li, *Angew. Chem., Int. Ed.*, 2016, **55**, 10800–10805.

100 J. Lin, A. Wang, B. Qiao, X. Liu, X. Yang, X. Wang, J. Liang, J. Li, J. Liu and T. Zhang, *J. Am. Chem. Soc.*, 2013, **135**, 15314–15317.

101 X.-F. Yang, A. Wang, B. Qiao, J. Li, J. Liu and T. Zhang, *Acc. Chem. Res.*, 2013, **46**, 1740–1748.

102 C. T. Campbell, S. C. Parker and D. E. Starr, *Science*, 2002, **298**, 811–814.

103 B. Qiao, A. Wang, X. Yang, L. F. Allard, Z. Jiang, Y. Cui, J. Liu, J. Li and T. Zhang, *Nat. Chem.*, 2011, **3**, 634–641.

104 J. Jones, H. Xiong, A. T. DeLaRiva, E. J. Peterson, H. Pham, S. R. Challa, G. Qi, S. Oh, M. H. Wiebenga, X. I. Pereira Hernández, Y. Wang and A. K. Datye, *Science*, 2016, **353**, 150–154.

105 P. Liu, Y. Zhao, R. Qin, S. Mo, G. Chen, L. Gu, D. M. Chevrier, P. Zhang, Q. Guo, D. Zang, B. Wu, G. Fu and N. Zheng, *Science*, 2016, **352**, 797–800.

106 M. Yang, L. F. Allard and M. Flytzani-Stephanopoulos, *J. Am. Chem. Soc.*, 2013, **135**, 3768–3771.

107 Z. Zhang, Y. Zhu, H. Asakura, B. Zhang, J. Zhang, M. Zhou, Y. Han, T. Tanaka, A. Wang, T. Zhang and N. Yan, *Nat. Commun.*, 2017, **8**, 16100.

108 S. F. J. Hackett, R. M. Brydson, M. H. Gass, I. Harvey, A. D. Newman, K. Wilson and A. F. Lee, *Angew. Chem., Int. Ed.*, 2007, **46**, 8593–8596.

109 H. Fei, J. Dong, Y. Feng, C. S. Allen, C. Wan, B. Volosskiy, M. Li, Z. Zhao, Y. Wang, H. Sun, P. An, W. Chen, Z. Guo, C. Lee, D. Chen, I. Shakir, M. Liu, T. Hu, Y. Li, A. I. Kirkland, X. Duan and Y. Huang, *Nat. Catal.*, 2018, **1**, 63–72.

110 Y. Chen, S. Ji, C. Chen, Q. Peng, D. Wang and Y. Li, *Joule*, 2018, **2**, 1242–1264.

111 C. H. Choi, M. Kim, H. C. Kwon, S. J. Cho, S. Yun, H.-T. Kim, K. J. J. Mayrhofer, H. Kim and M. Choi, *Nat. Commun.*, 2016, **7**, 10922.

112 H. Yan, Y. Lin, H. Wu, W. Zhang, Z. Sun, H. Cheng, W. Liu, C. Wang, J. Li, X. Huang, T. Yao, J. Yang, S. Wei and J. Lu, *Nat. Commun.*, 2017, **8**, 1070.

113 J. P. Collman, P. Denisevich, Y. Konai, M. Marrocco, C. Koval and F. C. Anson, *J. Am. Chem. Soc.*, 1980, **102**, 6027–6036.

114 E. Yeager, *J. Mol. Catal.*, 1986, **38**(1–2), 5–26.

115 N. R. Sahraie, U. I. Kramm, J. Steinberg, Y. Zhang, A. Thomas, T. Reier, J.-P. Paraknowitsch and P. Strasser, *Nat. Commun.*, 2015, **6**, 8618.

116 Z. Li, H. He, H. Cao, S. Sun, W. Diao, D. Gao, P. Lu, S. Zhang, Z. Guo, M. Li, R. Liu, D. Ren, C. Liu, Y. Zhang, Z. Yang, J. Jiang and G. Zhang, *Appl. Catal., B*, 2019, **240**, 112–121.

117 J. Wang, W. Liu, G. Luo, Z. Li, C. Zhao, H. Zhang, M. Zhu, Q. Xu, X. Wang, C. Zhao, Y. Qu, Z. Yang, T. Yao, Y. Li, Y. Lin, Y. Wu and Y. Li, *Energy Environ. Sci.*, 2018, **11**, 3375–3379.

118 Z. Lu, B. Wang, Y. Hu, W. Liu, Y. Zhao, R. Yang, Z. Li, J. Luo, B. Chi, Z. Jiang, M. Li, S. Mu, S. Liao, J. Zhang and X. Sun, *Angew. Chem., Int. Ed.*, 2019, **58**, 2622–2626.

119 Y. Zhao, D. Liu, B. Wang, H. Li, S. Huang, M. Liu, J. Wang, Q. Wang and J. Zhang, *Nano Energy*, 2019, **58**, 277–283.

120 J.-C. Liu, Y.-G. Wang and J. Li, *J. Am. Chem. Soc.*, 2017, **139**, 6190–6199.

121 T. He, S. Chen, B. Ni, Y. Gong, Z. Wu, L. Song, L. Gu, W. Hu and X. Wang, *Angew. Chem.*, 2018, **130**, 3551–3556.

122 N. Cheng, S. Stambula, D. Wang, M. N. Banis, J. Liu, A. Riese, B. Xiao, R. Li, T.-K. Sham, L.-M. Liu, G. A. Botton and X. Sun, *Nat. Commun.*, 2016, **7**, 13638.

123 L. Wang, L. Li, W. Zhang, X. Zhao, J. Qiu, A. Li, X. Zheng, Z. Hu, R. Si and J. Zeng, *Angew. Chem., Int. Ed.*, 2017, **56**, 4712–4718.

124 C. Li, *Chin. J. Catal.*, 2016, **37**, 1443–1445.

125 B. Wang, X. Wang, J. Zou, Y. Yan, S. Xie, G. Hu, Y. Li and A. Dong, *Nano Lett.*, 2017, **17**, 2003–2009.

126 J. Wang, Z. Li, Y. Wu and Y. Li, *Adv. Mater.*, 2018, **30**, 1801649.

127 S. Liang, C. Hao and Y. Shi, *ChemCatChem*, 2015, **7**, 2559–2567.

128 A. Uzun, V. Ortalan, Y. Hao, N. D. Browning and B. C. Gates, *ACS Nano*, 2009, **3**, 3691–3695.

129 A. J. Mackus, M. A. Verheijen, N. M. Leick, A. A. Bol and W. M. Kessels, *Chem. Mater.*, 2013, **25**, 1905–1911.

This journal is © The Royal Society of Chemistry 2019

Energy Environ. Sci., 2019, **12**, 2890–2923 | 2919

130 T. E. James, S. L. Hemmingson and C. T. Campbell, *ACS Catal.*, 2015, **5**, 5673–5678.

131 J. Liu, *ACS Catal.*, 2017, **7**, 34–59.

132 W.-J. Jiang, L. Gu, L. Li, Y. Zhang, X. Zhang, L.-J. Zhang, J.-Q. Wang, J.-S. Hu, Z. Wei and L.-J. Wan, *J. Am. Chem. Soc.*, 2016, **138**, 3570–3578.

133 A. Wang, J. Li and T. Zhang, *Nat. Rev. Chem.*, 2018, **2**, 65–81.

134 A. Zitolo, N. Ranjbar-Sahraie, T. Mineva, J. Li, Q. Jia, S. Stamatin, G. F. Harrington, S. M. Lyth, P. Krtil, S. Mukerjee, E. Fonda and F. Jaouen, *Nat. Commun.*, 2017, **8**, 957.

135 Z. Li, D. Wang, Y. Wu and Y. Li, *Natl. Sci. Rev.*, 2018, **5**, 673–689.

136 Y. Wu, D. Wang and Y. Li, *Sci. China Mater.*, 2016, **59**, 938–996.

137 B. Bayatsarmadi, Y. Zheng, A. Vasileff and S.-Z. Qiao, *Small*, 2017, **13**, 1700191.

138 J. Deng, H. Li, J. Xiao, Y. Tu, D. Deng, H. Yang, H. Tian, J. Li, P. Ren and X. Bao, *Energy Environ. Sci.*, 2015, **8**, 1594–1601.

139 D. Zhang, W. Chen, Z. Li, Y. Chen, L. Zheng, Y. Gong, Q. Li, R. Shen, Y. Han, W.-C. Cheong, L. Gu and Y. Li, *Chem. Commun.*, 2018, **54**, 4274–4277.

140 S. Yang, J. Kim, Y. J. Tak, A. Soon and H. Lee, *Angew. Chem., Int. Ed.*, 2016, **55**, 2058–2062.

141 S. Yang, Y. J. Tak, J. Kim, A. Soon and H. Lee, *ACS Catal.*, 2017, **7**, 1301–1307.

142 X. Wang, W. Wang, M. Qiao, G. Wu, W. Chen, T. Yuan, Q. Xu, M. Chen, Y. Zhang, X. Wang, J. Wang, J. Ge, X. Hong, Y. Li, Y. Wu and Y. Li, *Sci. Bull.*, 2018, **63**, 1246–1253.

143 L. Zhang, T. Liu, N. Chen, Y. Jia, R. Cai, W. Theis, X. Yang, Y. Xia, D. Yang and X. Yao, *J. Mater. Chem. A*, 2018, **6**, 18417–18425.

144 X. Zeng, J. Shui, X. Liu, Q. Liu, Y. Li, J. Shang, L. Zheng and R. Yu, *Adv. Energy Mater.*, 2018, **8**, 1701345.

145 X. Li, W. Bi, L. Zhang, S. Tao, W. Chu, Q. Zhang, Y. Luo, C. Wu and Y. Xie, *Adv. Mater.*, 2016, **28**, 2427–2431.

146 J. Li, S. Chen, N. Yang, M. Deng, S. Ibraheem, J. Deng, J. Li, L. Li and Z. Wei, *Angew. Chem., Int. Ed.*, 2019, **58**, 7035–7039.

147 Z. Zhang, Y. Chen, L. Zhou, C. Chen, Z. Han, B. Zhang, Q. Wu, L. Yang, L. Du, Y. Bu, P. Wang, X. Wang, H. Yang and Z. Hu, *Nat. Commun.*, 2019, **10**, 1657.

148 Q. Li, W. Chen, H. Xiao, Y. Gong, Z. Li, L. Zheng, X. Zheng, W. Yan, W.-C. Cheong, R. Shen, N. Fu, L. Gu, Z. Zhuang, C. Chen, D. Wang, Q. Peng, J. Li and Y. Li, *Adv. Mater.*, 2018, **30**, 1800588.

149 Y. Chen, S. Ji, Y. Wang, J. Dong, W. Chen, Z. Li, R. Shen, L. Zheng, Z. Zhuang, D. Wang and Y. Li, *Angew. Chem., Int. Ed.*, 2017, **56**, 6937–6941.

150 W. Zang, A. Sumboja, Y. Ma, H. Zhang, Y. Wu, S. Wu, H. Wu, Z. Liu, C. Guan, J. Wang and S. J. Pennycook, *ACS Catal.*, 2018, **8**, 8961–8969.

151 C. Zhao, X. Dai, T. Yao, W. Chen, X. Wang, J. Wang, J. Yang, S. Wei, Y. Wu and Y. Li, *J. Am. Chem. Soc.*, 2017, **139**, 8078–8081.

152 X. Cui, J. Xiao, Y. Wu, P. Du, R. Si, H. Yang, H. Tian, J. Li, W.-H. Zhang, D. Deng and X. Bao, *Angew. Chem.*, 2016, **128**, 6820–6824.

153 X. Zhang, Z. Wu, X. Zhang, L. Li, Y. Li, H. Xu, X. Li, X. Yu, Z. Zhang, Y. Liang and H. Wang, *Nat. Commun.*, 2017, **8**, 14675.

154 Y. Shi, C. Zhao, H. Wei, J. Guo, S. Liang, A. Wang, T. Zhang, J. Liu and T. Ma, *Adv. Mater.*, 2014, **26**, 8147–8153.

155 X. Wang, W. Chen, L. Zhang, T. Yao, W. Liu, Y. Lin, H. Ju, J. Dong, L. Zheng and W. Yan, *J. Am. Chem. Soc.*, 2017, **139**, 9419–9422.

156 L. Jiao, G. Wan, R. Zhang, H. Zhou, S.-H. Yu and H.-L. Jiang, *Angew. Chem., Int. Ed.*, 2018, **57**, 8525–8529.

157 R. Jiang, L. Li, T. Sheng, G. Hu, Y. Chen and L. Wang, *J. Am. Chem. Soc.*, 2018, **140**, 11594–11598.

158 H. Yan, H. Cheng, H. Yi, Y. Lin, T. Yao, C. Wang, J. Li, S. Wei and J. Lu, *J. Am. Chem. Soc.*, 2015, **137**, 10484–10487.

159 X. Han, X. Ling, Y. Wang, T. Ma, C. Zhong, W. Hu and Y. Deng, *Angew. Chem.*, 2019, **131**, 5413–5418.

160 X. X. Wang, D. A. Cullen, Y.-T. Pan, S. Hwang, M. Wang, Z. Feng, J. Wang, M. H. Engelhard, H. Zhang, Y. He, Y. Shao, D. Su, K. L. More, J. S. Spendelow and G. Wu, *Adv. Mater.*, 2018, **30**, 1706758.

161 H. T. Chung, D. A. Cullen, D. Higgins, B. T. Sneed, E. F. Holby, K. L. More and P. Zelenay, *Science*, 2017, **357**, 479–484.

162 M. Zhang, Y.-G. Wang, W. Chen, J. Dong, L. Zheng, J. Luo, J. Wan, S. Tian, W.-C. Cheong, D. Wang and Y. Li, *J. Am. Chem. Soc.*, 2017, **139**, 10976–10979.

163 G. Wan, P. Yu, H. Chen, J. Wen, C.-J. Sun, H. Zhou, N. Zhang, Q. Li, W. Zhao, B. Xie, T. Li and J. Shi, *Small*, 2018, **14**, 1704319.

164 S. Dilpazir, H. He, Z. Li, M. Wang, P. Lu, R. Liu, Z. Xie, D. Gao and G. Zhang, *ACS Appl. Energy Mater.*, 2018, **1**, 3283–3291.

165 P. Song, M. Luo, X. Liu, W. Xing, W. Xu, Z. Jiang and L. Gu, *Adv. Funct. Mater.*, 2017, **27**, 1700802.

166 J.-D. Yi, R. Xu, Q. Wu, T. Zhang, K.-T. Zang, J. Luo, Y.-L. Liang, Y.-B. Huang and R. Cao, *ACS Energy Lett.*, 2018, **3**, 883–889.

167 C. Wang, H. Zhang, J. Wang, Z. Zhao, J. Wang, Y. Zhang, M. Cheng, H. Zhao and J. Wang, *Chem. Mater.*, 2017, **29**, 9915–9922.

168 Z. Zhang, X. Gao, M. Dou, J. Ji and F. Wang, *Small*, 2017, **13**, 1604290.

169 A. Han, W. Chen, S. Zhang, M. Zhang, Y. Han, J. Zhang, S. Ji, L. Zheng, Y. Wang, L. Gu, C. Chen, Q. Peng, D. Wang and Y. Li, *Adv. Mater.*, 2018, **30**, 1706508.

170 C. Tang, B. Wang, H.-F. Wang and Q. Zhang, *Adv. Mater.*, 2017, **29**, 1703185.

171 H.-J. Qiu, Y. Ito, W. Cong, Y. Tan, P. Liu, A. Hirata, T. Fujita, Z. Tang and M. Chen, *Angew. Chem., Int. Ed.*, 2015, **54**, 14031–14035.

172 H. Shen, E. Gracia-Espino, J. Ma, H. Tang, X. Mamat, T. Wagberg, G. Hu and S. Guo, *Nano Energy*, 2017, **35**, 9–16.

173 N. Jia, Q. Xu, F. Zhao, H.-X. Gao, J. Song, P. Chen, Z. An, X. Chen and Y. Chen, *ACS Appl. Energy Mater.*, 2018, **1**, 4982–4990.

2920 | *Energy Environ. Sci.*, 2019, **12**, 2890–2923

This journal is © The Royal Society of Chemistry 2019

174 C. Zhu, S. Fu, J. Song, Q. Shi, D. Su, M. H. Engelhard, X. Li, D. Xiao, D. Li, L. Estevez, D. Du and Y. Lin, *Small*, 2017, **13**, 1603407.

175 L. Yang, D. Cheng, H. Xu, X. Zeng, X. Wan, J. Shui, Z. Xiang and D. Cao, *Proc. Natl. Acad. Sci. U. S. A.*, 2018, **115**, 6626–6631.

176 L. Yang, L. Shi, D. Wang, Y. Lv and D. Cao, *Nano Energy*, 2018, **50**, 691–698.

177 X. Zhang, J. Guo, P. Guan, C. Liu, H. Huang, F. Xue, X. Dong, S. J. Pennycook and M. F. Chisholm, *Nat. Commun.*, 2013, **4**, 1924.

178 M. Piernavieja-Hermida, Z. Lu, A. White, K.-B. Low, T. Wu, J. W. Elam, Z. Wu and Y. Lei, *Nanoscale*, 2016, **8**, 15348–15356.

179 S. Sun, G. Zhang, N. Gauquelin, N. Chen, J. Zhou, S. Yang, W. Chen, X. Meng, D. Geng, M. N. Banis, R. Li, S. Ye, S. Knights, G. A. Botton, T.-K. Sham and X. Sun, *Sci. Rep.*, 2013, **3**, 1775.

180 Y. Qu, Z. Li, W. Chen, Y. Lin, T. Yuan, Z. Yang, C. Zhao, J. Wang, C. Zhao, X. Wang, F. Zhou, Z. Zhuang, Y. Wu and Y. Li, *Nat. Catal.*, 2018, **1**, 781–786.

181 S. Wei, A. Li, J.-C. Liu, Z. Li, W. Chen, Y. Gong, Q. Zhang, W.-C. Cheong, Y. Wang, L. Zheng, H. Xiao, C. Chen, D. Wang, Q. Peng, L. Gu, X. Han, J. Li and Y. Li, *Nat. Nanotechnol.*, 2018, **13**, 856–861.

182 J. Yang, Z. Qiu, C. Zhao, W. Wei, W. Chen, Z. Li, Y. Qu, J. Dong, J. Luo, Z. Li and Y. Wu, *Angew. Chem., Int. Ed.*, 2018, **57**, 14095–14100.

183 Y. Qu, B. Chen, Z. Li, X. Duan, L. Wang, Y. Lin, T. Yuan, F. Zhou, Y. Hu, Z. Yang, C. Zhao, J. Wang, C. Zhao, Y. Hu, G. Wu, Q. Zhang, Q. Xu, B. Liu, P. Gao, R. You, W. Huang, L. Zheng, L. Gu, Y. Wu and Y. Li, *J. Am. Chem. Soc.*, 2019, **141**, 4505–4509.

184 X. Guo, G. Fang, G. Li, H. Ma, H. Fan, L. Yu, C. Ma, X. Wu, D. Deng, M. Wei, D. Tan, R. Si, S. Zhang, J. Li, L. Sun, Z. Tang, X. Pan and X. Bao, *Science*, 2014, **344**, 616–619.

185 D. Deng, X. Chen, L. Yu, X. Wu, Q. Liu, Y. Liu, H. Yang, H. Tian, Y. Hu, P. Du, R. Si, J. Wang, X. Cui, H. Li, J. Xiao, T. Xu, J. Deng, F. Yang, P. N. Duchesne, P. Zhang, J. Zhou, L. Sun, J. Li, X. Pan and X. Bao, *Sci. Adv.*, 2015, **1**, e1500462.

186 M. Moses-DeBusk, M. Yoon, L. F. Allard, D. R. Mullins, Z. Wu, X. Yang, G. Veith, G. M. Stocks and C. K. Narula, *J. Am. Chem. Soc.*, 2013, **135**, 12634–12645.

187 R. Jin, C. Zeng, M. Zhou and Y. Chen, *Chem. Rev.*, 2016, **116**, 10346–10413.

188 H. Wei, X. Liu, A. Wang, L. Zhang, B. Qiao, X. Yang, Y. Huang, S. Miao, J. Liu and T. Zhang, *Nat. Commun.*, 2014, **5**, 5634.

189 J. Kim, H.-E. Kim and H. Lee, *ChemSusChem*, 2018, **11**, 104–113.

190 Y. Zhu, X. Chen, J. Liu, J. Zhang, D. Xu, W. Peng, Y. Li, G. Zhang, F. Zhang and X. Fan, *ChemSusChem*, 2018, **11**, 2402–2409.

191 K. Kamiya, R. Kamai, K. Hashimoto and S. Nakanishi, *Nat. Commun.*, 2014, **5**, 5040.

192 L. Zhang, X. Wang, R. Wang and M. Hong, *Chem. Mater.*, 2015, **27**, 7610–7618.

193 W. Chaikittisilp, K. Ariga and Y. Yamauchi, *J. Mater. Chem. A*, 2013, **1**, 14–19.

194 Y. Li and H. Dai, *Chem. Soc. Rev.*, 2014, **43**, 5257–5275.

195 P. Tan, B. Chen, H. Xu, H. Zhang, W. Cai, M. Ni, M. Liu and Z. Shao, *Energy Environ. Sci.*, 2017, **10**, 2056–2080.

196 B. Liu, H. Shioyama, T. Akita and Q. Xu, *J. Am. Chem. Soc.*, 2008, **130**, 5390–5391.

197 P. Zhang, F. Sun, Z. Xiang, Z. Shen, J. Yun and D. Cao, *Energy Environ. Sci.*, 2014, **7**, 442–450.

198 M. O'Keeffe and O. M. Yaghi, *Chem. Rev.*, 2011, **112**, 675–702.

199 Z. Liang, C. Qu, D. Xia, R. Zou and Q. Xu, *Angew. Chem., Int. Ed.*, 2018, **57**, 9604–9633.

200 Y. Zheng and S.-Z. Qiao, *Natl. Sci. Rev.*, 2018, **5**, 626–627.

201 X. Fang, Q. Shang, Y. Wang, L. Jiao, T. Yao, Y. Li, Q. Zhang, Y. Luo and H.-L. Jiang, *Adv. Mater.*, 2018, **30**, 1705112.

202 H. Zhang, S. Hwang, M. Wang, Z. Feng, S. Karakalos, L. Luo, Z. Qiao, X. Xie, C. Wang, D. Su, Y. Shao and G. Wu, *J. Am. Chem. Soc.*, 2017, **139**, 14143–14149.

203 W. Chen, J. Pei, C.-T. He, J. Wan, H. Ren, Y. Zhu, Y. Wang, J. Dong, S. Tian, W.-C. Cheong, S. Lu, L. Zheng, X. Zheng, W. Yan, Z. Zhuang, C. Chen, Q. Peng, D. Wang and Y. Li, *Angew. Chem.*, 2017, **129**, 16302–16306.

204 S. Ma, G. A. Goenaga, A. V. Call and D.-J. Liu, *Chem. – Eur. J.*, 2011, **17**, 2063–2067.

205 C. Zhu, H. Li, S. Fu, D. Du and Y. Lin, *Chem. Soc. Rev.*, 2016, **45**, 517–531.

206 J. Tang, J. Liu, C. Li, Y. Li, M. O. Tade, S. Dai and Y. Yamauchi, *Angew. Chem., Int. Ed.*, 2015, **54**, 588–593.

207 W. Liu, L. Zhang, W. Yan, X. Liu, X. Yang, S. Miao, W. Wang, A. Wang and T. Zhang, *Chem. Sci.*, 2016, **7**, 5758–5764.

208 X. Sun, A. I. Olivos-Suarez, D. Osadchii, M. J. V. Romero, F. Kapteijn and J. Gascon, *J. Catal.*, 2018, **357**, 20–28.

209 Y. Han, Y.-G. Wang, W. Chen, R. Xu, L. Zheng, J. Zhang, J. Luo, R.-A. Shen, Y. Zhu, W.-C. Cheong, C. Chen, Q. Peng, D. Wang and Y. Li, *J. Am. Chem. Soc.*, 2017, **139**, 17269–17272.

210 W. Liu, L. Zhang, X. Liu, X. Liu, X. Yang, S. Miao, W. Wang, A. Wang and T. Zhang, *J. Am. Chem. Soc.*, 2017, **139**, 10790–10798.

211 H. Yang, S. J. Bradley, A. Chan, G. I. N. Waterhouse, T. Nann, P. E. Kruger and S. G. Telfer, *J. Am. Chem. Soc.*, 2016, **138**, 11872–11881.

212 Y. Chen, P. Xu, M. Wu, Q. Meng, H. Chen, Z. Shu, J. Wang, L. Zhang, Y. Li and J. Shi, *Adv. Mater.*, 2014, **26**, 4294–4301.

213 C. Detavernier, J. Dendooven, S. Pulinthanathu Sree, K. F. Ludwig and J. A. Martens, *Chem. Soc. Rev.*, 2011, **40**, 5242–5253.

214 N. Cheng, Y. Shao, J. Liu and X. Sun, *Nano Energy*, 2016, **29**, 220–242.

215 H. Zhang, G. Liu, L. Shi and J. Ye, *Adv. Energy Mater.*, 2018, **8**, 1701343.

216 H. Wei, K. Huang, D. Wang, R. Zhang, B. Ge, J. Ma, B. Wen, S. Zhang, Q. Li, M. Lei, C. Zhang, J. Irawan, L.-M. Liu and H. Wu, *Nat. Commun.*, 2017, **8**, 1490.

217 P. Zhang, L. Wang, S. Yang, J. A. Schott, X. Liu, S. M. Mahurin, C. Huang, Y. Zhang, P. F. Fulvio, M. F. Chisholm and S. Dai, *Nat. Commun.*, 2017, **8**, 15020.

218 U. Heiz, A. Sanchez, S. Abbet and W. D. Schneider, *J. Am. Chem. Soc.*, 1999, **121**, 3214–3217.

This journal is © The Royal Society of Chemistry 2019

Energy Environ. Sci., 2019, **12**, 2890–2923 | 2921

219 S. Abbet, A. Sanchez, U. Heiz, W. D. Schneider, A. M. Ferrari, G. Pacchioni and N. Rösch, *J. Am. Chem. Soc.*, 2000, **122**, 3453–3457.

220 W. E. Kaden, T. Wu, W. A. Kunkel and S. L. Anderson, *Science*, 2009, **326**, 826–829.

221 Y. Lei, F. Mehmood, S. Lee, J. Greeley, B. Lee, S. Seifert, R. E. Winans, J. W. Elam, R. J. Meyer, P. C. Redfern, D. Teschner, R. Schlögl, M. J. Pellin, L. A. Curtiss and S. Vajda, *Science*, 2010, **328**, 224–228.

222 S. Vajda and M. G. White, *ACS Catal.*, 2015, **5**, 7152–7176.

223 M. Zhou, J. E. Dick and A. J. Bard, *J. Am. Chem. Soc.*, 2017, **139**, 17677–17682.

224 H. Fei, J. Dong, C. Wan, Z. Zhao, X. Xu, Z. Lin, Y. Wang, H. Liu, K. Zang, J. Luo, S. Zhao, W. Hu, W. Yan, I. Shakir, Y. Huang and X. Duan, *Adv. Mater.*, 2018, **30**, 1802146.

225 D. C. Young, *Computational chemistry: a practical guide for applying techniques to real world problems[M]*, John Wiley & Sons, 2004.

226 G. Gao, Y. Jiao, E. R. Waclawik and A. Du, *J. Am. Chem. Soc.*, 2016, **138**, 6292–6297.

227 Y. Zhao, M. Zhu and L. Kang, *Catal. Lett.*, 2018, **148**, 2992–3002.

228 I. MacLaren and Q. M. Ramasse, *Int. Mater. Rev.*, 2014, **59**, 115–131.

229 J. Liu, *Chin. J. Catal.*, 2017, **38**, 1460–1472.

230 S. Wang, A. Y. Borisevich, S. N. Rashkeev, M. V. Glazoff, K. Sohlberg, S. J. Pennycook and S. T. Pantelides, *Nat. Mater.*, 2004, **3**, 143.

231 G. S. Parkinson, *Chin. J. Catal.*, 2017, **38**, 1454–1459.

232 H. Zhang, X. Li and Z. Jiang, *Curr. Opin. Electrochem.*, 2019, **14**, 7–15.

233 X. Liu and T.-C. Weng, *MRS Bull.*, 2016, **41**, 466–472.

234 I. Ogino, *Chin. J. Catal.*, 2017, **38**, 1481–1488.

235 J. Liu, M. Jiao, L. Lu, H. M. Barkholtz, Y. Li, Y. Wang, L. Jiang, Z. Wu, D.-J. Liu, L. Zhuang, C. Ma, J. Zeng, B. Zhang, D. Su, P. Song, W. Xing, W. Xu, Y. Wang, Z. Jiang and G. Sun, *Nat. Commun.*, 2017, **8**, 15938.

236 H. Funke, A. C. Scheinost and M. Chukalina, *Phys. Rev. B: Condens. Matter Mater. Phys.*, 2005, **71**, 094110.

237 Z. Xia, H. Zhang, K. Shen, Y. Qu and Z. Jiang, *Phys. B*, 2018, **542**, 12–19.

238 H. Zhang, J. Wei, J. Dong, G. Liu, L. Shi, P. An, G. Zhao, J. Kong, X. Wang, X. Meng, J. Zhang and J. Ye, *Angew. Chem.*, 2016, **128**, 14522–14526.

239 C. Asokan, L. DeRita and P. Christopher, *Chin. J. Catal.*, 2017, **38**, 1473–1480.

240 J. T. Yates Jr., S. D. Worley, T. M. Duncan and R. W. Vaughan, *J. Chem. Phys.*, 1979, **70**, 1225–1230.

241 V. L. Zholobenko, G.-D. Lei, B. T. Carvill, B. A. Lerner and W. M. H. Sachtler, *J. Chem. Soc., Faraday Trans.*, 1994, **90**, 233–238.

242 W. Zhang, S. Xu, X. Han and X. Bao, *Chem. Soc. Rev.*, 2012, **41**, 192–210.

243 A. Zitolo, V. Goellner, V. Armel, M.-T. Sougrati, T. Mineva, L. Stievano, E. Fonda and F. Jaouen, *Nat. Mater.*, 2015, **14**, 937.

244 H. Shen, E. Gracia-Espino, J. Ma, K. Zang, J. Luo, L. Wang, S. Gao, X. Mamat, G. Hu and T. Wagberg, *Angew. Chem., Int. Ed.*, 2017, **56**, 13800–13804.

245 M. Ferrandon, A. J. Kropf, D. J. Myers, K. Artyushkova, U. Kramm, P. Bogdanoff, G. Wu, C. M. Johnston and P. Zelenay, *J. Phys. Chem. C*, 2012, **116**, 16001–16013.

246 U. I. Kramm, I. Herrmann-Geppert, J. Behrends, K. Lips, S. Fiechter and P. Bogdanoff, *J. Am. Chem. Soc.*, 2016, **138**, 635–640.

247 Y. Deng, B. Chi, X. Tian, Z. Cui, E. Liu, Q. Jia, W. Fan, G. Wang, D. Dang, M. Li, K. Zang, J. Luo, Y. Hu, S. Liao, X. Sun and S. Mukerjee, *J. Mater. Chem. A*, 2019, **7**, 5020–5030.

248 M. Xiao, J. Zhu, L. Ma, Z. Jin, J. Ge, X. Deng, Y. Hou, Q. He, J. Li, Q. Jia, S. Mukerjee, R. Yang, Z. Jiang, D. Su, C. Liu and W. Xing, *ACS Catal.*, 2018, **8**, 2824–2832.

249 D. Zhao, J.-L. Shui, L. R. Grabstanowicz, C. Chen, S. M. Commet, T. Xu, J. Lu and D.-J. Liu, *Adv. Mater.*, 2014, **26**, 1093–1097.

250 S. Gong, C. Wang, P. Jiang, L. Hu, H. Lei and Q. Chen, *J. Mater. Chem. A*, 2018, **6**, 13254–13262.

251 Y. Mun, S. Lee, K. Kim, S. Kim, S. Lee, J. W. Han and J. Lee, *J. Am. Chem. Soc.*, 2019, **141**, 6254–6262.

252 L. Ma, S. Chen, Z. Pei, Y. Huang, G. Liang, F. Mo, Q. Yang, J. Su, Y. Gao, J. A. Zapien and C. Zhi, *ACS Nano*, 2018, **12**, 1949–1958.

253 Y. Deng, B. Chi, J. Li, G. Wang, L. Zheng, X. Shi, Z. Cui, L. Du, S. Liao, K. Zang, J. Luo, Y. Hu and X. Sun, *Adv. Energy Mater.*, 2019, **9**, 1802856.

254 L. Zhang, J. M. T. A. Fischer, Y. Jia, X. Yan, W. Xu, X. Wang, J. Chen, D. Yang, H. Liu, L. Zhuang, M. Hankel, D. J. Searles, K. Huang, S. Feng, C. L. Brown and X. Yao, *J. Am. Chem. Soc.*, 2018, **140**, 10757–10763.

255 S. H. Ahn, X. Yu and A. Manthiram, *Adv. Mater.*, 2017, **29**, 1606534.

256 Z. Wei, in *Electrocatalysis*, ed. S. Sun and S. Chen, Chemical Industry Press, 2013, ch. 4, pp. 113–195.

257 Y. Peng, B. Lu and S. Chen, *Adv. Mater.*, 2018, 1801995.

258 F. He, K. Li, C. Yin, Y. Wang, H. Tang and Z. Wu, *Carbon*, 2017, **114**, 619–627.

259 S. M. Kozlov, G. Kovács, R. Ferrando and K. M. Neyman, *Chem. Sci.*, 2015, **6**, 3868–3880.

260 A. Krasheninnikov, P. Lehtinen, A. S. Foster, P. Pyykkö and R. M. Nieminen, *Phys. Rev. Lett.*, 2009, **102**, 126807.

261 B. Lu, T. J. Smart, D. Qin, J. E. Lu, N. Wang, L. Chen, Y. Peng, Y. Ping and S. Chen, *Chem. Mater.*, 2017, **29**, 5617–5628.

262 C. K. Poh, S. H. Lim, J. Lin and Y. P. Feng, *J. Phys. Chem. C*, 2014, **118**, 13525–13538.

263 E. F. Holby, G. Wu, P. Zelenay and C. D. Taylor, *J. Phys. Chem. C*, 2014, **118**, 14388–14393.

264 V. Tripkovic, *Phys. Chem. Chem. Phys.*, 2017, **19**, 29381–29388.

265 Z.-D. He, S. Hanselman, Y.-X. Chen, M. T. M. Koper and F. Calle-Vallejo, *J. Phys. Chem. Lett.*, 2017, **8**, 2243–2246.

266 F. Calle-Vallejo, J. I. Martínez, J. M. García-Lastra, E. Abad and M. T. M. Koper, *Surf. Sci.*, 2013, **607**, 47–53.

2922 | *Energy Environ. Sci.*, 2019, **12**, 2890–2923

This journal is © The Royal Society of Chemistry 2019

267 S. Kattel, P. Atanassov and B. Kiefer, *Phys. Chem. Chem. Phys.*, 2014, **16**, 13800–13806.

268 Z. Duan and G. Wang, *Phys. Chem. Chem. Phys.*, 2011, **13**, 20178–20187.

269 J. K. Nørskov, J. Rossmeisl, A. Logadottir, L. Lindqvist, J. R. Kitchin, T. Bligaard and H. Jónsson, *J. Phys. Chem. B*, 2004, **108**, 17886–17892.

270 J. A. Gauthier, S. Ringe, C. F. Dickens, A. J. Garza, A. T. Bell, M. Head-Gordon, J. K. Nørskov and K. Chan, *ACS Catal.*, 2019, **9**, 920–931.

271 J. X. Wang, F. A. Uribe, T. E. Springer, J. Zhang and R. R. Adzic, *Faraday Discuss.*, 2009, **140**, 347–362.

272 V. Tripkovic and T. Vegge, *J. Phys. Chem. C*, 2017, **121**, 26785–26793.

273 E. F. Holby and C. D. Taylor, *Sci. Rep.*, 2015, **5**, 9286.

274 J. L. Kneebone, S. L. Daifuku, J. A. Kehl, G. Wu, H. T. Chung, M. Y. Hu, E. E. Alp, K. L. More, P. Zelenay, E. F. Holby and M. L. Neidig, *J. Phys. Chem. C*, 2017, **121**, 16283–16290.

275 T. Kondo, S. Casolo, T. Suzuki, T. Shikano, M. Sakurai, Y. Harada, M. Saito, M. Oshima, M. I. Trioni, G. F. Tantardini and J. Nakamura, *Phys. Rev. B: Condens. Matter Mater. Phys.*, 2012, **86**, 035436.

276 S. Guo and S. Sun, *J. Am. Chem. Soc.*, 2012, **134**, 2492–2495.

277 J. Liu, B. R. Bunes, L. Zang and C. Wang, *Environ. Chem. Lett.*, 2018, **16**, 477–505.

278 Y. Chen, Z. Huang, Z. Ma, J. Chen and X. Tang, *Catal. Sci. Technol.*, 2017, **7**, 4250–4258.

279 J.-C. Liu, Y. Tang, Y.-G. Wang, T. Zhang and J. Li, *Natl. Sci. Rev.*, 2018, **5**, 638–641.

280 C. T. Campbell, *Nat. Chem.*, 2012, **4**, 597.

281 P. Liu and N. Zheng, *Natl. Sci. Rev.*, 2018, **5**, 636–638.

282 N. Govindarajan, J. M. García-Lastra, E. J. Meijer and F. Calle-Vallejo, *Curr. Opin. Electrochem.*, 2018, **8**, 110–117.

283 M. T. de Groot and M. T. M. Koper, *Phys. Chem. Chem. Phys.*, 2008, **10**, 1023–1031.

284 M. Busch, *Curr. Opin. Electrochem.*, 2018, **9**, 278–284.

This journal is © The Royal Society of Chemistry 2019

Energy Environ. Sci., 2019, **12**, 2890–2923 | **2923**